MODEL-PLANT MISMATCH DIAGNOSIS USING PLANT MODEL RATIOS FOR A GRINDING MILL CIRCUIT UNDER MODEL PREDICTIVE CONTROL

by

Heinz Karl Mittermaier

Submitted in partial fulfilment of the requirements for the degree

Master of Engineering (Electronic Engineering)

in the

Department of Electrical, Electronic and Computer Engineering

Faculty of Engineering, Built Environment and Information Technology

UNIVERSITY OF PRETORIA

November 2023

SUMMARY

MODEL-PLANT MISMATCH DIAGNOSIS USING PLANT MODEL RATIOS FOR A
GRINDING MILL CIRCUIT UNDER MODEL PREDICTIVE CONTROL

by

Heinz Karl Mittermaier

Supervisor:	Prof. J. D. Le Roux
Co-supervisor:	Prof. I. K. Craig
Department:	Electrical, Electronic and Computer Engineering
University:	University of Pretoria
Degree:	Master of Engineering (Electronic Engineering)
Keywords:	Controller performance monitoring, grinding mill circuit, model predictive control, model-plant mismatch, process performance monitoring.

In the context of a mineral processing plant, the process of separating valuable materials from ore encompasses several sequential stages. The first stage of the process includes the crushing and grinding of the ore via crushers and grinding mills, collectively referred to as the comminution stage. This stage lays the critical foundation for the downstream stages to follow. The comminution stage focuses on stable throughput and reducing the ore to a specific product particle size distribution as fed to the subsequent separation stage. For semi-autogenous grinding mill circuits this is achieved by feeding the ore into the grinding mill along with water and steel balls. The rotation of the mill then causes the steel balls to fall from the sides of the mill and crush the ore. The crushed ore will be fed into a sump and then pumped into a classifier. The classifier separates the in-specification material from the out-of-specification material. The particles that are in-specification will be fed into the separation stage while the particles that are too large will be fed back into the mill.

To optimize throughput, power utilization, ensure process safety, and maintain stable operational conditions, mineral processing plants have increasingly embraced the implementation of control systems. Some control strategies include the employment of advanced process control techniques like

model predictive controllers and real-time optimization layers, deployed in conjunction with cascaded control systems and multiple-layer control systems as well as regulatory control and supervisory control strategies to ensure optimal operation of plants in the mineral process industry. For advanced process control, and more specifically model predictive control, to work as intended, an accurate model of the plant is required. For most industrial processes, a linear model is fitted to a specific operating point for the plant, in particular first order plus time delay model, and therefore this will be the focus of the study. Unfortunately, most real-world plants are by nature non-linear and therefore, a change in operating condition will constitute a model-plant mismatch being introduced to the model-based controller. This mismatch will lead to a degradation of controller performance causing suboptimal control of the plant.

To identify and diagnose the model-plant mismatch, and therefore ensure optimal model predictive control, the plant model ratio is investigated. By using a ratio of the plant transfer function to the model transfer function, the method is able to identify each parameter, within a first order plus time delay representation of the process, that contains a model-plant mismatch as well as diagnose the relative size and the direction of the mismatch for each parameter namely gain, time constant, and delay. Furthermore, using a plant model ratio estimation technique, multiple-input multiple-output systems can be decoupled, forming a plant model ratio matrix, and therefore the model-plant mismatch will be isolated to specific entries in the plant model ratio matrix. Thereafter, the parameters containing model-plant mismatch will be identified and diagnosed.

The plant model ratio is then applied to a grinding mill circuit under model predictive control. Sub-optimal identification, isolation, and diagnosis of the model-plant mismatch within a grinding mill circuit is obtained. This allows for the investigation of the limitations of the plant model ratio. The first limitation is that if the process gains are not within the same order of magnitude, the cross-spectral density will be overpowered, rendering the plant model ratio less effective. Nonetheless, this limitation can be mitigated by correctly scaling the model of the process. The second limitation is that if the process dynamics are not within the same range, a dynamic imbalance will be present within the process, also resulting in suboptimal results using the plant model ratio.

ACKNOWLEDGEMENTS

I would like to thank my supervisors, Prof. Derik le Roux and Prof. Ian Craig, for guiding me through the research that was conducted. I am grateful for their guidance and the invaluable insights they provided, which deepened my understanding of research.

I would like to thank Mintek for their financial support over the past two years. They have allowed me to pursue work that I am passionate about along with the prospects of continuing the work in the years to come. I also extend my thanks to, Dr. Lodewicus Coetzee, for imparting insightful views on my research.

I would like to thank the IFAC Foundation for allowing me to attend the 22nd World Congress of the International Federation of Automatic Control (IFAC2023) in Yokohama, Japan. This was a surreal experience that I will remember for the rest of my life. Thank you to my co-authors on the presented paper, Prof. Derik le Roux, Dr. Laurentz Olivier, and Prof. Ian Craig, for contributing to the success of the research.

I would like to thank my family. To my parents, Markus and Rové Mittermaier, thank you for the support you have shown towards my education. I will always cherish your sacrifices that have paved the way for me to achieve all my goals. I would also like to express my gratitude to my grandfather for his contributions to the expansion of my education.

I would like to thank my wife, Janie Mittermaier. Without you, I would not be able to stand where I stand today. Your continued love, support, understanding and encouragement are what helped me to succeed, not only in my studies but in life.

Finally, I am thankful to God for granting me the ability and opportunity to achieve this significant milestone.

LIST OF ABBREVIATIONS

APC	advanced process control
AWGN	additive white Gaussian noise
CPM	controller performance monitoring
CSD	cross-spectral density
CV	controlled variable
FOPTD	first order plus time delay
IMC	internal model control
LTI	linear time-invariant
MIMO	multiple-input multiple-output
MPC	model predictive control
MV	manipulated variable
PCSD	partial cross-spectral density
PMR	plant model ratio
SISO	single-input single-output

TABLE OF CONTENTS

LIST OF FIGURES

LIST OF TABLES

CHAPTER 1   INTRODUCTION

1.1   PROBLEM STATEMENT

1.1.1   Context of the Problem

Process control is a crucial discipline that involves the monitoring and manipulation of processes to ensure consistency, efficiency and quality. The application of process control, and more specifically advanced process control (APC), strategies to industrial plants can lead to:

1. **Improved efficiency**: The optimization of both controlled variables (CVs) and manipulated variables (MVs), can translate into cost savings and enhanced resource utilization, by improving productivity, minimizing energy consumption and reducing waste materials.

2. **Enhanced quality**: APC methods can minimize output variations which results in higher quality products while reducing defective products.

3. **Increased profitability**: By increasing the process throughput, while minimizing process waste, APC methods can increase industrial profitability.

Therefore, the addition of APC technologies to an industrial setting can aid in the success and sustainability of systems across a multitude of sectors. One of the most prominent APC methodologies is that of the model predictive controller (MPC) (Darby and Nikolaou, 2012) which aims to control a system, in an optimal manner, while conforming to both predefined MV and CV constraints.

This short description of MPC can be expanded as done by Camacho and Bordons (1999) where MPC is defined as an optimal control technique in which the calculated control actions minimize a cost function for a constrained dynamical system over a finite, receding, horizon. Therefore, at each time step the MPC controller receives the current plant states. If the states are not measurable, they can be estimated using a state estimator, for example, a Kalman-filter. Using these states as an initial condition, the controller will use the **internal model of the plant** to simulate the plant outputs (CVs)

over the prediction horizon. The simulation is done by applying a set of control moves (MVs), over the length of the control horizon, to the **internal model of the plant**. These control moves are then adjusted using a constrained optimization problem to solve a cost function that drives the CVs to the desired setpoint while minimizing the rate of change of the MVs. The first MV as determined by the optimization problem is applied to the plant and the algorithm is repeated. The optimization problem can be visualized as in Figure 1.1 (Camacho and Bordons, 1999; Wang, 2009).
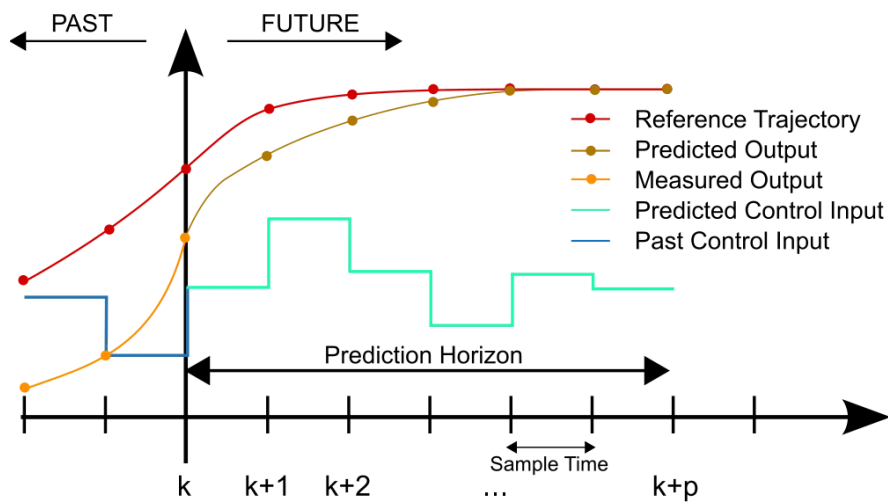
Figure 1.1. A visual representation of a model predictive controller.

From this description of MPC, it is evident that an accurate initial state as well as an accurate model of the plant is required at each time step. While the theory of state estimation has been thoroughly explored (Azhin et al., 2022; Holten et al., 1988; Han et al., 2021; Varas et al., 2019), one of the predominant factors of process control is that a change in process dynamics is unavoidable. These changes in dynamics can cause performance deterioration of model-based controllers over time and significantly reduce the performance benefit of MPC (Mayne, 2014; Qin and Badgwell, 2003; Schwenzer et al., 2021).

1.1.2   Process Input/Output Relationship

Most MPC controllers in the process industries use a linear model of the process as the internal model of the plant, and therefore the input/output relationship of the linear process can be defined using a transfer function (Seborg et al., 2016). These transfer functions can be represented as either first-order or higher-order functions with or without time delays including or excluding time-varying elements, while non-linear systems can be approximated using transfer functions. Therefore, depending on the

process being described by the transfer function, different complexities can be introduced to increase or decrease the accuracy of the process representation.

Even though most processes in the industry tend to be higher order and non-linear, a widely used representation of process-based plants are those of a first-order plus time delay (FOPTD) transfer function, as these representations tend to encapsulate enough information to accurately perform process control, and even APC, over a narrow range of operating conditions. The FOPTD transfer function contains a gain term (K), a time constant term (τ) and a delay term (D), as seen in (1.1). The FOPTD transfer function typography is extensively used to represent grinding mill circuits as seen in Craig and MacLeod (1995), Niu et al. (2017), Olivier and Craig (2011), and Xu et al. (2018).

$$G(s) = \frac{Ke^{-Ds}}{\tau s + 1} \tag{1.1}$$

1.1.3 Non-Linear Nature of Grinding Mills

As discussed by Coetzee et al. (2010), Le Roux et al. (2013), and Le Roux et al. (2020) a closed-loop grinding mill circuit is inherently non-linear, primarily as a result of the parabolic nature of the mill power draw in relation to the mill filling. In addition to this relationship, disturbances can also introduce non-linearity into a grinding mill. These disturbances include:

- Material properties,
- Mill erosion,
- Size reduction mechanisms, and
- Particle size distribution.

However, a linear time-invariant (LTI) representation of the grinding mill, as used in Craig and MacLeod (1995), provides a sufficiently accurate representation of the plant for control in a narrow range of operating conditions. Nonetheless, over time the operating conditions of the mill will change, caused by either setpoint changes implemented by the plant operator or a disturbance as previously mentioned, and therefore the narrow range of operating conditions, for which the LTI model was developed, will be violated. This violation will cause an inaccurate representation of the plant over time, leading to the performance of a linear MPC controller deteriorating when applied to the grinding mill.

1.1.4 Research Gap

Seeing that the need for an accurate model of the controlled plant is required for MPC to function as intended, a lot of research on the topic of model-plant mismatch (MPM) detection, identification and

diagnosis, under the umbrella of controller performance monitoring (CPM), has been done. Nonetheless, a robust method of MPM diagnosis is still to be developed within the process control industry. A degraded plant model, in model-based control, is one of the primary reasons why decoupled classical proportional-integral-derivative controllers are often favoured above APC methods for multiple-input, multiple-output (MIMO) plants, especially for grinding mill circuits (Hodouin, 2011; Olivier and Craig, 2017; Wei and Craig, 2009).

In light of the non-linear nature of grinding mills, the fidelity of the linear model used by MPC to control the grinding mill circuit will inevitably degrade, and in return, the MPC performance will diminish. Therefore, it is crucial to be able to detect and diagnose MPM in an online fashion for grinding mills under MPC. Therefore, CPM is the focus of this research.

The plant model ratio (PMR), is a proposed method of detecting MPM in systems that are represented using FOPTD transfer functions. The method holds potential as it is capable of:

- Isolating the MPM to a specific entry in a MIMO transfer function matrix,
- Identify the parameter(s) in the FOPTD transfer function (i.e., the gain, time constant, delay terms) that contains the MPM, and
- Diagnose the direction and the relative size of the MPM for each identified parameter.

For this reason, the PMR is chosen as the method with the most potential from the methods discussed in the literature review. Thus, the PMR method is evaluated on benchmark problems in the area of CPM as well as investigated for the use of MPM diagnosis for grinding mill circuits.

1.2 RESEARCH OBJECTIVE AND QUESTIONS

1.2.1 Research Objective

The proposed research is focused on the development of a robust MPM diagnosis procedure within the scope of mineral processing and more specifically grinding mill circuits. The aim is to determine the degree and direction of MPM from routine operational data in an online fashion. The method should be non-intrusive, and the plant should be able to function as intended while the diagnosis is performed.

1.2.2 Research Questions

- For a SISO plant under MPC, can the MPM be identified per FOPTD parameter, and can each mismatch direction be diagnosed from routine operational data?

- For a MIMO plant under MPC, can the MPM be isolated to each entry in the MIMO transfer function matrix, can the MPM be identified per FOPTD parameter, and can each mismatch direction be diagnosed from routine operational data?
- Can the MIMO case of the MPM methodology be applied to a grinding mill circuit under MPC?

1.3 RESEARCH GOALS

From the research questions, the following research goals were formulated:

- Assess and investigate the use of PMR to detect MPM for SISO systems under linear MPC control.
- Assess and investigate the use of PMR to detect MPM for MIMO systems under linear MPC control.
- Assess the feasibility of using the PMR to detect MPM in grinding mill circuits under linear MPC control.

1.4 APPROACH

To attain the research goals the following approach is followed:

- Research and present recent trends and developments in the field of MPM detection and diagnoses for plants controlled by model-based controllers.
- Develop and expand the frequency-based analysis of the PMR for SISO systems, including the required methodology of estimating the PMR from routine operational data.
- Incorporate an optimal delay estimation technique into the PMR to mitigate the need for high-frequency excitation within the system.
- Expand the PMR to MIMO systems by means of decorrelation of transfer functions from routine operating data realizing an $n \times n$ PMR matrix that can accommodate the application of the SISO PMR to each entry.
- Assess the SISO PMR methodology on a pressure control system, by testing the following mismatches:
  - Exclusively diagnose the MPM in the gain term of the transfer function.
  - Exclusively diagnose the MPM in the time constant term of the transfer function.
  - Exclusively diagnose the MPM in the delay term of the transfer function.
  - Diagnose the MPM in a combination of FOPTD terms.
- Assess the MIMO PMR methodology on a distillation column by testing a combination of mismatches in multiple transfer functions.

- Apply the MIMO PMR to a grinding mill circuit, replicating a real-world scenario as closely as possible and assess the feasibility of the PMR.

1.5   RESEARCH CONTRIBUTION

The main contribution of the research stems from the application of the PMR to a grinding mill circuit. The work successfully assesses the PMR as applied to SISO and MIMO systems and further tests the viability of using the PMR to diagnose MPM for grinding mill circuits, with a FOPTD representation, under MPC.

1.6   RESEARCH OUTPUTS

The following publications resulted from this study. An initial simulation study on the PMR applied to a grinding mill circuit, was published in:

- Mittermaier, H.K., le Roux, J.D., Olivier, L.E. and Craig, I.K., 2023. Model-plant mismatch detection for a plant under Model Predictive Control: A grinding mill circuit case study. IFAC-PapersOnLine, 56(2), pp.11778-11783.

1.7   OVERVIEW OF STUDY

In Chapter 2 a literature review is conducted on recent innovations of MPM methodologies within the process control industry. This is followed by the full development of the PMR and improved PMR methods for both SISO and MIMO cases in Chapter 3. Chapter 4 contains the evaluation of both SISO and MIMO PMR methodologies on a number of scenarios to ensure that the MPM diagnosis procedure developed in Chapter 3 is reliable. A non-linear model of a grinding mill circuit is derived in Chapter 5, followed by a system identification (SID) of the grinding mill to obtain a set of FOPTD transfer functions for the mill about a specific operating point. This linear representation of the model is used to test the PMR as applied to the grinding mill circuit. Concluding remarks can be found in Chapter 6.

CHAPTER 2   LITERATURE STUDY

2.1   CHAPTER OVERVIEW

The literature review that follows is focused on CPM within the bounds of process control and with an emphasis on model-based control. The controller performance methods are divided into indirect methods of CPM and direct methods of CPM. Each subset of monitoring approaches is explored within this chapter, followed by a brief overview of CPM within the minerals processing industry.

2.2   CONTROLLER PERFORMANCE MONITORING

One of the predominant factors of process control is that a change in process dynamics, due to non-linear processes, is unavoidable. These changes in dynamics can cause performance deterioration of model-based controllers over time and significantly reduce the performance benefit of MPC controllers (Mayne, 2014; Qin and Badgwell, 2003; Schwenzer et al., 2021). This is one of the reasons why decoupled classical proportional-integral-derivative controllers are often favoured above advanced process control (APC) methods for multiple-input multiple-output (MIMO) plants, especially when applied to grinding mill circuits (Hodouin, 2011; Olivier and Craig, 2017; Wei and Craig, 2009).

CPM in the form of model-plant mismatch (MPM) detection, isolation and diagnosis have been identified and developed to the point where MPM can be identified in an online fashion, with minimal process disruption (Wu and Du, 2022). Each method of CPM for model-based controllers can be classified into either indirect or direct methods as described below.

2.2.1   Indirect Methods of Controller Performance Monitoring

The principal categories for the indirect methods are statistical-based techniques and sensitivity function-based methods.

2.2.1.1 Statistical-Based Techniques

Partial correlation analysis

Badwe et al. (2009) proposed a partial correlation analysis on which most of the statistical-based methodologies are based. The proposed methodology first calculates the disturbance-free components of the MV. These disturbance-free MV components are then decorrelated to all other MVs ($\hat{\varepsilon}_{u_i}$) to allow a single transfer function containing the MPM to be identified within a MIMO transfer function matrix. The same steps are used to decorrelate the model residuals to all the MVs ($\hat{\varepsilon}_{e_j}$). A non-zero cross-correlation between $\hat{\varepsilon}_{u_i}$ and $\hat{\varepsilon}_{e_j}$ indicates an MPM within the $u_i - y_j$ input-output channel, where u_i is the i-th input and y_j is the j-th output of the system. The larger the correlation coefficient the more significant the MPM will be.

For the specific proposed methodology to work, a data set with sufficient setpoint excitation is required since the method investigated uses the estimation of loop sensitivities between the setpoints and the MVs. The setpoint excitation will ensure estimation accuracy to evaluate the information matrix as described by Ljung (1999).

Correlation analysis

In contrast to the required setpoint excitation of the partial correlation analysis of Badwe et al. (2009), the correlation analysis method described by Li et al. (2020) requires a data set with zero setpoint changes. The methodology uses a correlation analysis method between the inputs and the disturbances along with a model quality index to formulate a custom model assessment index applicable to an MPC algorithm using a univariate predictive control structure. The MPM location within the MIMO transfer function matrix can then be identified by means of decorrelation (Sun et al., 2013; Webber and Gupta, 2008). Therefore, all disturbances will have to be measurable for the results to be dependable.

Plant model ratio

In addition to partial correlation, other statistical-based techniques include the PMR as developed by Selvanathan and Tangirala (2010a) and is defined as the ratio of the plant transfer function to the model transfer function ($G/\hat{G}$). This definition of MPM allows for the diagnosis of gain, time constant and delay mismatches within a SISO system, with the caveat that high-frequency broadband excitation is required within the system. To mitigate the requirement for high-frequency excitation, an improved PMR method as described by Yerramilli and Tangirala (2018) was developed where an optimal delay estimation technique is used to allow for delay mismatch diagnosis without high-frequency excitation.

Selvanathan and Tangirala (2010a) discussed how to estimate the PMR from routine operational data while Yerramilli and Tangirala (2016) expanded the PMR estimation to MIMO systems by introducing a decoupling estimation of the PMR for multivariate systems.

Variance ratio-based model evaluation index

The variance ratio-based model evaluation index, much like the partial correlation analysis (Badwe et al., 2009) and the PMR (Selvanathan and Tangirala, 2010a), is based on the IMC structure. This method of MPM detection uses the adaptive Lasso approach to determine the order and estimate the parameters of a linear regression model (Zou, 2006). The following steps can be followed to obtain the variance ratio-based model evaluation index:

Step 1 : Collect routine closed-loop data including the setpoints ($r(t)$), CV ($y(t)$), MV ($u(t)$) and calculate the output error ($e(t) = y(t) - r(t)$).

Step 2 : Construct the required data matrices as described by Ling et al. (2017) and Ljung (1999).

Step 3 : If the order of the disturbance is 0 or 1, calculate the estimated disturbance model using the adaptive Lasso equation. If the disturbance order is greater than 1, estimate the discrete process time delay as discussed in Wang et al. (2015) and then calculate the estimated disturbance model using the adaptive Lasso equation.

Step 4 : Using the closed-loop input/output data, calculate the model quality variable.

Step 5 : Calculate the model evaluation index using the model quality variable and the error estimation (from step 1). Since a model evaluation index of 1 represents a perfect model of the plant, the further the model evaluation index is from 1 the more MPM can be expected (Ling et al., 2017).

Autocovariance-based process parameter value identification

The methodology proposed by Xu et al. (2020) stems from an autocovariance approach to identify the minimization of discrepancies between dynamic matrix control parameters and the sampled matrix parameters of MIMO systems under MPC (Chen et al., 2013; Wang et al., 2017; Xu et al., 2020).

2.2.1.2 Sensitivity Function-Based Techniques

A dual validation algorithm

The dual validation algorithm for CPM is based on the dual-model divergence method that was developed by Basseville and Benveniste (1983), and includes a sequential segmentation of non-stationary digital signals through the detection of changes in an autoregressive model with an unknown

model switching time. Therefore, using the Box-Jenkins structure (Ljung, 1999) an estimation for the time-variant plant and disturbance models can be obtained. Then, using the statistical methods of Basseville and Nikiforov (1993) applied to these estimations, the variance between the plant and disturbances models could be calculated. The dual-model divergence method applied to the calculated variance indicates the amount of MPM (Jiang et al., 2009).

Markov parameter estimation

As described by Al-Muthairi and Bingulac (1995) and Phan et al. (1991) the Markov parameters can be extracted from routine operational data. A statistical-based evaluation of the Markov parameters yields the MPM methodology as described by the following steps:

Step 1 : Select the Markov Parameter vector order, the window size, the step length, the number of windows, and the number of variables.

Step 2 : Collect the operation data where sufficient setpoint excitation is present.

Step 3 : Construct Hankel matrices and estimate the Markov parameter matrix from operational data. Then extract the Markov Parameter vectors related to different moving windows.

Step 4 : Calculate the corresponding mean values and standard derivations.

Step 5 : Check the overlap between the two bands and decide whether a mismatch is present. (Yin et al., 2014).

Improved PMR with minimal excitation

The improved PMR (Kaw et al., 2014), follows the same structure for PMR as discussed in Section 2.2.1.1 (and in Chapter 3) but further develops auxiliary characteristics to improve upon the PMR. These characteristics include:

- **Setpoint shaping -** From a sensitivity analysis of the PMR, it is found that the same results can be obtained from a dual-frequency sinusoidal dithering signal as with a broadband excitation as recommended by Selvanathan and Tangirala (2010a). Ideally, these setpoint signals will have frequencies of $\omega_1 = 0$ (a step change) and $\omega_2 = \infty$. Seeing that, in reality, most feedback control systems are low pass filters and noise starts to play a role at higher frequency, a recommended formula to obtain ω_2 is given.

- **PMR estimation, including distributional properties -** Taking into consideration the sinusoidal setpoint proposed by Selvanathan and Tangirala (2010a), a statistical approach to the PMR equation is used seeing that the stochastic part of the plant output will form a Gaussian

distribution. Therefore, the central limit theorem can be used to adjust the PMR in order to improve the method.

2.2.2 Direct Methods of Controller Performance Monitoring

Indemnification algorithm set

The single predominant direct method of MPM detection is the proposed algorithms by Tsai et al. (2015). The first algorithm is based on using small sinusoidal test signals to estimate the process frequency responses and is used to identify if MPM is present. If MPM is present, the second algorithm is used to pinpoint the transfer function(s) in the transfer function matrix that contains the MPM. The second algorithm uses a frequency domain representation of the relative sensitivity function to construct an indemnification matrix used to isolate the MPM within the transfer function matrix.

Error detection of multivariate systems

The specific method of detecting MPM in multivariable systems under MPC proposed by Ji et al. (2012) lends itself to the implementation of non-disturbing sinusoidal dither signals as testing signals. These testing signals can then be used to estimate the process frequency response at multiple frequency points. From the frequency response points, an error index matrix can be constructed and used to access the model error captured in the MPC controller (Gao et al., 2016; Ji et al., 2012).

2.3 CPM FOR THE MINERAL PROCESSING INDUSTRY

For the same reasons mentioned in Section 2.2, various CPM methods used within the minerals processing industry have received substantial attention in the literature and can be classified into classical CPM techniques or data-driven CPM techniques.

2.3.1 Classical CPM used in the Mineral Processing Industry

A computational fluid dynamics model of a hydrocyclone could be used to cross-reference the system performance between the simulated (or expected) results and the real-world results as proposed by Schwarz et al. (2019). Cut size, pressure drop, and water split are combined with a trivial error calculation to quantify the performance of the hydrocyclone.

Topographic and symptomatic search techniques are presented by Venkatasubramanian et al. (2003). Topographic searches perform malfunction analysis using a template of normal operation, whereas symptomatic searches look for symptoms to direct the search to the fault location. Both search methodologies can be applied to the minerals processing industry as discussed by Taguchi (2014) and Venkatasubramanian et al. (2003).

Within the minerals processing industry, oscillations can propagate through multiple units of the plant, causing CVs to deviate from their respective setpoints leading to a degradation of controller performance. Lindner et al. (2018) proposed the use of transfer entropy and a non-linearity index to detect this degradation since the transfer entropy applies a causality analysis to the measured variables allowing the propagation path of the oscillations to be traced. The non-linearity index can then be applied to this propagation path based on the assumption that the oscillations will be greatest when closest to the origin of the oscillations.

2.3.2 Data-Driven CPM for the Mineral Processing Industry

Wakefield et al. (2018) proposed a statistical-based process monitoring approach using feature extraction by means of principal component analysis. The method is then expanded to a fault detection and diagnosis strategy using the Granger causality as a data-based CPM topology.

Based on the complexity and variability of processes, model-based fault diagnosis tends to be too time-consuming (or computationally expensive) to implement within the minerals processing industry while data-based methods tend to be less computationally expensive but exclude knowledge from model-based fault diagnosis. Therefore, Groenewald and Aldrich (2015) proposed a hybrid approach between causality maps and data-based fault diagnosis methods in the form of extreme learning machine algorithms.

2.4 CHAPTER SUMMARY

Within this chapter, different approaches to detecting MPM in the process industry were briefly explored. Each method described consists of unique advantages and disadvantages that could play a fatal role in the success or downfall of the method when applied to a grinding mill circuit. After consideration of each method's characteristics, the PMR with the optimal delay estimation will be used as the basis of this research. The PMR methodology will be developed (Chapter 3), evaluated on general processes (Chapter 4) and tested on a grinding mill circuit (Chapter 5).

CHAPTER 3 PLANT MODEL RATIO

3.1 CHAPTER OVERVIEW

The following chapter will focus on the development of the PMR methodology. In Section 3.2 the PMR is developed for SISO systems. This includes the theoretical derivation of each parameter mismatch based on the FOPTD transfer function as seen in (1.1). After the PMR diagnosis procedure has been described for each permutation of mismatch the full PMR diagnosis procedure, for all parameters, is presented in Table 3.3. In Section 3.2.3 the estimation of the SISO PMR from routine operational data is described, followed by the development of the improved PMR in Section 3.3. The improved PMR uses an optimal delay estimation technique to alleviate the PMR methodology from requiring high-frequency setpoint excitation. The PMR methodology is expanded to MIMO cases in Section 3.4 were the PMR estimation is done to realize a decoupled PMR matrix of SISO PMR entries. Finally, a few statements on the limitations and considerations of the PMR are made in Section 3.5.

3.2 PLANT MODEL RATIO FOR SISO SYSTEMS

By means of a model-plant comparison, within the internal model control (IMC) structure seen in Figure 3.1, controller performance can be improved by investigating the difference between the plant (G) and an online version of the plant model ($\hat{G}$). This comparison denotes the traditional form of MPM and can be represented as $\Delta G = G - \hat{G}$. Since ΔG is seldom zero due to modelling uncertainties
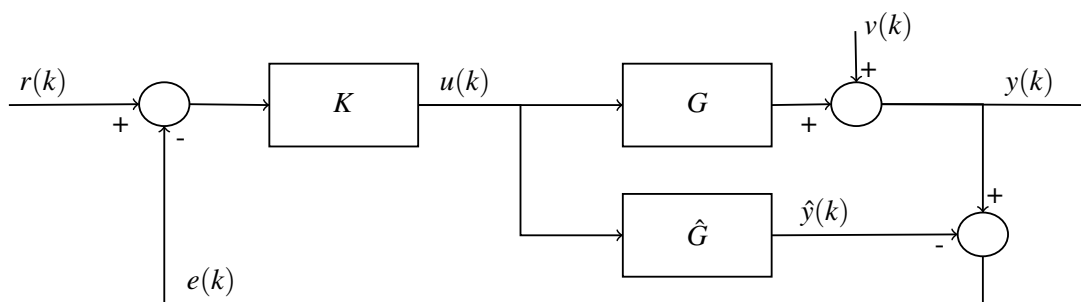
Figure 3.1. Closed-loop IMC structure.

and the lack of accurate process knowledge, the PMR was developed to mitigate the shortcomings of the traditional MPM (ΔG) and provide a method to collect improved information on MPM present in a specific process. Thus, from Figure 3.1, the PMR is defined as the ratio of the frequency response function of the plant ($G(e^{j\omega})$) to the frequency response function of the model ($\hat{G}(e^{j\omega})$):

$$G_{PMR}(e^{j\omega}) = \frac{G(e^{j\omega})}{\hat{G}(e^{j\omega})}. \tag{3.1}$$

This definition of the PMR is derived from a ratio between $\hat{G}$ and G and is applicable to all FOPTD transfer functions of the form seen in (1.1). In the absence of noise the PMR can also be interpreted as the transfer function between the model output $y(k)$ and the plant output $\hat{y}(k)$ as seen in Figure 3.2.

3.2.1 MPM Methodology Improvement

By using the polar representation of (3.1), the principal advantage of using PMR for MPM (as opposed to ΔG) can be seen:

$$\begin{aligned} G_{PMR}(e^{j\omega}) &= \frac{|\underline{G}(e^{j\omega})|e^{j\angle \underline{G}(e^{j\omega})}e^{-jD\omega}}{|\hat{\underline{G}}(e^{j\omega})|e^{j\angle \hat{\underline{G}}(e^{j\omega})}e^{-j\hat{D}\omega}} \\ &= M(\omega)e^{j\Delta P(\omega)}, \end{aligned} \tag{3.2}$$

where $\underline{G}$ and $\hat{\underline{G}}$ represent the delay-free parts of the plant and the model transfer functions, respectively. From (3.2), the fundamental MPM diagnosis can be derived, as seen later in this chapter, and the PMR allows for the individual MPM diagnosis of each parameter within the FOPTD transfer function. The magnitude mismatch information is contained in $M(\omega) = \frac{|\underline{G}(e^{j\omega})|}{|\hat{\underline{G}}(e^{j\omega})|}$ while the phase mismatch information is contained in $\Delta P(\omega) = \frac{e^{j\angle \underline{G}(e^{j\omega})}e^{-jD\omega}}{e^{j\angle \hat{\underline{G}}(e^{j\omega})}e^{-j\hat{D}\omega}}$. This allows the time constant mismatch to be decoupled from the delay mismatch. The improvement of the PMR over the traditional MPM representation can be verified by investigating the polar representation of the traditional MPM (ΔG):

$$\begin{aligned} \Delta G(e^{j\omega}) &= |\underline{G}(e^{j\omega})|e^{j\angle \underline{G}(e^{j\omega})}e^{-jD\omega} - |\hat{\underline{G}}(e^{j\omega})|e^{j\angle \hat{\underline{G}}(e^{j\omega})}e^{-j\hat{D}\omega} \\ &= A(\omega)e^{jB(\omega)}. \end{aligned} \tag{3.3}$$

Seeing that B in (3.3) contain elements of both the mismatched time constants as well as the mismatched delays, the improvements of the PMR on MPM detection and the ability to decouple the parametric mismatches from one another, compared to the PMR, is reaffirmed.
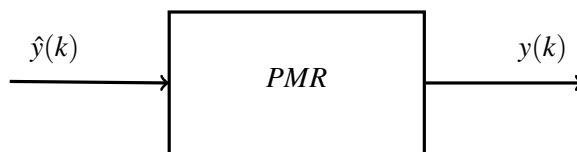
Figure 3.2. PMR interpreted as a transfer function.

3.2.2 The PMR Methodology

The following subsections will describe how mismatches in gain, time constant, delay, and the combination of the three can be identified using the PMR. The notation that will be used is:

- K - plant gain,
- $\hat{K}$ - nominal gain,
- τ - plant time constant,
- $\hat{\tau}$ - nominal time constant,
- D - plant time delay,
- $\hat{D}$ - nominal time delay, and

where the nominal parameter represents the parameter captured in the model of the system while the plant parameter is assumed to be the actual parameter of the system. A graphical representation of the mismatch diagnosis, which will be developed in the remainder of Section 3.2.2, can be seen in Table 3.1 and Table 3.2 followed by a summary of the MPM analysis in Table 3.3.

3.2.2.1 Gain Mismatch

A performance deterioration caused purely by a gain mismatch can be defined as:

- $K \neq \hat{K}$,
- $\tau = \hat{\tau}$, and
- $D = \hat{D}$.

Therefore, (3.1) will simplify to:

$$
\begin{aligned}
G_{PMR}(e^{j\omega}) &= \frac{|G(e^{j\omega})|e^{j\angle \underline{G}(e^{j\omega})}e^{-jD\omega}}{|\hat{G}(e^{j\omega})|e^{j\angle \underline{\hat{G}}(e^{j\omega})}e^{-j\hat{D}\omega}} \\
&= \frac{K}{\hat{K}}.
\end{aligned}
\tag{3.4}
$$

From (3.4), the MPM diagnosis can be formulated as:

$$
M(\omega) \neq 1 \quad \forall \omega
$$
$$
\Delta P(\omega) = 0 \quad \forall \omega.
\tag{3.5}
$$

The direction of the mismatch can also be determined as:

$$
M(\omega) > 1 \text{ if } K > \hat{K}
$$
$$
M(\omega) < 1 \text{ if } K < \hat{K}.
\tag{3.6}
$$

Thus, to determine if the mismatch between the plant and the model is purely due to a gain mismatch, the zero-frequency component (or DC term) of the magnitude spectrum of the PMR should not be one

while the phase of the PMR is zero over all frequencies. The direction of the mismatch is also directly correlated to the direction by which the zero-frequency component of the magnitude spectrum of the PMR deviates from one.

3.2.2.2   Time Constant Mismatch

A performance deterioration caused purely by a time constant mismatch can be defined as:

- $K = \hat{K}$,
- $\tau \neq \hat{\tau}$, and
- $D = \hat{D}$.

Therefore, (3.1) will simplify to:

$$
\begin{aligned}
G_{PMR}(e^{j\omega}) &= \frac{|G(e^{j\omega})|e^{j\angle \underline{G}(e^{j\omega})}e^{-jD\omega}}{|\hat{G}(e^{j\omega})|e^{j\angle \hat{\underline{G}}(e^{j\omega})}e^{-j\hat{D}\omega}} \\
&= \frac{(1-a)(1-e^{-j\omega}\hat{a})}{(1-\hat{a})(1-e^{-j\omega}a)} \\
&= M(\omega)e^{j\Delta P(\omega)},
\end{aligned}
\tag{3.7}
$$

where $a = e^{j\angle \underline{G}(e^{j\omega})}$ and $\hat{a} = e^{j\angle \hat{\underline{G}}(e^{j\omega})}$ as defined in (3.2) and therefore representing the time constant of the respective transfer functions:

$$
M(\omega) = \frac{(1-a)}{(1-\hat{a})}\sqrt{\frac{1-2\hat{a}\cos(\omega)+\hat{a}^2}{1-2a\cos(\omega)+a^2}},
\tag{3.8}
$$

while the phase spectrum will be:

$$
\Delta P(\omega) = \tan^{-1}\left(\frac{\hat{a}\sin(\omega)}{1-\hat{a}\cos(\omega)}\right) - \tan^{-1}\left(\frac{a\sin(\omega)}{1-a\cos(\omega)}\right).
\tag{3.9}
$$

From (3.8) and (3.9), the MPM will have the following effect on the PMR:

$$
\begin{aligned}
&M(\omega)|_{\omega=0} = 1 \\
&M(\omega)|_{\omega=0} \neq M(\omega)|_{\omega\neq0} \\
&\Delta P(\omega)|_{\omega=0,\pi} = 0 \\
&\Delta P(\omega)|_{\omega=0,\pi} \neq \Delta P(\omega)|_{\omega\neq0,\pi}.
\end{aligned}
\tag{3.10}
$$

Therefore, the time constant mismatch can be identified from either the magnitude spectrum or phase spectrum of the PMR. The diagnosis using the magnitude spectrum will be favoured in this representation of the PMR. Once the mismatch has been identified as a time constant mismatch, the

following criteria can be used to diagnose the direction of the mismatch:

$$M(\omega)|_{\omega=\pi} < 1 \text{ if } \tau > \hat{\tau}$$

$$M(\omega)|_{\omega=\pi} > 1 \text{ if } \tau < \hat{\tau}.$$

(3.11)

The magnitude spectrum in (3.11) can be evaluated at π seeing that the zero-frequency component of the magnitude spectrum will be 1 (since there us no gain mismatch present).

3.2.2.3　Delay Mismatch

A performance deterioration caused purely by a delay mismatch can be defined as:

- $K = \hat{K}$,
- $\tau = \hat{\tau}$, and
- $D \neq \hat{D}$.

Therefore, (3.1) will simplify to:

$$G_{PMR}(e^{j\omega}) = \frac{|G(e^{j\omega})|e^{j\angle \underline{G}(e^{j\omega})}e^{-jD\omega}}{|\hat{G}(e^{j\omega})|e^{j\angle \underline{\hat{G}}(e^{j\omega})}e^{-j\hat{D}\omega}}$$

$$= e^{-(D-\hat{D})j\omega},$$

(3.12)

and the delay mismatch can be diagnosed as:

$$M(\omega) = 1 \quad \forall \omega$$

$$\Delta P(\omega) = \alpha\omega \quad \forall \omega,$$

(3.13)

where $\alpha = \Delta D = \hat{D} - D$. Thus, a pure delay mismatch can be diagnosed if the entire magnitude spectrum of the PMR is equal to one while the phase spectrum of the PMR varies linearly and the degree of variation is equal to the degree of delay mismatch. The direction of the mismatch can be seen as inversely proportional to the gradient, α, therefore the direction diagnosis of the delay mismatch is:

$$\alpha > 0 \text{ if } D < \widehat{D}$$

$$\alpha < 0 \text{ if } D > \widehat{D}.$$

(3.14)

3.2.2.4　Gain and Time Constant Mismatch

For gain and time constant mismatches, the performance loss can be described due to the following:

- $K \neq \hat{K}$,
- $\tau \neq \hat{\tau}$, and
- $D = \hat{D}$.

Therefore, (3.1) will simplify to:

$$G_{PMR}(\omega) = \frac{|G(e^{j\omega})|e^{j\angle \underline{G}(e^{j\omega})}e^{-jD\omega}}{|\hat{G}(e^{j\omega})|e^{j\angle \underline{\hat{G}}(e^{j\omega})}e^{-j\hat{D}\omega}}$$

$$= \frac{K}{\hat{K}}\frac{(1-a)(1-e^{-j\omega}\hat{a})}{(1-\hat{a})(1-e^{-j\omega}a)} \qquad (3.15)$$

$$= M(\omega)e^{j\Delta P(\omega)}.$$

This will lead to the following magnitude and phase spectra components:

$$M(\omega) = \frac{K}{\hat{K}}\frac{(1-a)}{(1-\hat{a})}\sqrt{\frac{1-2\hat{a}\cos\omega+\hat{a}^2}{1-2a\cos\omega+a^2}}$$

$$\Delta P(\omega) = \tan^{-1}\left(\frac{\hat{a}\sin(\omega)}{1-\hat{a}\cos(\omega)}\right) - \tan^{-1}\left(\frac{a\sin(\omega)}{1-a\cos(\omega)}\right). \qquad (3.16)$$

From (3.16), the MPM will have the following effect on the PMR:

$$M(\omega)|_{\omega=0} \neq 1$$

$$M(\omega)|_{\omega=0} \neq M(\omega)_{\omega\neq 0}$$

$$\Delta P(\omega)|_{\omega=0,\pi} = 0 \qquad (3.17)$$

$$\Delta P(\omega)|_{\omega=0,\pi} \neq \Delta P(\omega)|_{\omega\neq 0,\pi}.$$

Therefore, the simplest way to identify MPM due to gain and time constant mismatches is to use the magnitude spectrum. The zero-frequency component should not be equal to one while the remaining magnitude spectrum will change over the remaining frequencies, following an adapted diagnosis from (3.6) and (3.11):

$$M(\omega)|_{\omega=0} > 1 \text{ if } K > \hat{K}$$

$$M(\omega)|_{\omega=0} < 1 \text{ if } K < \hat{K}$$

$$M(\omega)|_{\omega=\pi} < M(\omega)|_{\omega=0} \text{ if } \tau > \hat{\tau} \qquad (3.18)$$

$$M(\omega)|_{\omega=\pi} > M(\omega)|_{\omega=0} \text{ if } \tau < \hat{\tau}.$$

3.2.2.5   Gain and Delay Mismatch

Gain and delay mismatches are described using the following:

- $K \neq \hat{K}$,
- $\tau = \hat{\tau}$, and
- $D \neq \hat{D}$.

Therefore, (3.1) will simplify to:

$$G_{PMR}(\omega) = \frac{|G(e^{j\omega})|e^{j\angle \underline{G}(e^{j\omega})}e^{-jD\omega}}{|\hat{G}(e^{j\omega})|e^{j\angle \underline{\hat{G}}(e^{j\omega})}e^{-j\hat{D}\omega}}$$
$$= \frac{K}{\hat{K}}e^{-(D-\hat{D})j\omega},$$

(3.19)

thus, the gain mismatch will be captured in the magnitude spectrum of the PMR while the delay mismatch will be captured in the phase spectrum of the PMR. From this, the following condition will be true for a system with gain and delay mismatch:

$$M(\omega) \neq 1 \quad \forall \omega$$
$$\Delta P(\omega) = \alpha\omega \quad \forall \omega,$$

(3.20)

where $\alpha = \Delta D = \hat{D} - D$. Once the mismatch has been identified as a gain and delay mismatch, the following criteria can be used to indicate the extent (direction) of the mismatch:

$$M(\omega) > 1 \text{ if } K > \hat{K}$$
$$M(\omega) < 1 \text{ if } K < \hat{K}$$
$$\alpha > 0 \text{ if } D < \hat{D}$$
$$\alpha < 0 \text{ if } D > \hat{D}.$$

(3.21)

3.2.2.6 Time constant and delay mismatch

For time constant and delay mismatches, the following is true:

- $K = \hat{K}$,
- $\tau \neq \hat{\tau}$, and
- $D \neq \hat{D}$.

Therefore, (3.1) will simplify to:

$$G_{PMR}(\omega) = \frac{|G(e^{j\omega})|e^{j\angle \underline{G}(e^{j\omega})}e^{-jD\omega}}{|\hat{G}(e^{j\omega})|e^{j\angle \underline{\hat{G}}(e^{j\omega})}e^{-j\hat{D}\omega}}$$
$$= \frac{(1-a)(1-e^{-j\omega}\hat{a})}{(1-\hat{a})(1-e^{-j\omega}a)}e^{-j\Delta D\omega},$$

(3.22)

realizing the following magnitude and phase spectra of the PMR:

$$M(\omega) = \frac{|G(e^{j\omega})|e^{j\angle \underline{G}(e^{j\omega})}e^{-jD\omega}}{|\hat{G}(e^{j\omega})|e^{j\angle \underline{\hat{G}}(e^{j\omega})}e^{-j\hat{D}\omega}}$$
$$= \frac{(1-a)}{(1-\hat{a})}\sqrt{\frac{1-2\hat{a}\cos\omega+\hat{a}^2}{1-2a\cos\omega+a^2}}$$

(3.23)

$$\Delta P(\omega) = \tan^{-1}\left(\frac{\hat{a}\sin(\omega)}{1-\hat{a}\cos(\omega)}\right) - \tan^{-1}\left(\frac{a\sin(\omega)}{1-a\cos(\omega)}\right) + \omega(\Delta D).$$

From (3.23), the MPM will have the following effect on the PMR:

$$M(\omega)|_{\omega=0} = 1$$

$$M(\omega)|_{\omega=0} \neq M(\omega)|_{\omega \neq 0} \tag{3.24}$$

$$\Delta P(\omega) \approx f(\tau, \omega) = \alpha\omega + c,$$

where $f(\tau, \omega)$ represents a linear approximation of ΔP.

Therefore, the magnitude spectrum of the PMR should have a zero-frequency component not equal to one, with the magnitude spectrum over the remaining frequencies equal to the zero-frequency component. The phase spectrum should also vary linearly. The direction diagnosis for both the time constant and delay mismatches are similar to (3.11) and (3.14) respectively.

3.2.2.7 Gain, Time Constant, and Delay Mismatch

For gain, time constant and delay mismatches, the performance loss will be due to:

- $K \neq \hat{K}$,
- $\tau \neq \hat{\tau}$, and
- $D \neq \hat{D}$.

Therefore, (3.1) will simplify to:

$$\begin{aligned}
G_{PMR}(\omega) &= \frac{|G(e^{j\omega})|e^{j\angle \underline{G}(e^{j\omega})}e^{-jD\omega}}{|\hat{G}(e^{j\omega})|e^{j\angle \hat{G}(e^{j\omega})}e^{-j\hat{D}\omega}} \\
&= \frac{K}{\hat{K}}\frac{(1-a)(1-e^{-j\omega}\hat{a})}{(1-\hat{a})(1-e^{-j\omega}a)}e^{-j\Delta D\omega}.
\end{aligned} \tag{3.25}$$

From (3.25) the PMR will have the following magnitude and phase spectra:
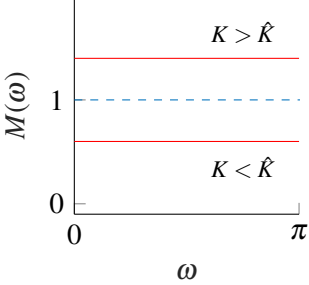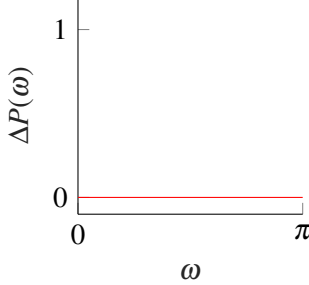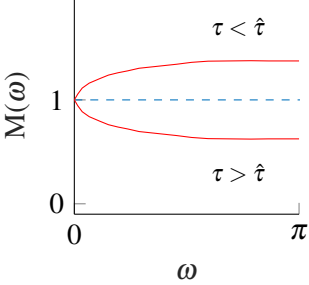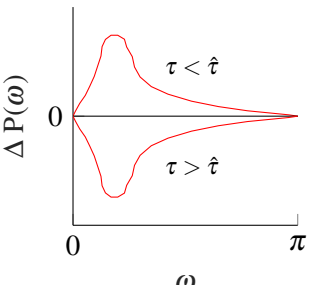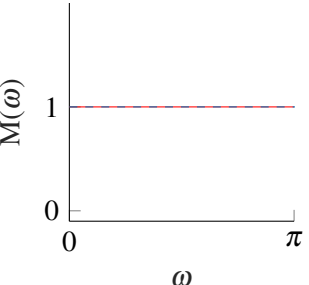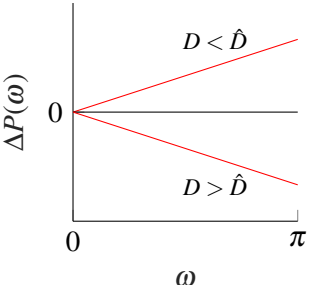
$$M(\omega) = \frac{K}{\hat{K}}\frac{(1-a)}{(1-\hat{a})}\sqrt{\frac{1-2\hat{a}\cos\omega+\hat{a}^2}{1-2a\cos\omega+a^2}}$$

$$\Delta P(\omega) = \tan^{-1}\left(\frac{\hat{a}\sin(\omega)}{1-\hat{a}\cos(\omega)}\right) - \tan^{-1}\left(\frac{a\sin(\omega)}{1-a\cos(\omega)}\right) + \omega(\Delta D). \tag{3.26}$$

From (3.26), the MPM will have the following effect on the PMR:

$$M(\omega)|_{\omega=0} \neq 1$$

$$M(\omega)|_{\omega=0} \neq M(\omega)|_{\omega \neq 0} \tag{3.27}$$

$$\Delta P(\omega) \approx f(\tau, \omega) = \alpha\omega + c,$$

where $f(\tau, \omega)$ represents a linear approximation of ΔP. The full diagnosis procedure can be seen in Table 3.3.

Table 3.1. Conditions to diagnose the type of mismatch among gain, time constant, and delay. Adapted from Selvanathan and Tangirala (2010a), with permission.

Type of mismatch	$M(\omega)$	$\Delta P(\omega)$
Gain mismatch $K \neq \widehat{K}$		
Time constant mismatch $\tau \neq \widehat{\tau}$		
Delay mismatch $D \neq \widehat{D}$		

3.2.2.8　PMR Methodology Summary
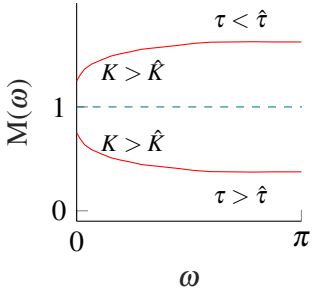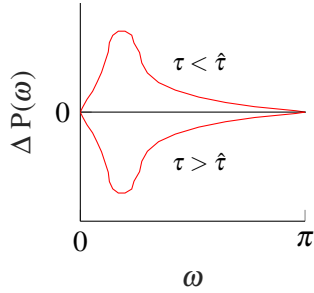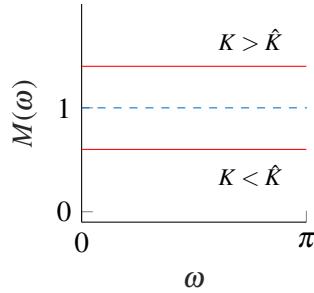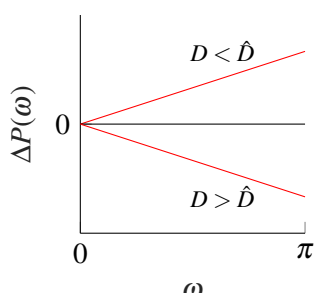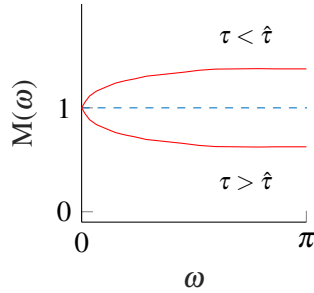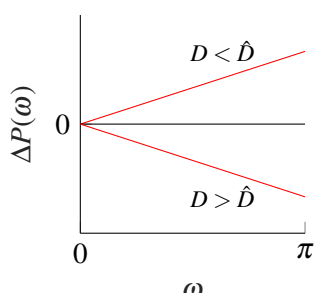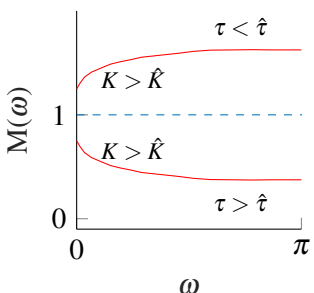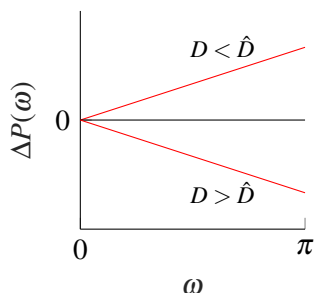
The PMR methodology can be summarized as well as generalized for all mismatch arrangements. Table 3.1 and Table 3.2 shows the conditions of MPM identification as described by Selvanathan and Tangirala (2010a).

From Table 3.1 and Table 3.2 as well as the development of the PMR, the systematic procedure in Table 3.3 can universally be used to identify MPM for FOPTD models.

3.2.3　Plant Model Ratio Estimation for SISO Systems

Recall that the PMR is defined as the ratio between the process transfer function G and the model transfer function $\widehat{G}$ as seen in (3.1). Due to process variation and non-linearity most process transfer

Table 3.2. Conditions to diagnose combinations of mismatches. Adapted from Selvanathan and Tangirala (2010a), with permission.

Type of mismatch	$M(\omega)$	$\Delta P(\omega)$
Gain and time constant mismatch $K \neq \widehat{K}$, $\tau \neq \widehat{\tau}$	$\tau < \hat{\tau}$; $K > \hat{K}$; $K > \hat{K}$; $\tau > \hat{\tau}$	$\tau < \hat{\tau}$; $\tau > \hat{\tau}$
Gain and delay mismatch $K \neq \widehat{K}$, $D \neq \widehat{D}$	$K > \hat{K}$; $K < \hat{K}$	$D < \hat{D}$; $D > \hat{D}$
Time constant and delay mismatch $\tau \neq \widehat{\tau}$, $D \neq \widehat{D}$	$\tau < \hat{\tau}$; $\tau > \hat{\tau}$	$D < \hat{D}$; $D > \hat{D}$
Gain, time constant, and delay mismatch $K \neq \widehat{K}$, $\tau \neq \widehat{\tau}$, $D \neq \widehat{D}$	$\tau < \hat{\tau}$; $K > \hat{K}$; $K > \hat{K}$; $\tau > \hat{\tau}$	$D < \hat{D}$; $D > \hat{D}$

functions will not be known apriori. To address this issue, the PMR can under certain conditions be estimated from routine operating data. These conditions include that the setpoint contains sufficient excitation and that the signal-to-noise ratio is also large enough to make reliable inferences (Yerramilli and Tangirala, 2018).

Table 3.3. MPM analysis using PMR.

	Assessment Procedure	**Diagnosis of MPM**	**MPM Direction**
Step 1	$M(\omega)\|_{\omega=0} \neq 1$	if $M(0) = 1$: $K = \hat{K}$, else $K \neq \hat{K}$	$M(\omega) > 1$ if $K > \hat{K}$, $M(\omega) < 1$ if $K < \hat{K}$
Step 2	$M(\omega)$ has a zero slope (flatness test)	if flat: $\tau = \hat{\tau}$, else $\tau \neq \hat{\tau}$	$M(\omega)\|_{\omega=\pi} < 1$ if $\tau > \hat{\tau}$ $M(\omega)\|_{\omega=\pi} > 1$ if $\tau < \hat{\tau}$
Step 3	Linearity check of $\Delta P(\omega)$	if $\alpha = 0$: $D = \hat{D}$, else $D \neq \hat{D}$	$\alpha > 0$ if $D < \hat{D}$ $\alpha < 0$ if $D > \hat{D}$

From the IMC structure in Figure 3.1, the process and model outputs can be defined as:

$$y(k) = Gu(k) + v(k) \tag{3.28}$$

$$\hat{y}(k) = \widehat{G}u(k). \tag{3.29}$$

Therefore, in a noise-free environment where $v(k) = 0$, the PMR estimation will be:

$$\frac{G(\omega)}{\widehat{G}(\omega)} = \frac{Y(\omega)}{\hat{Y}(\omega)}, \tag{3.30}$$

where $Y(\omega)$ and $\hat{Y}(\omega)$ are the Fourier transforms of y and $\hat{y}$ respectively. Nonetheless, for a practical system, the presence of noise (as seen in (3.28)) and disturbances are unavoidable and therefore a smoothed estimation of the PMR is desired. Building on an empirical transfer function estimation, the cross-spectral density (CSD) forms the foundation of the smoothed PMR estimation (Ljung, 1999; Selvanathan and Tangirala, 2010a):

$$\widehat{G}_{PMR} = \frac{\gamma_{y,r}(\omega)}{\gamma_{\hat{y},r}(\omega)}, \tag{3.31}$$

where $\gamma_{y,r}(\omega)$ is the CSD between the process output y and the setpoint r, while $\gamma_{\hat{y},r}(\omega)$ is the estimated CSD between the model output $\hat{y}$ and the setpoint r. This correlation between outputs and setpoint allows for the effects of noise and disturbances (which should be uncorrelated with the setpoint) to be removed from the PMR (Selvanathan and Tangirala, 2010a; Yerramilli and Tangirala, 2016).

3.3   THE IMPROVED PLANT MODEL RATIO

The delay mismatch detection described in Section 3.2 requires high-frequency excitation to estimate the delay mismatch as mentioned by Mittermaier et al. (2023); Selvanathan and Tangirala (2010a); Yerramilli and Tangirala (2016). An improvement on the PMR methodology as discussed below aims to mitigate the requirements for high-frequency excitation within a system. This is especially important for feedback control systems that usually act as low-pass filters that attenuate high-frequency excitation. The alleviation of the requirement for high-frequency excitation is achieved by estimating the delay

mismatch using a method of optimal delay estimation. The optimal delay estimation technique stems from the idea that the PMR is a transfer function between the process output (y) and the model output ($\hat{y}$), in a noise free environment, as depicted in Figure 3.2. Thus, the discrete PMR transfer function can be split into a delay-free term ($\underline{H}$) and a delay term ($z^{-\Delta D}$):

$$G_{PMR}(z) = \underline{H}z^{-\Delta D}. \tag{3.32}$$

The methodology, described below, is based on the delay estimation as discussed by Hamon and Hannan (1974), Lindemann et al. (2001) and Selvanathan and Tangirala (2010b).

3.3.1 Optimal Delay Estimation Methodology

An arbitrary discrete transfer function $H(z)$ can be split into a transfer function containing the delay-free portion of the system ($\underline{H}(z)$) and the delay of the system (z^{-D}):

$$H(z) = \underline{H}(z)z^{-D}. \tag{3.33}$$

The phase spectrum of the transfer function contains a contribution from both the time-delay and delay-free part of the transfer function:

$$\arg[H(\omega)] = \arg[\underline{H}(\omega)] - D(\omega), \tag{3.34}$$

where arg represents the angle of the complex number. Therefore, if the left-hand side and the delay-free contribution of (3.34) is known, the delay (D) can be estimated. The left-hand side of (3.34) can be estimated as previously stated, by using the linear system relation:

$$H(\omega) = \frac{\gamma_{yu}(\omega)}{\gamma_{uu}(\omega)}, \tag{3.35}$$

where $\gamma_{yu}(\omega)$ is the CSD and $\gamma_{uu}(\omega)$ is the auto-spectral-density of the variables in each subscript.

The delay-free term of (3.34) ($\arg[\underline{H}(\omega)]$) can be estimated without having to estimate $\underline{H}(\omega)$ by considering the fact that the magnitude of the delay-free term and the magnitude of the complete transfer function (left-hand side of (3.34)) are identical:

$$|H(\omega)| = |\underline{H}(\omega)|. \tag{3.36}$$

Therefore, the delay can be estimated using (3.34) without the delay factorization as shown in (3.33).

Using the transfer function estimate shown in (3.35), the Hilbert transform relation can be used to obtain the argument of the transfer function (Oppenheim, 1999):

$$\arg[F(\omega)] = -\frac{1}{2\pi} \int_{-\pi}^{\pi} \log|F(\theta)| \left[\cot\left(\frac{\omega-\theta}{2}\right) + \cot\left(\frac{\omega+\theta}{2}\right) \right] d\theta, \qquad (3.37)$$

where $F(.)$ is a linear time-invariant minimum-phase causal system. Therefore, assuming that $\underline{H}(\omega)$ is a minimum phase system, setting $F(\omega) = \underline{H}(\omega)$ and discretizing the integral in (3.37), the argument of the delay-free part in (3.34) can be approximated as (Lindemann et al., 2001):

$$\arg[\underline{H}(\omega_l)] = -\frac{1}{2B} \sum_{k=1, k \neq l}^{B} \log|H(\omega_k)| \left(\cot\left(\frac{\omega_l - \omega_k}{2}\right) + \cot\left(\frac{\omega_l + \omega_k}{2}\right) \right), \qquad (3.38)$$

where, ω_l is the frequency in question, while ω_k forms a moving window of frequencies within a bandwidth of frequencies denoted B.

The estimates of $\arg[H(\omega)]$ as in (3.35), and $\arg[\underline{H}(\omega)]$ as in (3.38) can be substituted in (3.34) to form the following error function:

$$\varepsilon(\omega) = \arg[\widehat{H}(\omega)] - \arg[\underline{\widehat{H}}(\omega)] + (D)\omega. \qquad (3.39)$$

From the error function the delay (D) can be solved by obtaining the solution to the following cost function as proposed by Hamon and Hannan (1974):

$$\max_D J(D) = \sum_B W(\omega)\cos(\varepsilon(\omega)), \qquad (3.40)$$

where W is the weighting function as defined in (3.42).

When the error term of (3.39) tends to zero, the cosine function in (3.40) will reach a peak value. Therefore, the cost function searches for the integer value of D that realizes the maximum value of the cost function over the same bandwidth, B, as in (3.38). The bandwidth is a proper band of normalized frequencies $[0, \pi/T_s]$, where T_s is the sampling rate.

The weighting function of the objective function is derived from a least-squares approach (Ljung, 1999) with the aim of applying a bias to the objective function that is inversely proportional to the variance of the phase spectral estimate per normalized frequency. As described by Lindemann et al. (2001), when using the smoothed periodogram method to estimate the phase spectra, the variance of the phase estimate will be:

$$\text{var}(\arg[\widehat{H}(\omega)]) = \frac{1}{\nu}\left(\frac{1}{\kappa^2(\omega)} - 1\right), \qquad (3.41)$$

where v is the analogous degrees of freedom and $\kappa^2(\omega)$ is the magnitude-squared coherence between the input and output of the system. The weighting function $W(\omega)$ is chosen based on the weighted least-squares as:

$$W(\omega) = \frac{\kappa^2(\omega)}{1 - \kappa^2(\omega)}. \tag{3.42}$$

Combining the weighting function in (3.42) with the error function in (3.39) and the objective function in (3.40), a non-linear integer optimization problem should be solved to estimate the delay D. Seeing that in an actual real-world process, the expected delay variability due to MPM tends to be small, the non-linear integer optimization can be simplified to a standard search over a predetermined variable set of plausible integers, for example, $D \in [-10, 10]$.

3.3.2 Application to the PMR

The previously developed method for the optimal estimation of delay terms, described in Section 3.3.1, can be directly applied to the PMR by substituting the LTI system of interest ($H(\omega)$) in Section 3.3.1) with the PMR as defined in (3.2). Since the PMR is also an LTI system, the PMR can be written as a product of a delay-free term and a time delay term:

$$G_{PMR}(z) = \underline{G_{PMR}}(z)z^{-\Delta D}, \tag{3.43}$$

where $\Delta D = D - \hat{D}$. Applying the Hilbert transform relation (seen in (3.37)) to the PMR will realize the estimate of $\arg[\underline{G_{PMR}}(\omega)]$:

$$\arg\left[\,\underline{G_{PMR}}(\omega_l)\,\right] = -\frac{1}{2M}\sum_{k=1,k\neq l}^{M}\log|\,G_{PMR}(\omega_k)\,|\left(\cot\left(\frac{\omega_l - \omega_k}{2}\right) + \cot\left(\frac{\omega_l + \omega_k}{2}\right)\right). \tag{3.44}$$

Therefore, the delay mismatch can be estimated by solving the following optimization problem:

$$\Delta\widehat{D} = \arg\max_{\Delta D}\sum_{B}W(\omega)\cos\left(\arg[G_{PMR}(\omega)] - \arg[\underline{G_{PMR}}(\omega)] + \Delta D\omega\right). \tag{3.45}$$

It should be noted that the developed method operates under the assumption that the setpoint contains sufficient excitation and that the signal-to-noise ratio is also large enough to make reliable inferences (Yerramilli and Tangirala, 2018). As mentioned before, the improved PMR approach does not require high-frequency excitation as low-frequency excitation is sufficient to assure positive results. For the best analysis, the frequencies used in the delay estimation methodology should be limited to the range of frequencies over which the closed-loop system was excited. The useable frequency range can easily be obtained using a frequency analysis of the setpoint signal. Since most real-world systems, operating under an advanced control scheme will include the use of a real-time optimization layer that will introduce some setpoint variations, the low-frequency excitation requirement of the improved PMR

Table 3.4. MPM analysis using Improved PMR.

	Assessment Procedure	**Diagnosis of MPM**	**MPM Direction**
Step 1	$M(\omega)\|_{\omega=0} \neq 1$	if $M(0)=1$: $K = \hat{K}$, else $K \neq \hat{K}$	$M(\omega) > 1$ if $K > \hat{K}$, $M(\omega) < 1$ if $K < \hat{K}$
Step 2	$M(\omega)$ has a zero slope (flatness test)	if flat: $\tau = \hat{\tau}$, else $\tau \neq \hat{\tau}$	$M(\omega)\|_{\omega=\pi} < 1$ if $\tau > \hat{\tau}$ $M(\omega)\|_{\omega=\pi} > 1$ if $\tau < \hat{\tau}$
Step 3	Optimal delay mismatch detection	if $\alpha = 0$: $D = \hat{D}$, else $D \neq \hat{D}$	$\Delta D < 0$ if $D < \hat{D}$ $\Delta D > 0$ if $D > \hat{D}$

method does not restrict the control of the system nor is it an unrealistic expectation for an industrial closed-loop system (Seborg et al., 2016).

Given the development of the improved PMR for the estimation of delay mismatch in an optimal fashion, as well as the mitigation of the high-frequency excitation requirement, the systematic procedure in Table 3.4 can be used to identify MPM.

3.4   PLANT MODEL RATIO FOR MIMO SYSTEMS

The most prominent difference between SISO and MIMO systems is that for a MIMO system, the model and plant transfer functions are matrices, with the matrix elements being SISO transfer functions between individual input/output channels:

$$G = \begin{bmatrix} G_{11} & G_{12} & \cdots & G_{1j} \\ G_{21} & G_{22} & \cdots & G_{2j} \\ \vdots & \vdots & \ddots & \vdots \\ G_{i1} & G_{i2} & \cdots & G_{ij} \end{bmatrix}. \tag{3.46}$$

The objective of the PMR when applied to a MIMO system would be to isolate the MPM to a specific transfer function within the MIMO transfer function matrix and apply the SISO PMR diagnosis procedure (Table 3.4) to each element in the matrix. Seeing that the SISO PMR, as described in (3.1), cannot be directly applied to MIMO systems in a trivial way, a novel approach to the MIMO PMR is developed, by Yerramilli and Tangirala (2016), from the IMC structure in Figure 3.1. The plant output y_i can be expressed in terms of the model output $\hat{y}_i$:

$$y_i(\omega) = \sum_{k=1}^{n} G_{ik}(\omega)u_k(\omega) + d_i(\omega)$$

$$= \sum_{k=1}^{n} G_{PMR_{ik}}(\omega)\hat{G}_{ik}(\omega)u_k(\omega) + d_i(\omega) \tag{3.47a}$$

$$= \sum_{k=1}^{n} G_{PMR_{ik}}(\omega)\hat{y}_{ik}(\omega) + d_i(\omega), \tag{3.47b}$$

where $\hat{y}_{ik}$ is the k-th component, of the i-th model output ($\hat{y}_i$), corresponding to the k-th input u_k. Thus, for an $n \times n$ MIMO system, the element-wise division between the plant and model transfer function matrices defines the PMR matrix (Yerramilli and Tangirala, 2016, 2018):

$$G_{PMR}(\omega) = \begin{bmatrix} \frac{G_{11}(\omega)}{\hat{G}_{11}(\omega)} & \frac{G_{12}(\omega)}{\hat{G}_{12}(\omega)} & \cdots & \frac{G_{1n}(\omega)}{\hat{G}_{1n}(\omega)} \\ \vdots & \vdots & \ddots & \vdots \\ \frac{G_{n1}(\omega)}{\hat{G}_{n1}(\omega)} & \frac{G_{n2}(\omega)}{\hat{G}_{n2}(\omega)} & \cdots & \frac{G_{nn}(\omega)}{\hat{G}_{nn}(\omega)} \end{bmatrix}$$

$$= \begin{bmatrix} G_{PMR_{11}} & G_{PMR_{12}} & \cdots & G_{PMR_{1j}} \\ \vdots & \vdots & \ddots & \vdots \\ G_{PMR_{i1}} & G_{PMR_{i2}} & \cdots & G_{PMR_{ij}} \end{bmatrix}. \tag{3.48}$$

3.4.1 MIMO PMR Estimation From Operational Data

As discussed in Section 3.2.3, the process transfer function will seldom be known apriori, thus, the MIMO PMR could be estimated using routine operational data under certain conditions. If the inputs are uncorrelated, i.e., the transfer function matrix of (3.46) is a diagonal matrix, the plant model ratio can be described as (Yerramilli and Tangirala, 2016, 2018):

$$G_{PMR_{ij}}(\omega) = \frac{\gamma_{y_i,\hat{y}_{ij}}(\omega)}{\gamma_{\hat{y}_{ij},\hat{y}_{ij}}(\omega)}, \tag{3.49}$$

where the i-th row of the PMR matrix in (3.48) is interpreted as a transfer function between the n components of the model output $\hat{y}_i$ and the plant output y_i. Since most MIMO industrial systems do not have a diagonal transfer function matrix and significant correlations exist between all inputs and all outputs, the PMR in (3.49) does not hold true due to the confounding effect, i.e., the PMR in a particular channel is also influenced by contributions of inputs/outputs from other channels (Yerramilli and Tangirala, 2018).

The confounding effect between correlated channels can be mitigated using a partial cross-spectral density (PCSD) analysis (discussed in Section 3.4.2). The PCSD allows the numerical decoupling of the system by using conditioned signals. These conditioned signals can be interpreted as residual signals after the effects of confounding variables have been accounted for as described by Priestley (1981).

The PCSD can be used either as an explicit or implicit method to decouple the confounding signals within the system when estimating the MIMO PMR. The explicit method, based on partial statistics,

is described in Section 3.4.3, while the implicit method, based on linear regression is described in Section 3.4.4.

3.4.2 Partial Cross-Spectral Density

The PCSD, sometimes referred to as the conditioned CSD, is the frequency domain analogue of the partial covariance function and is used to calculate the CSD between two datasets after the effects of a third dataset are removed Priestley (1981).

To obtain the PCSD between x and y, given z, first obtain the two conditioned signals:

$$\psi_{x|z}(t) = x(t) - \sum_{k=-\infty}^{\infty} b_1(k)z(t-k) \tag{3.50a}$$

$$\psi_{y|z}(t) = y(t) - \sum_{k=-\infty}^{\infty} b_2(k)z(t-k), \tag{3.50b}$$

where $b_1(k)$ and $b_2(k)$ are determined by minimizing the expectation operators $E[\psi_{x|z}^2(t)]$ and $E[\psi_{y|z}^2(t)]$ respectively. The frequency-domain representation of the conditioned signals in (3.50) are:

$$\Psi_{x|z}(\omega) = X(\omega) - B_1(\omega)Z(\omega) \tag{3.51a}$$

$$\Psi_{y|z}(\omega) = Y(\omega) - B_2(\omega)Z(\omega). \tag{3.51b}$$

The transfer functions for b_1 and b_2 are:

$$B_1(\omega) = \sum_{k=-\infty}^{\infty} b_1(k)e^{-j\omega k} = \frac{\gamma_{x,z}(\omega)}{\gamma_{z,z}(\omega)} \tag{3.52a}$$

$$B_2(\omega) = \sum_{k=-\infty}^{\infty} b_2(k)e^{-j\omega k} = \frac{\gamma_{y,z}(\omega)}{\gamma_{z,z}(\omega)}. \tag{3.52b}$$

The PCSD is found by evaluating the CSD between $\Psi_{x|z}$ and $\Psi_{y|z}$. Thus, the PCSD between x and y given z can be defined as:

$$\begin{aligned}
\gamma_{x,y|z}(\omega) = &\gamma_{x,y}(\omega) - B_1(\omega)\gamma_{z,y}(\omega) - B_2^*(\omega)\gamma_{x,z}(\omega) + B_1(\omega)B_2^*(\omega)\gamma_{z,z}(\omega) \\
= &\gamma_{x,y}(\omega) - \frac{\gamma_{x,z}(\omega)\gamma_{z,y}(\omega)}{\gamma_{z,z}(\omega)},
\end{aligned} \tag{3.53}$$

where B_2^* is the complex conjugate of B_2.

3.4.3 Explicit MIMO PMR Estimation

Using operational data, along with the PCSD, a decoupled estimation of the PMR matrix in (3.48) can be derived. From (3.47) it is clear that for an $n \times n$ system, the confounding variables between a specific plant output and the corresponding model output are the residual $(n-1)$ contributions to the model output of the same row in the transfer function matrix. The PCSD allows for the estimation of the decoupled PMR by removing the effects of the confounding variables for a specific component in

Department of Electrical, Electronic and Computer Engineering   29
University of Pretoria

the PMR matrix:

$$\widehat{G}_{PMR_{ij}}(\omega) = \frac{\gamma_{y_i,\hat{y}_{ij}|\mathbf{Z}}(\omega)}{\gamma_{\hat{y}_{ij},\hat{y}_{ij}|\mathbf{Z}}(\omega)}, \tag{3.54}$$

where $\mathbf{Z} = \{\hat{y}_{ik}|k \in (1,...n), k \neq j\}$.

The decoupled PMR for an $n \times n$ system equates to n^2 SISO PMR systems. Each decoupled SISO PMR sub-system is characterized by a unique input-output relationship. Thus, the SISO PMR analysis and systematic test of Table 3.4 can be applied to each entry of the PMR matrix.

3.4.4 Implicit MIMO PMR Estimation

The implicit method of estimating the PMR uses a multiple regression approach on (3.47) by firstly correlating both sides with all setpoints. The correlation will realize n equations for n entries for each row of the MIMO PMR matrix as seen below in (3.55). The correlation step mitigates the effects of disturbances and noise as explained in Section 3.2.3.

$$\begin{bmatrix} \gamma_{y_i,r_1}(\omega) \\ \gamma_{y_i,r_2}(\omega) \\ \vdots \\ \gamma_{y_i,r_n}(\omega) \end{bmatrix} = \begin{bmatrix} \gamma_{\hat{y}_{i1},r_1}(\omega) & \gamma_{\hat{y}_{i2},r_1}(\omega) & \dots & \gamma_{\hat{y}_{in},r_1}(\omega) \\ \gamma_{\hat{y}_{i1},r_2}(\omega) & \gamma_{\hat{y}_{i2},r_2}(\omega) & \dots & \gamma_{\hat{y}_{in},r_2}(\omega) \\ \vdots & \vdots & \ddots & \vdots \\ \gamma_{\hat{y}_{i1},r_n}(\omega) & \gamma_{\hat{y}_{i2},r_n}(\omega) & \dots & \gamma_{\hat{y}_{in},r_n}(\omega) \end{bmatrix} \begin{bmatrix} G_{PMR_{i1}}(\omega) \\ G_{PMR_{i2}}(\omega) \\ \vdots \\ G_{PMR_{in}}(\omega) \end{bmatrix}. \tag{3.55}$$

Therefore, elements of the i-th row of the PMR matrix can be estimated via regression and the steps should be repeated for each row of the PMR matrix. It should be noted that the values in (3.55) are complex and frequency dependent. Therefore, the transpose operation for solving the linear algebra problem should be replaced by their conjugate-transpose counterparts and should be calculated for each frequency within the bandwidth B (Yerramilli and Tangirala, 2018).

The implicit method of estimating the PMR matrix realizes a matrix of SISO PMR transfer functions homogeneous to the SISO PMR transfer function in (3.31). Therefore, the SISO analysis and systematic test of Table 3.4 can be applied to each entry of the PMR matrix. The simplified nature of the implicit MIMO PMR estimation makes it a more favourable method as compared to the explicit MIMO PMR estimation.

3.5 PLANT MODEL RATIO CONSIDERATIONS AND LIMITATIONS

Three items should initially be taken note of in regard to the application of the PMR:

1. Since the PMR is fundamentally based on a frequency analysis, sufficient broadband setpoint excitation is required. A single-frequency sinusoidal wave will propagate only a single frequency

through the system which will lead to a lack of information over a band of frequencies in the PCSD (Priestley, 1981).

2. If the model used to describe the system is not a deviation variable model as described by Skogestad and Postlethwaite (2010), where all operations of the system are centred about zero, the operating point of each variable within the system should be subtracted from the recorded data. Eliminating the offset in data will remove the corresponding lower frequency components that overpower the CSD and ensure accurate results for the PMR.

3. The PMR is developed as a ratio between the plant transfer function and the model transfer function. This ratio is then estimated using a cross-spectral density between the reference signal of the entire system and either the plant or model outputs. Therefore the PMR will diagnose the MPM irrespective of the controller performance. From this, the controller performance is omitted from the dissertation to ensure a concise discussion of the obtained results.

3.6   CHAPTER SUMMARY

The focus of this chapter was to describe the theory of the PMR. The frequency-based nature of the PMR was used to develop an MPM diagnosis procedure. The diagnosis procedure includes the diagnosis for gain, time constant and delay mismatched for FOPTD transfer functions.

The development of the PMR was succeeded by a method to estimate the SISO PMR from routine operational data. To mitigate the requirement for high-frequency excitation, the PMR was improved by incorporating an optimal delay estimation method. Finally, SISO PMR is expanded to a MIMO case by developing a decoupling mechanism that equates to a MIMO PMR matrix to which the SISO PMR can be applied directly.

CHAPTER 4   METHODOLOGY VERIFICATION AND SIMULATION STUDY

4.1   CHAPTER OVERVIEW

This chapter will focus on the evaluation of the PMR on a number of different SISO and MIMO processes. The SISO PMR case is evaluated in Section 4.2, followed by the evaluation of the MIMO PMR case in Section 4.3.

In Section 4.2.1 the process description of the system used to evaluate the SISO PMR is presented. The process description is followed by the controller design and simulation description for the SISO PMR evaluation in Section 4.3.2. The following permutations of MPM were used:

- A baseline simulation in Section 4.2.3.
- Gain mismatches in Section 4.2.4.
- Time constant mismatches in Section 4.2.5.
- Delay mismatches in Section 4.2.6.
- A combination of mismatches in Section 4.2.7.

A description of the process used to evaluate the MIMO PMR can be found in Section 4.3.1, followed by two scenarios for evaluating the MIMO PMR in Section 4.3.3 and Section 4.3.4.

4.2   INVESTIGATION OF THE PMR FOR SISO SYSTEMS

4.2.1   Process Description

To evaluate the PMR for SISO systems as derived in Section 3.2, a controllable pressure tank system is used as described by Bagyaveereswaran et al. (2016). The system consists of a single inflow and a single outflow connected to the pressure tank as depicted in Figure 4.1.

Open loop step tests were applied to the pressure control system, in Figure 4.1, by varying the outflow from the tank, keeping the inflow constant and recording the tank pressure. A FOPTD transfer function was fitted to the process data realizing the following representation of the pressure control system:

$$G(s) = \frac{1.01e^{-0.5s}}{18.42s + 1}. \tag{4.1}$$

MPM within the system can stem from either non-linearities or hardware malfunctions, thus, the system will be a suitable candidate to test the PMR functionality.

4.2.2 Controller Design and Simulation Description

4.2.2.1 Controller Design

The plant of (4.1) will be controlled using a standard MPC controller (Qin and Badgwell, 2003). The controller is a linear constrained MPC controller with an unconstrained Kalman-filter to estimate the states of the system from the plant outputs (Grewal and Andrews, 2001). Using a zero-order hold function with a sampling time of 0.5 seconds, the plant in (4.1) could be discretized:

$$G(z) = \frac{0.02705z^{-1}}{z - 0.9732}. \tag{4.2}$$

A third-order Padé approximation of the time delay was used to realize the discrete state-space representation of (4.2) (Trefethen, 2019):

$$x_{k+1} = Ax_k + Bu_k \tag{4.3a}$$

$$y_k = Cx_k + Du_k \tag{4.3b}$$
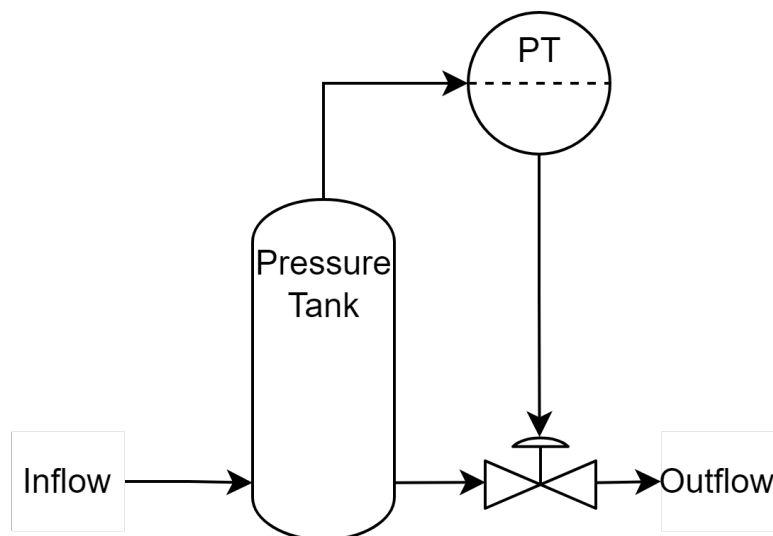
Figure 4.1. Pressure control system. Adapted from Zheng et al. (2009), with permission.

with

$$A = \begin{bmatrix} -0.3333 & -0.1667 \\ 0.125 & 0 \end{bmatrix} \tag{4.3c}$$

$$B = \begin{bmatrix} 0.5 \\ 0 \end{bmatrix} \tag{4.3d}$$

$$C = \begin{bmatrix} -0.1667 & 0.3333 \end{bmatrix} \tag{4.3e}$$

$$D = \begin{bmatrix} 0 \end{bmatrix} . \tag{4.3f}$$

Both the MPC and the Kalman-filter uses this state space description. The linear MPC is formulated as:

$$\mathbf{u} = \arg\min J\left(\mathbf{u}^{N_C}\right), \tag{4.4a}$$

given that,

$$J\left(\mathbf{u}^{N_C}\right) = \sum_{j=1}^{N_P} \left\| \mathbf{e}_{k+j}^{y} \right\|_{\mathbf{Q}} + \sum_{j=0}^{N_C-1} \left\| \Delta\mathbf{u}_{k+j} \right\|_{\mathbf{R}}, \tag{4.4b}$$

subject to

$$\mathbf{x}_{k+j} = \mathbf{A}\left(\mathbf{x}_{k+j-1}\right) + \mathbf{B}\left(\mathbf{u}_{k+j-1}\right) \quad \forall j = 1, N_p$$

$$\mathbf{y}_{k+j} = \mathbf{C}\left(\mathbf{x}_{k+j-1}\right) + \mathbf{D}\left(\mathbf{u}_{k+j-1}\right) \quad \forall j = 1, N_p$$

$$\underline{\mathbf{u}} \leq \mathbf{u}_{k+j} \leq \overline{\mathbf{u}} \quad \forall j = 0, N_C - 1, \tag{4.4c}$$

$$\Delta\underline{\mathbf{u}} \leq \Delta\mathbf{u}_{k+j} \leq \Delta\overline{\mathbf{u}} \quad \forall j = 0, N_C - 1.$$

The prediction horizon (N_p) is chosen as 10 while the control horizon (N_c) is chosen as 2. The objective function weights are $Q = 1$ and $R = 0.1$ respectively. The plant is controlled to the extent that no constraints are reached. The Kalman-filter is designed using a constant Kalman gain (K_n), defined as:

$$K_n = P_{n,n1}H^T\left(HP_{n,n-1}H^T + R_n\right)^{-1}, \tag{4.5}$$

where $P_{n,n-1}$ is the prior estimate covariance matrix of the current state (predicted at the previous step), H is the observation matrix and R_n is the measurement noise covariance matrix.

4.2.2.2 Simulation Description

The simulation of the plant uses the simulation structure seen in Figure 4.2. Both the plant and model outputs are logged for use with the PMR algorithm along with the setpoint. The addition

---
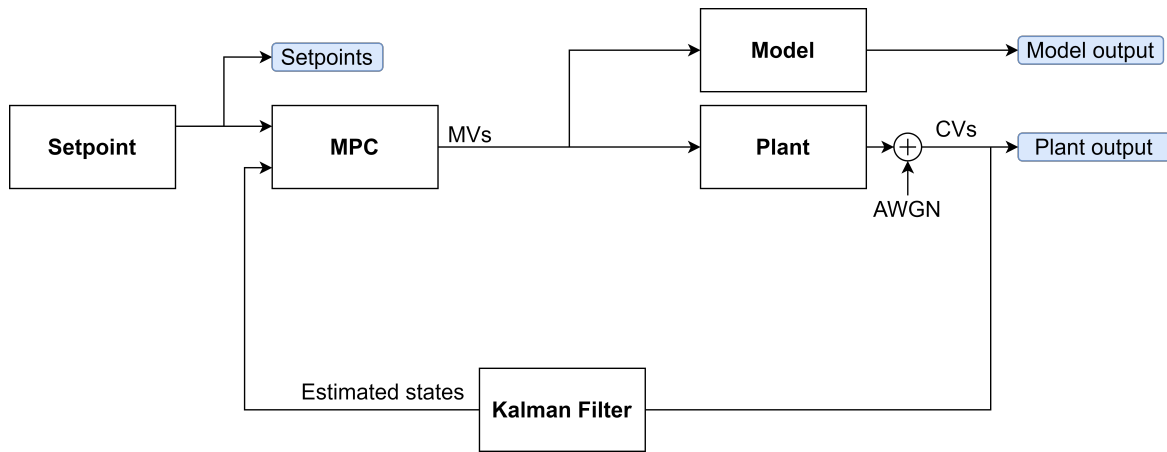
Figure 4.2. SISO simulation study feedback loop.

of the Kalman-filter to estimate the states for the MPC controller can be seen as synonymous with

Figure 3.1.

To ensure that the required excitation is applied to the process, a pseudo-random binary sequence, with a maximum switching time of 10 times the sampling rate (maximum switching time $= 10 \times T_s$), is used as a setpoint reference. An additive white Gaussian noise (AWGN) signal, with a power-to-noise ratio of 0.1, is added to the plant output to simulate measurement noise. The implicit PMR estimation, as discussed in subsection 3.4.4, was used.

4.2.3   Baseline Simulation of Methodology

To ensure the method does not detect false positives, the first simulation is done with zero MPM. This will allow a baseline performance analysis before MPM scenarios are investigated.

The improved PMR as described in Section 3.2.3 is applied to the process data. The MPM analysis from Table 3.3 can be used to quantify the amount of mismatch present between the process and the model.
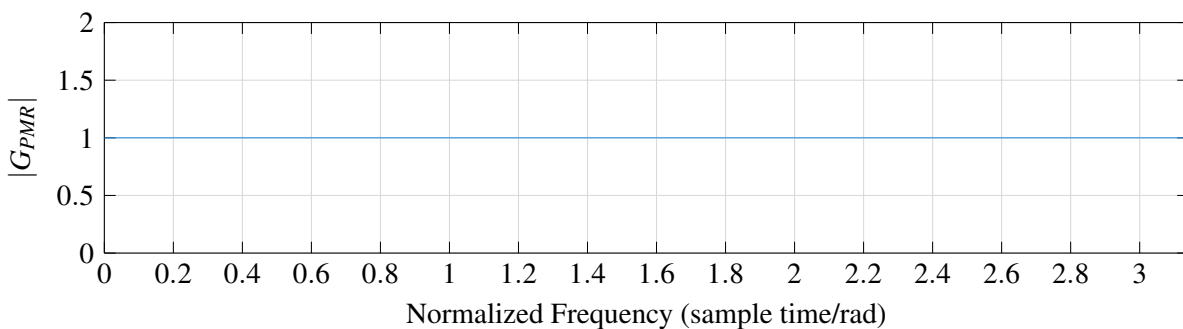
Figure 4.3. PMR magnitude spectra for the baseline simulation.
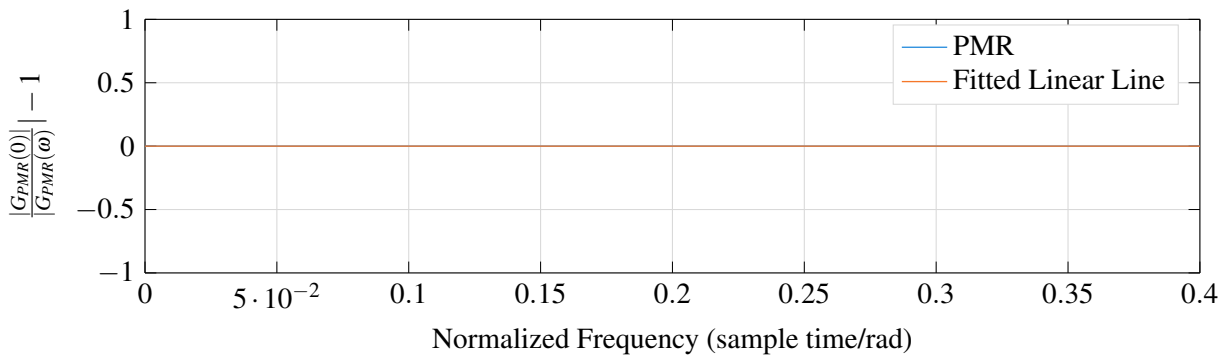
Figure 4.4. Initial slope of PMR magnitude spectra for the baseline simulation.

The first step is to test if the zero-frequency component of the magnitude spectra of the PMR is equal to 1. From the graph of the PMR magnitude spectra, seen in Figure 4.3, it is evident that there is no MPM in the gain term of the transfer function. It should be noted that no noise is visible in Figure 4.3 seeing that the cross-spectral density used to estimate the PMR allowed the noise to be suppressed to a level not visible on the graph.

The second step of the diagnosis procedure is to do a linearity check on the initial slope of the magnitude spectra of the PMR. The blue line in Figure 4.4 shows a graph of the rate of change of the magnitude spectrum between the normalized frequencies of 0 and 0.4 (the range recommended by Yerramilli and Tangirala (2016)). The orange line is a linear graph fitted to the blue line, over the normalized frequencies of 0 and 0.4, and the slope of the orange line is used to detect the initial slope of the PMR magnitude spectrum to quantify the time constant mismatch present. Seeing that the slope of the orange line is zero, it is evident that there is no time constant mismatch present.

The last step, used to determine the mismatch in delay term, follows the improved delay estimation as described in Section 3.3. The calculated cost function per ΔD is displayed in Table 4.1 where $\emptyset$ represents an undefined solution to the cost function. From this table, it is evident that there is no MPM present in the delay term as the maximum of the cost function in (3.45) is for $\Delta D = 0$. Recall that the weighting function used in the cost function of the optimal delay estimation, as seen in

Table 4.1. Objective function results for the baseline simulation.

ΔD	-5	-4	-3	-2	-1	0	1	2	3	4	5
Cost Function	$\emptyset$	$\emptyset$	$\emptyset$	$\emptyset$	$\emptyset$	$J(D) \to \infty$	$\emptyset$	$\emptyset$	$\emptyset$	$\emptyset$	$\emptyset$

(3.42), is:

$$W(\omega) = \frac{\kappa^2(\omega)}{1 - \kappa^2(\omega)},$$

(4.6)

where $\kappa^2(\omega)$ is the magnitude-squared coherence between the input and output of the system. For a system with no delay mismatch, the magnitude-squared coherence will be 1, resulting in an infinitely large weighting function when numerically calculated. This coupled with the nature of the cosine function in the cost function will lead to the results in Table 4.1.

4.2.4 Simulation of Gain Mismatch

To independently test the ability of the PMR to detect gain mismatches from process data, the following mismatches will be applied to the plant in (4.1):

1. A gain increase of 10%: $G(s) = \frac{1.111e^{-0.5s}}{18.42s+1}$
2. A gain decrease of 25%: $G(s) = \frac{0.7575e^{-0.5s}}{18.42s+1}$
3. A gain increase of 50%: $G(s) = \frac{1.515e^{-0.5s}}{18.42s+1}$

4.2.4.1 +10% Gain Mismatch

From Figure 4.5, it is evident that the zero-frequency component is equal to 1.1, indicating a +10% mismatch in the gain term. The slope of the linear line fitted to the initial rate of change of the magnitude spectra of the PMR (Figure 4.6) indicates a flat initial slope with a value of -1.0270×10^{-16}, and therefore it can be concluded that there is no MPM within the time constant term of the transfer function. Finally, the cost function values from (3.45) are identical to those in Table 4.1 and therefore no delay mismatch is detected. This diagnosis can be summarized, as seen in Table 4.2, following the structure of Table 3.4.

Table 4.2. MPM diagnosis for +10% gain mismatch.

	Assessment Procedure	Diagnosis of MPM
Step 1	$M(\omega)\|_{\omega=0}$	From Figure 4.5, the zero-frequency component of the magnitude spectra is 1.1, indicating a +10% MPM in gain.
Step 2	$M(\omega)$ initial slope flatness test	From Figure 4.6, the slope can be seen as approximately flat, with the slope of the fitted line equal to -1.0270×10^{-16}. Therefore, no MPM in time constant is present.
Step 3	Optimal delay mismatch detection	The results for the optimal delay estimation is identical to that summarized in Table 4.1, and therefore no MPM in the delay is present.

Figure 4.5. PMR magnitude spectra for a +10% gain mismatch applied to a SISO system.
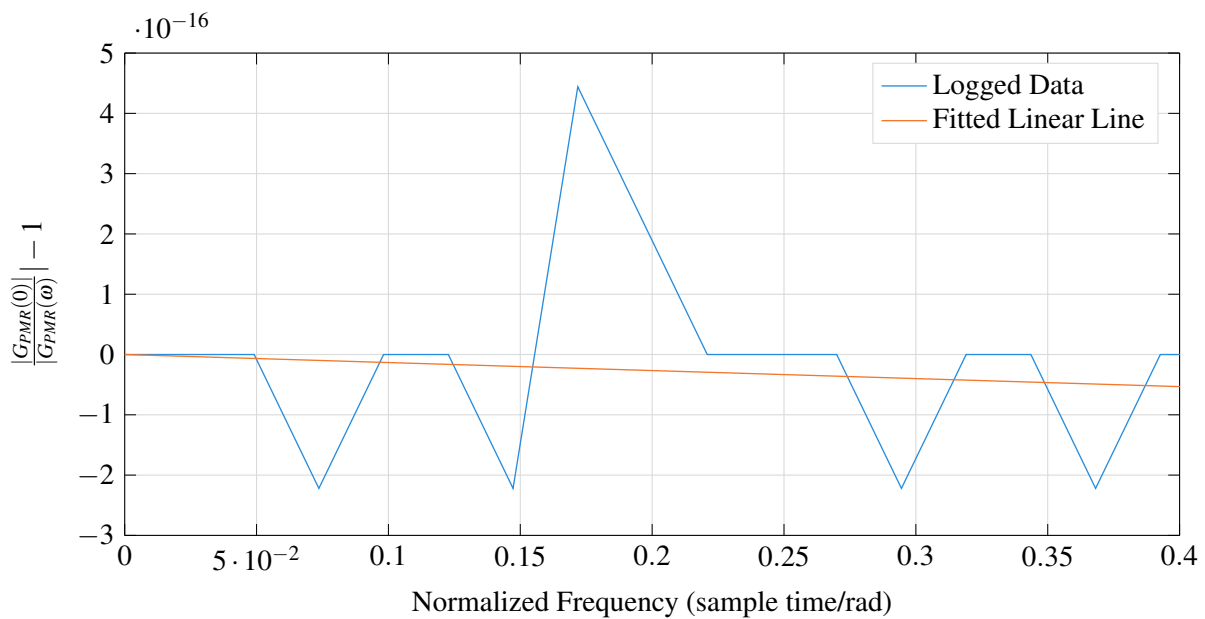
Figure 4.6. Initial slope of PMR magnitude spectra for a +10% gain mismatch applied to a SISO system.

4.2.4.2 -25% Gain Mismatch

The diagnosis procedure, as described in Table 3.4, can be followed to diagnose the MPM for the -25% change in gain as seen in Table 4.3.

Figure 4.7. PMR magnitude spectra for a -25% gain mismatch applied to a SISO system.

Figure 4.8. Initial slope of PMR magnitude spectra for a -25% gain mismatch applied to a SISO system.

Table 4.3. MPM diagnosis for -25% gain mismatch.

	Assessment Procedure	Diagnosis of MPM
Step 1	$M(\omega)|_{\omega=0}$	From Figure 4.7, the zero-frequency component of the magnitude spectra is 0.75, indicating a -25% MPM in gain.
Step 2	$M(\omega)$ initial slope flatness test	From Figure 4.8, the slope can be seen as approximately flat, with the slope of the fitted line equal to 9.3363×10^{-18}. Therefore, no MPM in time constant is present.
Step 3	Optimal delay mismatch detection	The results for the optimal delay estimation is identical to that summarized in Table 4.1, and therefore no MPM in delay is present.

Table 4.4. MPM diagnosis for 50% gain mismatch.

	Assessment Procedure	Diagnosis of MPM
Step 1	$M(\omega)\|_{\omega=0}$	From Figure 4.9, the zero-frequency component of the magnitude spectra is 1.5, indicating a +50% MPM in gain.
Step 2	$M(\omega)$ initial slope flatness test	From Figure 4.10, the slope can be seen as approximately flat, with the slope of the fitted line equal to 8.3093×10^{-16}. Therefore, no MPM in time constant is present.
Step 3	Optimal delay mismatch detection	The results for the optimal delay estimation is identical to that summarized in Table 4.1, and therefore no MPM in delay is present.

4.2.4.3   +50% Gain Mismatch

The diagnosis procedure, as described in Table 3.4, can be followed to diagnose the MPM for the +50% change in gain as seen in Table 4.4.
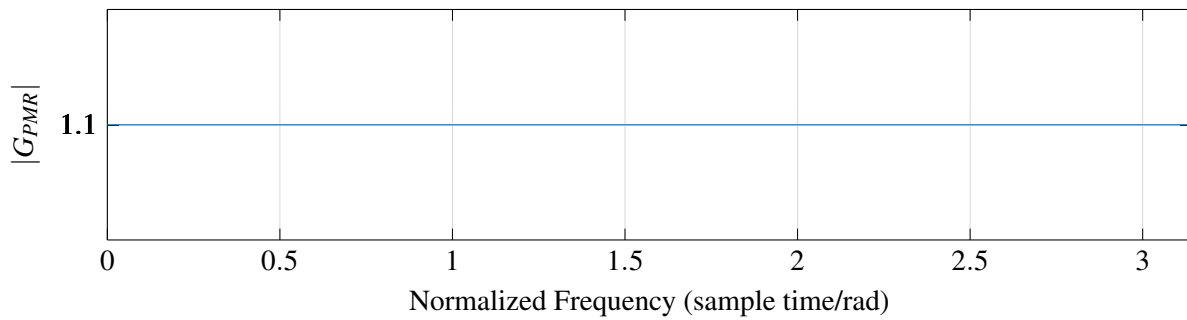

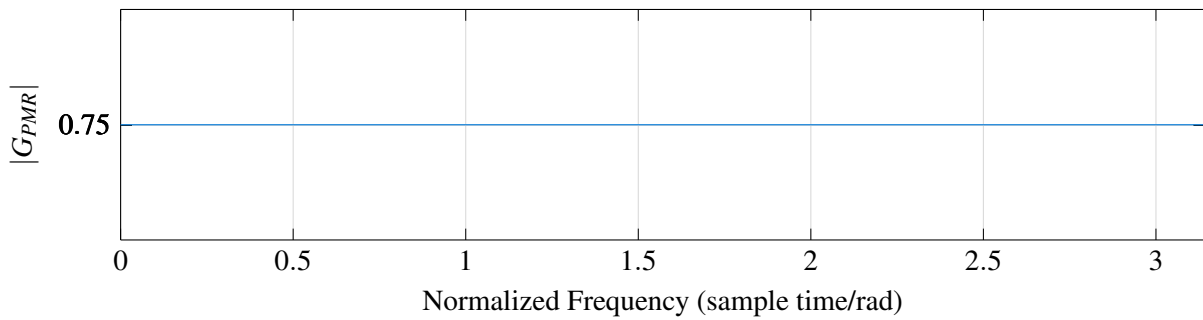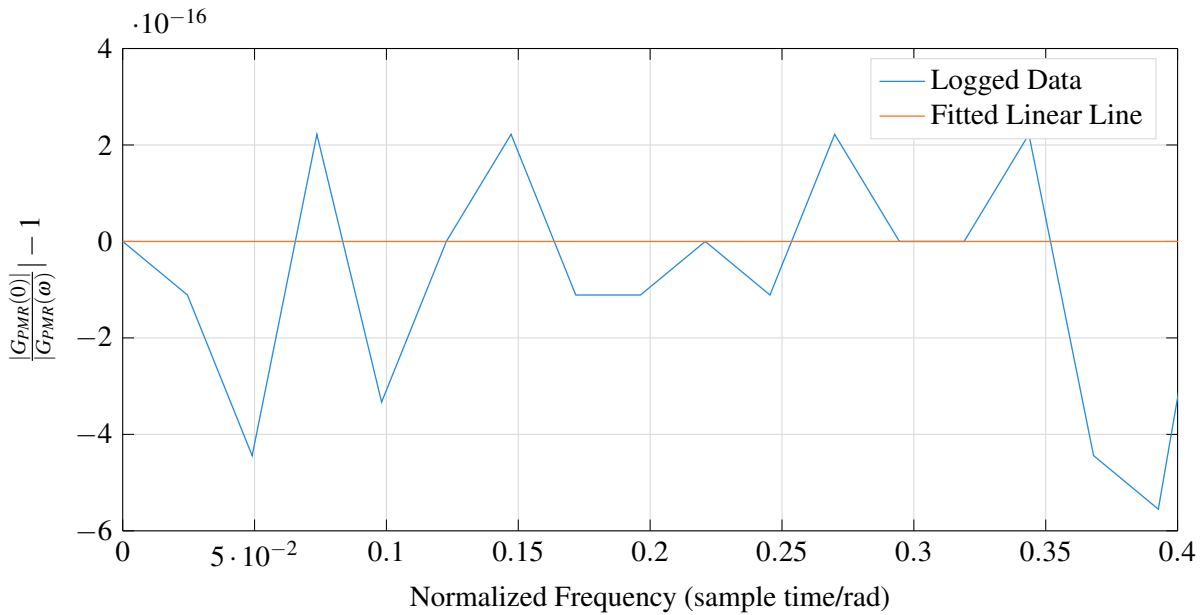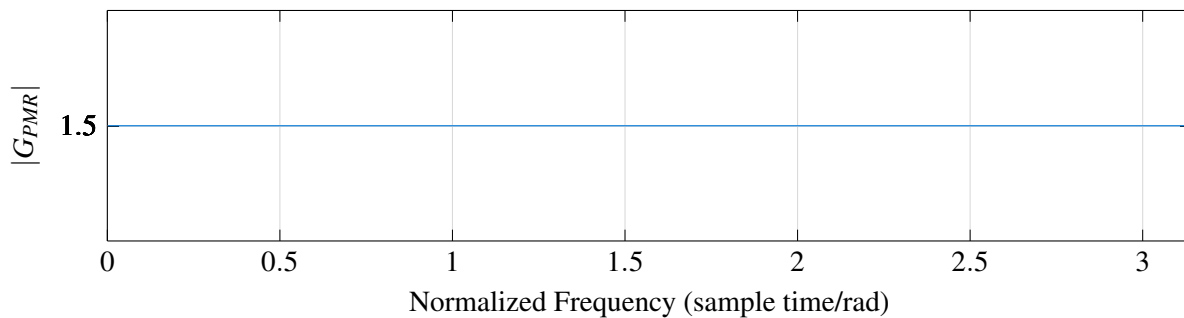**Figure 4.9.** PMR magnitude spectra for a +50% gain mismatch applied to a SISO system.
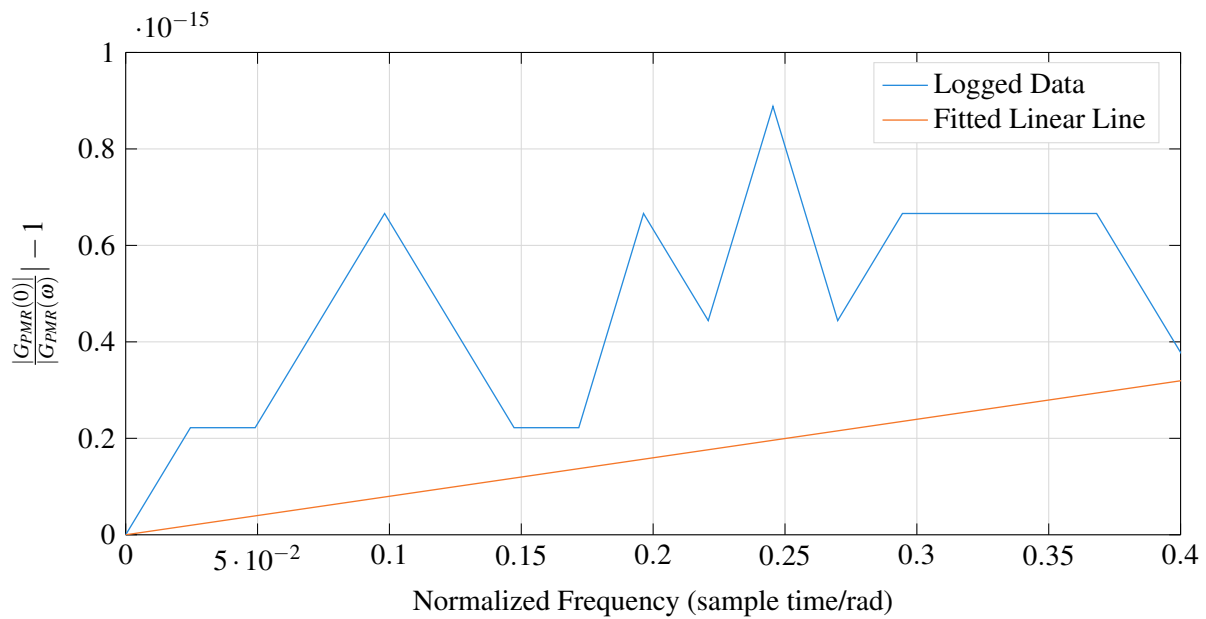
Figure 4.10. Initial slope of PMR magnitude spectra for a +50% gain mismatch applied to a SISO system.

4.2.5   Simulation of Time constant Mismatch

To evaluate and quantify the PMR for detecting MPM within the time constant parameter of the transfer function, the same simulation description and controller as described in Section 4.3.2 coupled with the SISO system described in Section 4.3.2, will be used along with the following mismatches introduced into the process:

1. A time constant increase of 10%: $G(s) = \frac{1.01e^{-0.5s}}{20.262s+1}$
2. A time constant decrease of 25%: $G(s) = \frac{1.01e^{-0.5s}}{13.815+1}$

4.2.5.1   +10% Time Constant Mismatch

From Figure 4.11, the deduction can be made that there is no MPM in the gain term of the transfer function since the zero-frequency component of the PMR magnitude spectrum is very close to one. With an exact value of 1.0084 the graphical representation of the gain mismatch can be confirmed. Using an initial slope flatness test on the PMR magnitude spectrum, the relative degree and direction of MPM can be determined. The linear line fitted to the initial rate of change of the PMR magnitude spectra, in Figure 4.12, has a slope -0.03744, indicating a relative mismatch number of 3.744 for the time constant in the SISO transfer function. The relative mismatch number is calculated by multiplying the slope of the linear line fitted to the initial rate of change of the PMR magnitude spectra by -100. This is done to simplify the quantification of the relative MPM size while the sign change between the slope and the relative mismatch number is due to the fact that the time constant mismatch is

inversely proportional to the change of the magnitude spectrum as seen in (3.11), (3.18), Table 3.1, and Table 3.2. Therefore, the relative mismatch number approximates the relative amount of MPM present, when compared to other relative mismatch numbers, but does not correspond directly to the mismatch applied to the system, while the direction of the MPM is captured in the sign of the relative mismatch number. Finally, the optimization problem, as described in (3.45), is solved for a ΔD range of -5 to 5. As seen in Figure 4.13, the estimated MPM for the delay term is zero as the largest cost function is calculated for $\Delta D = 0$. This diagnosis can be summarized, as seen in Table 4.5, following the structure of Table 3.4.

Figure 4.11. PMR magnitude spectra for a +10% time constant mismatch applied to a SISO system.

Table 4.5. MPM diagnosis for +10% time constant mismatch.

	Assessment Procedure	Diagnosis of MPM
Step 1	$M(\omega)\|_{\omega=0}$	From Figure 4.11, the zero-frequency component of the magnitude spectra is 1.0084, indicating approximately 0% MPM in gain.
Step 2	$M(\omega)$ initial slope flatness test	From Figure 4.12, the slope can be seen as increasing, the slope of the fitted line equal to -0.0374, resulting in a relative mismatch number of 3.744 therefore capturing the correct mismatch direction.
Step 3	Optimal delay mismatch detection	The results for the optimal delay estimation can be seen in Figure 4.13. It is evident that there is no MPM detected in the delay term.
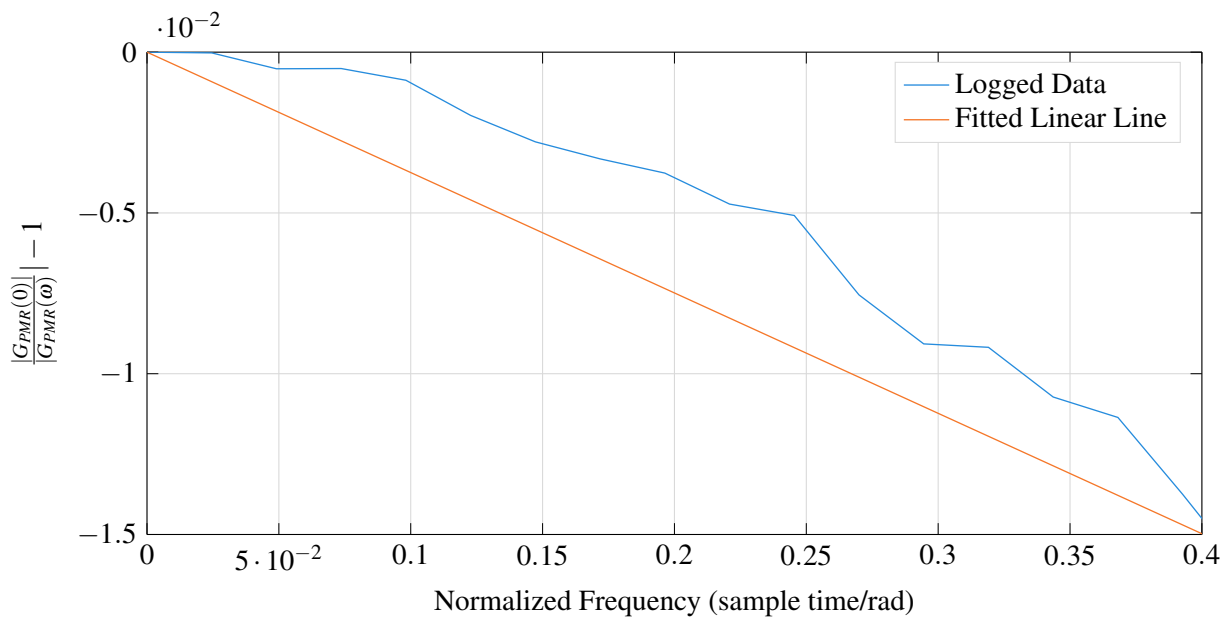
Figure 4.12. Initial slope of PMR magnitude spectra for a +10% time constant mismatch applied to a SISO system.
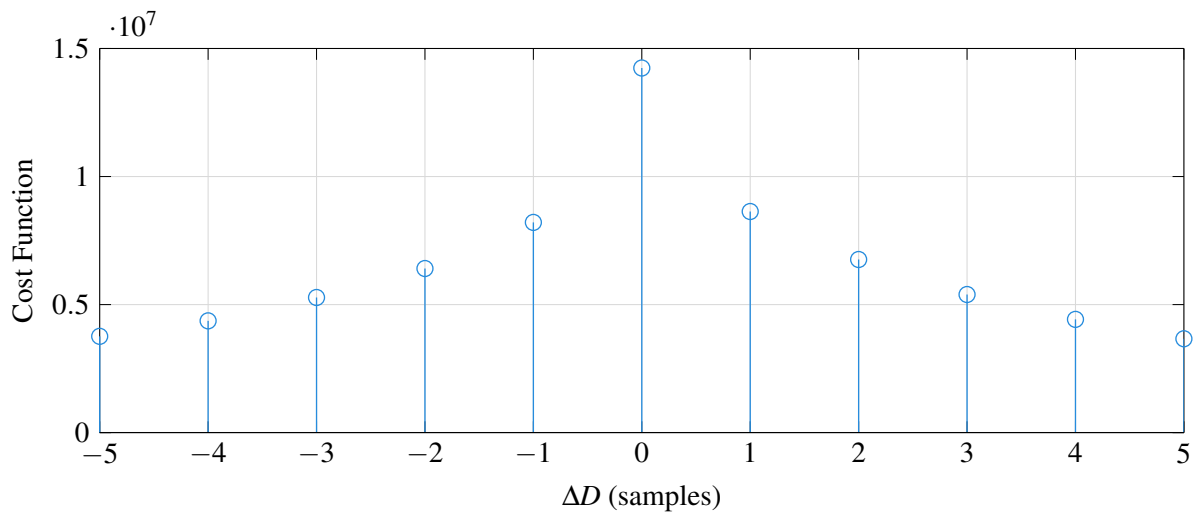
Figure 4.13. Objective function results for a +10% time constant mismatch applied to a SISO system.

4.2.5.2   -25% Time Constant Mismatch

The diagnosis procedure, as described in Table 3.4, can be followed to diagnose the MPM for the -25% change in time constant as seen in Table 4.6.

Table 4.6. MPM diagnosis for -25% time constant mismatch.

	Assessment Procedure	Diagnosis of MPM
Step 1	$M(\omega)\|_{\omega=0}$	From Figure 4.14, the zero-frequency component of the magnitude spectra is 1.0108, indicating approximately 0% MPM in gain.
Step 2	$M(\omega)$ initial slope flatness test	From Figure 4.15, the slope can be seen as increasing, the slope of the fitted line equal to 0.080918, resulting in a relative mismatch number of -8.0918 therefore capturing the correct relative size (compared to the +10% mismatch applied earlier) as well as the correct mismatch direction.
Step 3	Optimal delay mismatch detection	The results for the optimal delay estimation can be seen in Figure 4.16. It is evident that there is no MPM detected in the delay term.
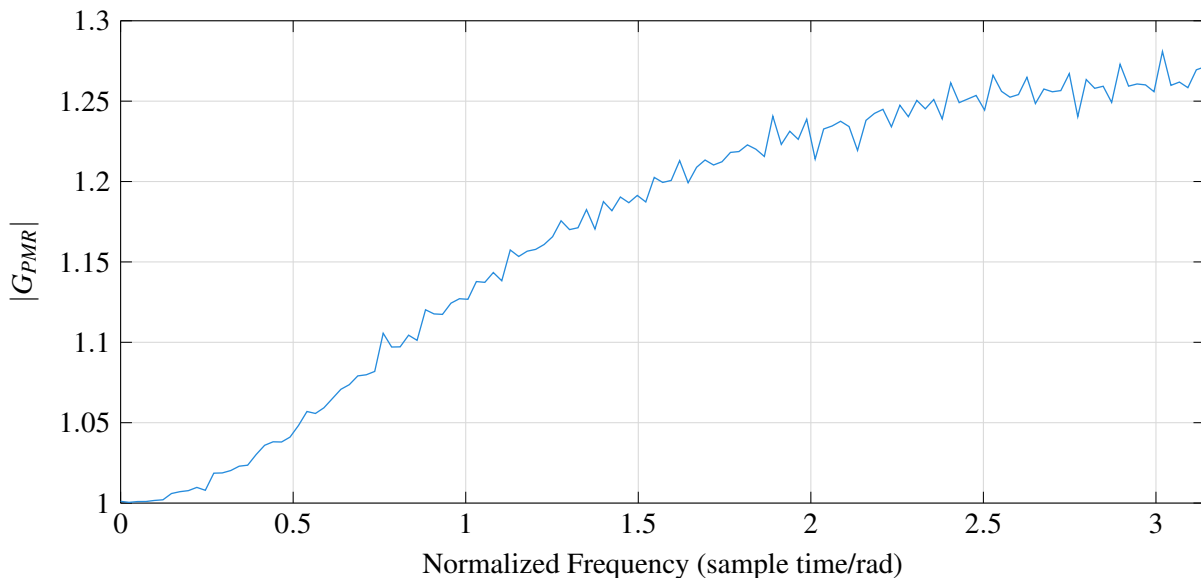
Figure 4.14. PMR magnitude spectra for a -25% time constant mismatch applied to a SISO system.
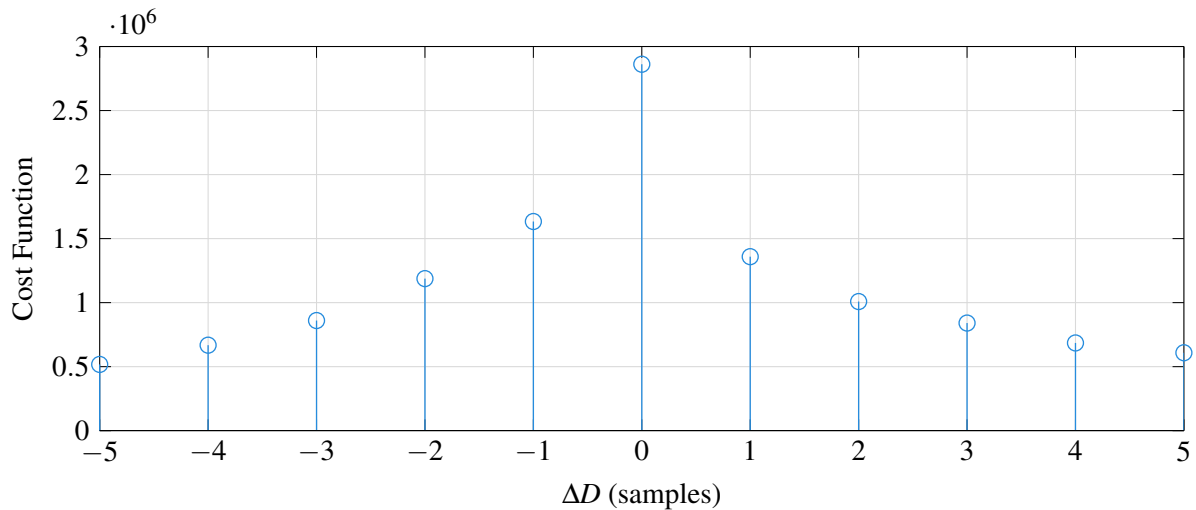
Figure 4.16. Objective function results for a -25% time constant mismatch applied to a SISO system.
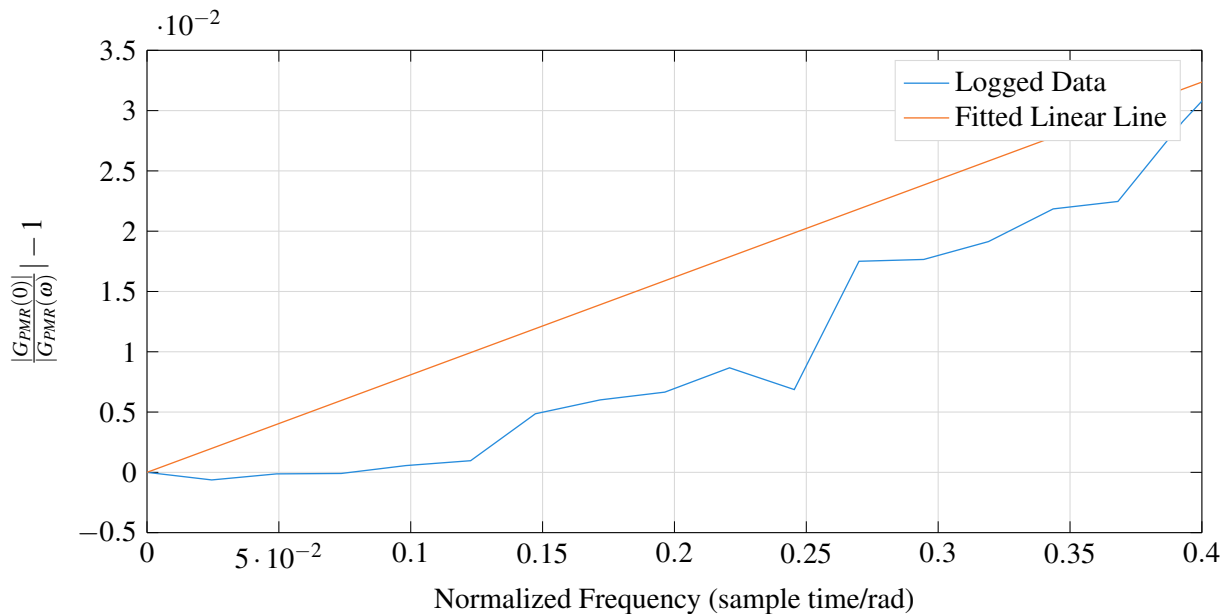
Figure 4.15. Initial slope of PMR magnitude spectra for a -25% time constant mismatch applied to a SISO system.

4.2.6 Simulation of Delay Mismatch

To determine the viability of detecting MPM in the delay term of a FOPTD transfer function using the PMR, the following mismatch in the delay term will be applied:

1. A delay increase of one sample (0.5 seconds): $G(s) = \frac{1.01e^{-1s}}{18.42+1}$

4.2.6.1   1 Sample Delay Mismatch

The same diagnosis procedure, as described in Table 3.4, and as followed above can be implemented to diagnose the MPM for the 1 sample delay mismatch applied to the system. From Figure 4.17, the zero-frequency component of the PMR magnitude spectra is 0.9972, indicating approximately 0% MPM in gain. From Figure 4.18, the slope can be seen as approximately flat, with the slope of the fitted line equal to 0.0011879, resulting in a relative mismatch number of -0.11879. Therefore, no MPM in time constant is present. The results for the optimal delay estimation can be seen in Figure 4.19. Since the maximum cost function is calculated for $\Delta D = 1$ a MPM of 1 sample is identified in the delay term of the process. This diagnosis can be summarized as seen in Table 4.7. It should be noted that if the delay mismatch present in the process does not align with a sampling instance, the optimal delay estimation technique would have a rounding effect and indicate the nearest integer, ΔD, to the mismatch present in the system.

Table 4.7. MPM diagnosis for 1 sample delay mismatch.

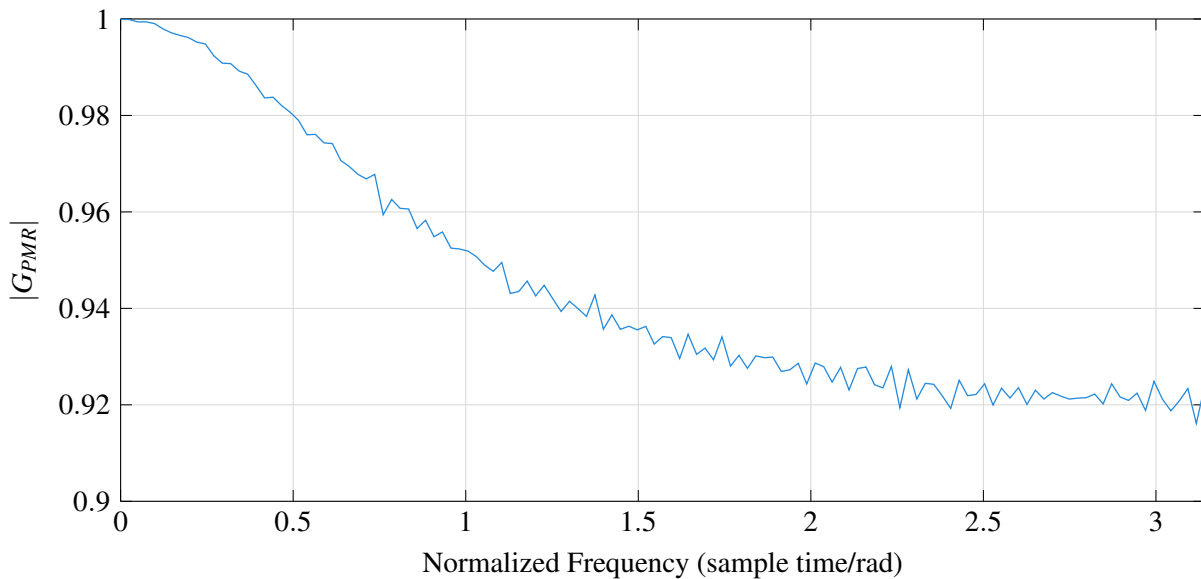|	**Assessment Procedure**	**Diagnosis of MPM**
Step 1	$M(\omega)\|_{\omega=0}$	From Figure 4.17, the zero-frequency component of the magnitude spectra is 0.997, indicating approximately 0% MPM in gain.
Step 2	$M(\omega)$ initial slope flatness test	From Figure 4.18, the slope can be seen as increasing, the slope of the fitted line equal to 0.0011879, resulting in a relative mismatch number of -0.11879 therefore capturing the correct relative size as well as the correct mismatch direction.
Step 3	Optimal delay mismatch detection	The results for the optimal delay estimation can be seen in Figure 4.19. It is evident that there is a delay mismatch of 1 sample.
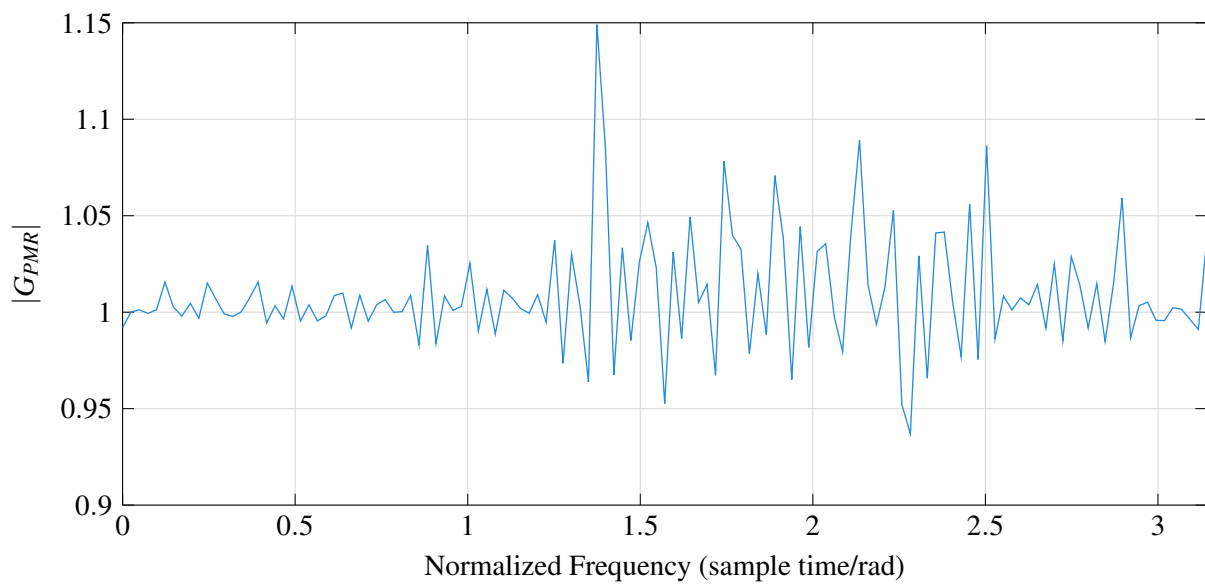
Figure 4.17. PMR magnitude spectra for a 1 sample time delay mismatch applied to a SISO system.
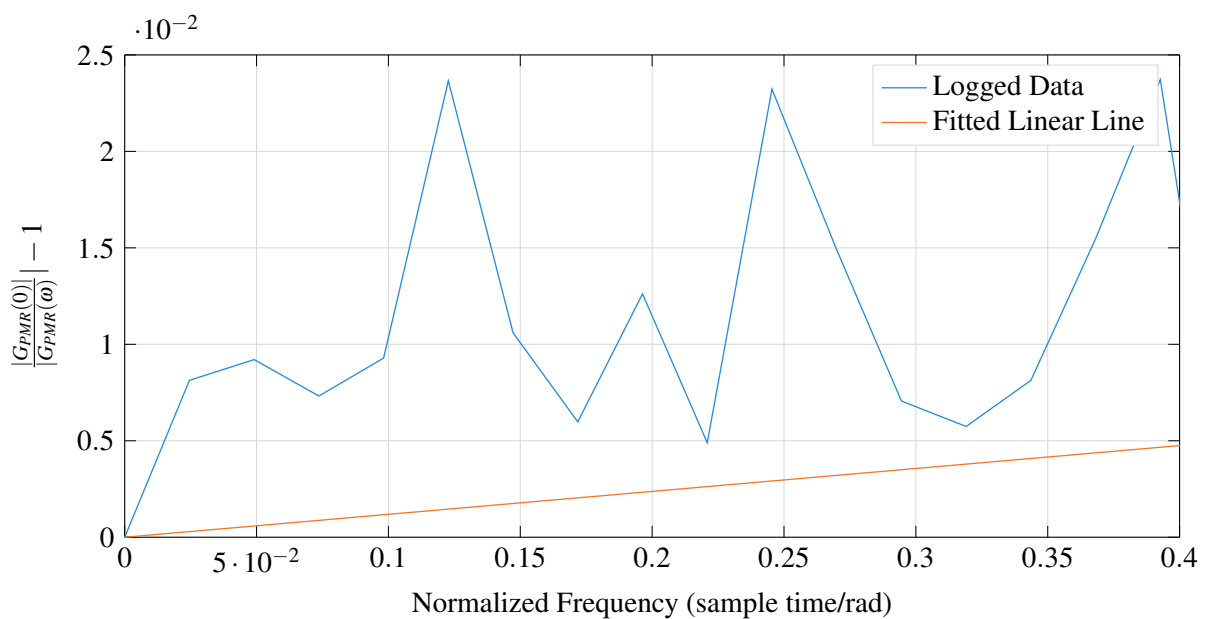
Figure 4.18. Initial slope of PMR magnitude spectra for a 1 sample time delay mismatch applied to a SISO system.
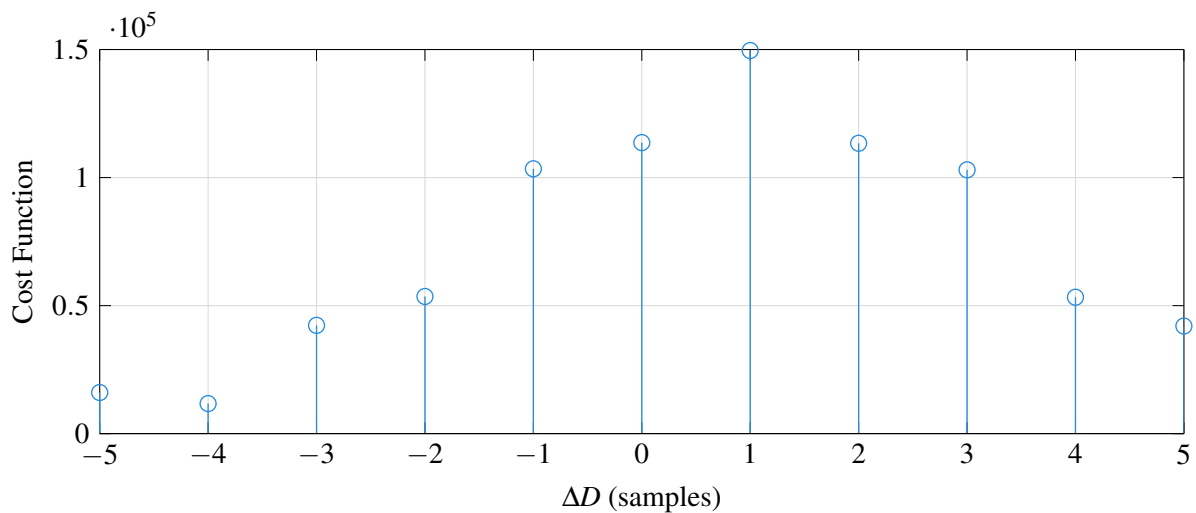
Figure 4.19. Objective function results for a 1 sample time delay mismatch applied to a SISO system.

4.2.7 Simulation of a Combination of Mismatches

The following scenarios will be used to validate the performance of the PMR methodology when concurrent mismatches are applied to the process.

1. **Scenario 1:** A gain increase of 20%, a time constant increase of 25%, and a delay increase of 1 sample (0.5 seconds): $G(s) = \frac{1.212e^{-1s}}{23.025+1}$

2. **Scenario 2:** A gain increase of 20%, a time constant decrease of 15%, and a delay decrease of 1 sample (0.5 seconds): $G(s) = \frac{1.212}{15.657+1}$
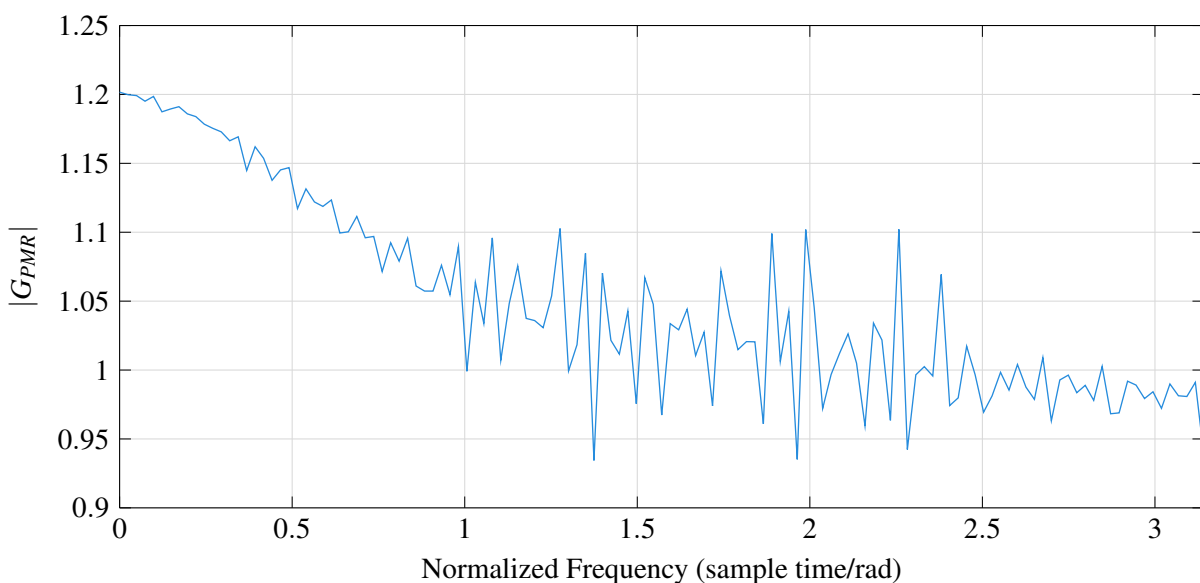
Figure 4.20. PMR magnitude spectra for the simulation study of scenario 1 applied to a SISO system.

4.2.7.1 Scenario 1

Using the diagnosis procedure as described in Table 3.4, the MPM for scenario 1 as applied to the system can be diagnosed as seen in Table 4.8.

Table 4.8. MPM diagnosis for scenario 1.

	Assessment Procedure	**Diagnosis of MPM**
Step 1	$M(\omega)\|_{\omega=0}$	From Figure 4.20, the zero-frequency component of the PMR magnitude spectra is 1.2016, indicating the correct MPM in the gain term of approximately +20% MPM.
Step 2	$M(\omega)$ initial slope flatness test	From Figure 4.21, the slope can be seen as decreasing, with the slope of the fitted line equal to -0.100575, resulting in a relative mismatch number of 10.056 and therefore diagnosing the correct mismatch direction and relative size (compared to Table 4.9) in the time constant term.
Step 3	Optimal delay mismatch detection	The results for the optimal delay estimation can be seen in Figure 4.22. Since the maximum cost function is calculated for $\Delta D = 1$, a MPM of 1 sample is identified in the delay term of the process.
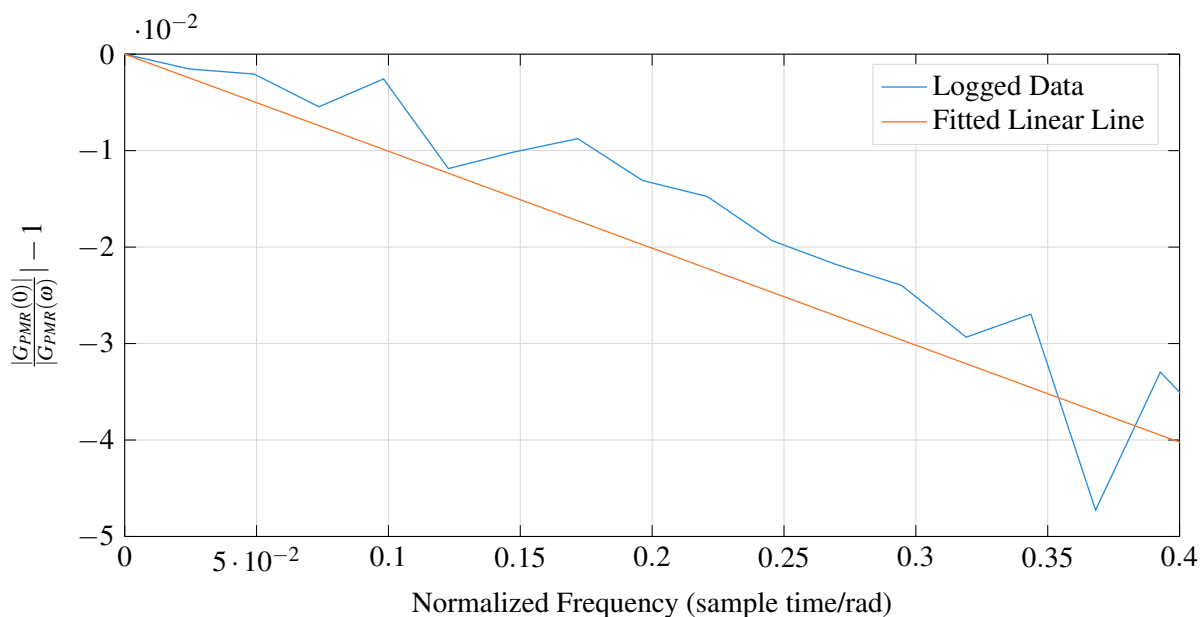
Figure 4.21. Initial slope of PMR magnitude spectra for the simulation study of scenario 1 applied to a SISO system.
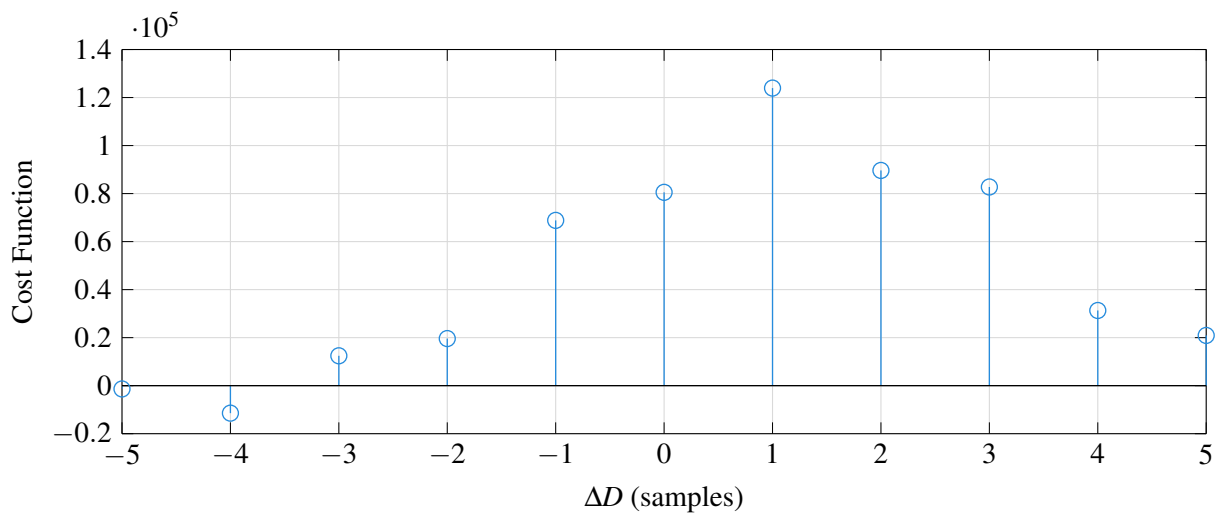
Figure 4.22. Objective function results for the simulation study of scenario 1 applied to a SISO system.

4.2.7.2   Scenario 2

Using the diagnosis procedure as described in Table 3.4, the MPM for scenario 2 as applied to the system can be diagnosed as seen in Table 4.9.

Table 4.9. MPM diagnosis for scenario 2.

	Assessment Procedure	**Diagnosis of MPM**
Step 1	$M(\omega)\|_{\omega=0}$	From Figure 4.23, the zero-frequency component of the PMR magnitude spectra is 1.2028, indicating the correct MPM in the gain term of approximately +20% MPM in gain.
Step 2	$M(\omega)$ initial slope flatness test	From Figure 4.24, the slope can be seen as increasing, with the slope of the fitted line equal to 0.0627912, resulting in a relative mismatch number of -6.2791 and therefore diagnosing the correct mismatch direction and relative size (compared to Table 4.8) in the time constant term.
Step 3	Optimal delay mismatch detection	The results for the optimal delay estimation can be seen in Figure 4.25. Since the maximum cost function is calculated for $\Delta D = -1$ a MPM of -1 sample is identified in the delay term of the process.
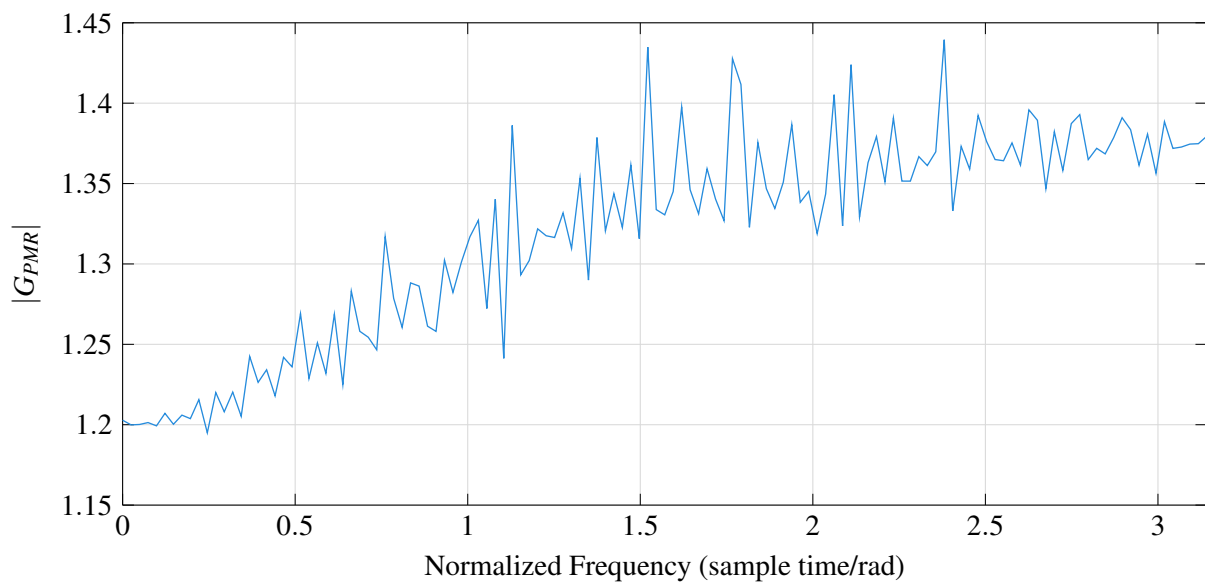
Figure 4.23. PMR magnitude spectra for the simulation study of scenario 2 applied to a SISO system.
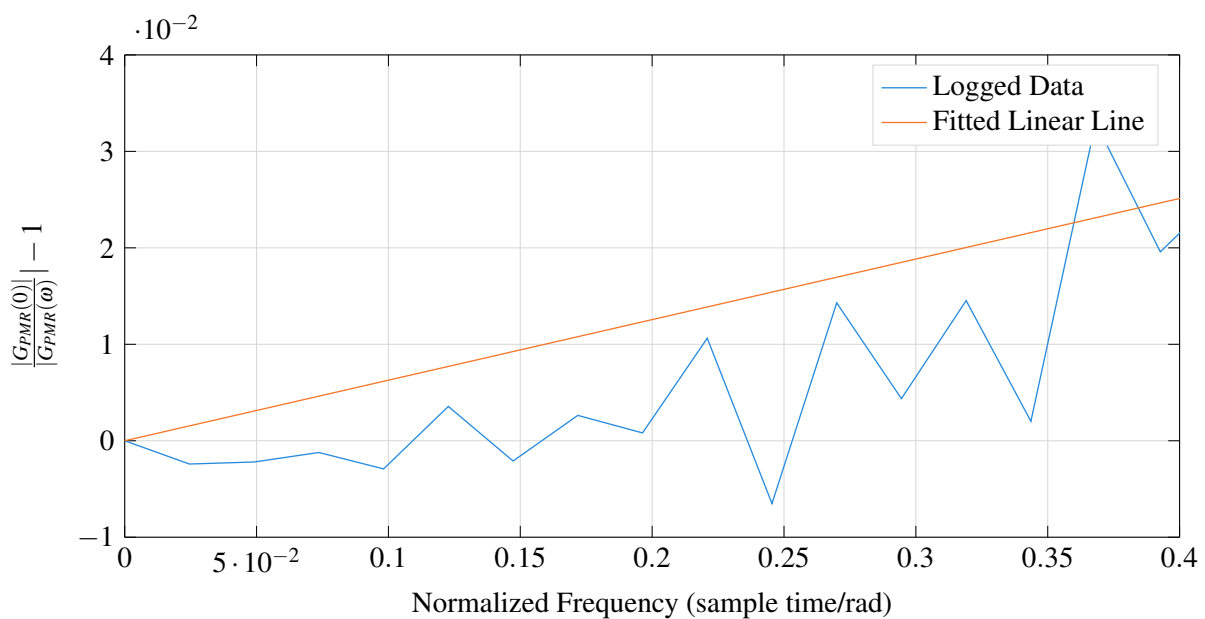
Figure 4.24. Initial slope of PMR magnitude spectra for the simulation study of scenario 2 applied to a SISO system.
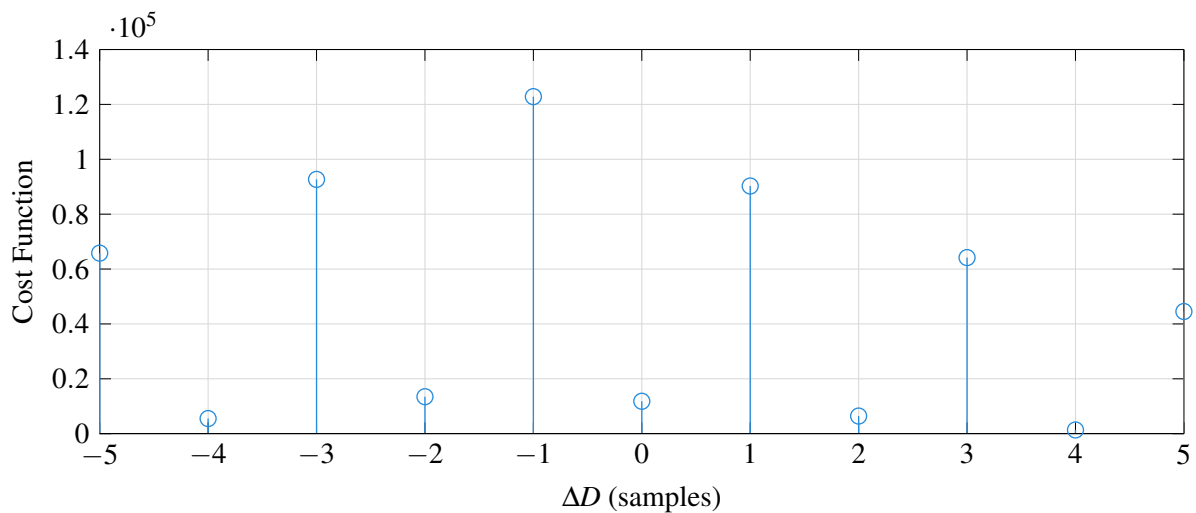
Figure 4.25. Objective function results for the simulation study of scenario 2 applied to a SISO system.

4.3 INVESTIGATION OF THE PMR FOR MIMO SYSTEMS

4.3.1 Process Description

To test and evaluate the PMR for MPM diagnosis in MIMO system, as developed in Section 3.4, the Wood-Berry distillation column, shown in Figure 4.26 and described in (4.7), will be used (Wood and Berry, 1973). The variables of (4.7), as discussed by (Wood and Berry, 1973), are listed in Table 4.10. The simulation structure and linear MPC controller, as described in Section 4.3.2, will be adapted to suit a MIMO system but will follow the same principles as the SISO case with regard to output disturbances and state estimation.
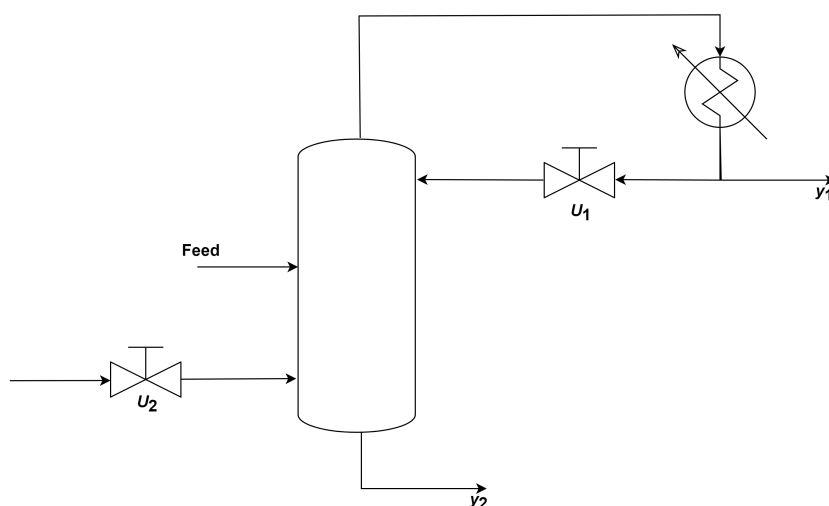
Figure 4.26. A simplified scheme of the Wood-Berry distillation column. Adapted from Zheng et al. (2009), with permission.

Table 4.10. Variable names for the Wood-Berry distillation column.

Variable	Name
MVs	
$u_1(s)$	Reflux flow rate
$u_2(s)$	Steam flow rate
CVs	
$y_1(s)$	Overhead product composition
$y_2(s)$	Bottom product composition

$$
\begin{bmatrix} y_1(s) \\ y_2(s) \end{bmatrix} = \begin{bmatrix} \frac{12.8e^{-s}}{16.7s+1} & \frac{-18.9e^{-3s}}{21s+1} \\ \frac{6.6e^{-7s}}{10.9s+1} & \frac{-19.4e^{-3s}}{14.4s+1} \end{bmatrix} \begin{bmatrix} u_1(s) \\ u_2(s) \end{bmatrix}.
\tag{4.7}
$$

4.3.2 Controller Design and Simulation Description

4.3.2.1 Controller Design

The plant of (4.7) will be controlled using a standard MPC controller. The controller is a linear constrained MPC controller (Qin and Badgwell, 2003) with an unconstrained Kalman-filter to estimate the states of the system from the plant outputs (Grewal and Andrews, 2001). Using a zero-order hold function with a sampling time of 1 second, the plant in (4.7) could be discretized:

$$
G(z) = \begin{bmatrix} \frac{0.744z^{-1}}{z-0.9419} & \frac{-0.8789z^{-3}}{z-0.9535} \\ \frac{0.5786z^{-7}}{z-0.9123} & \frac{-1.302z^{-3}}{z-0.9329} \end{bmatrix}.
\tag{4.8}
$$

A third-order Padé approximation of the time delay is used to realize the discrete state-space representation of (4.8) (Trefethen, 2019):

$$
x_{k+1} = Ax_k + Bu_k
\tag{4.9a}
$$

$$
y_k = Cx_k + Du_k
\tag{4.9b}
$$

with

$$A = \begin{bmatrix}
-2.06 & -0.479 & 0 & 0 & 0 & 0 & 0 & 0 & 0 & 0 \\
0.25 & 0 & 0 & 0 & 0 & 0 & 0 & 0 & 0 & 0 \\
0 & 0 & -1.258 & -0.4404 & -0.2446 & 0 & 0 & 0 & 0 & 0 \\
0 & 0 & 1 & 0 & 0 & 0 & 0 & 0 & 0 & 0 \\
0 & 0 & 0 & 0.125 & 0 & 0 & 0 & 0 & 0 & 0 \\
0 & 0 & 0 & 0 & 0 & -3.048 & -1.071 & -0.1905 & 0 & 0 \\
0 & 0 & 0 & 0 & 0 & 2 & 0 & 0 & 0 & 0 \\
0 & 0 & 0 & 0 & 0 & 0 & 0.25 & 0 & 0 & 0 \\
0 & 0 & 0 & 0 & 0 & 0 & 0 & 0 & -0.7361 & -0.1852 \\
0 & 0 & 0 & 0 & 0 & 0 & 0 & 0 & 0.25 & 0
\end{bmatrix}$$

$$B = \begin{bmatrix}
2 & 0 & 2 & 0 & 0 & 0 & 0 & 0 & 0 & 0 \\
0 & 0 & 0 & 0 & 0 & 2 & 0 & 0 & 2 & 0
\end{bmatrix}^T \tag{4.9d}$$

$$C = \begin{bmatrix}
-0.3832 & 3.066 & 0 & 0 & 0 & -0.45 & 0.675 & -1.8 & 0 & 0 \\
0 & 0 & 0.3028 & -0.3532 & 0.8073 & 0 & 0 & 0 & 0.6736 & -1.796
\end{bmatrix}$$

$$D = \begin{bmatrix} 0 & 0 \\ 0 & 0 \end{bmatrix}. \tag{4.9f}$$

Both the MPC and the Kalman-filter uses this state space description. The linear MPC, as in (4.4), is used. The prediction horizon (N_p) is chosen as 10 while the control horizon (N_c) is chosen as 2. The objective function weights are $Q = \text{diag}[1,1]$ and $R = \text{diag}[0.1,0.1]$ respectively. The Kalman-filter is designed using a constant Kalman gain, described in (4.5). The plant is controlled to the extent that no constraints are reached.

4.3.2.2 Simulation Description

The simulation of the plant uses the simulation structure seen in Figure 4.2. Both the plant and model outputs are logged for use with the PMR algorithm along with the setpoint.

To ensure that the required excitation is applied to the process, a pseudo-random binary sequence is used as a setpoint reference. AWGN signals, with a power-to-noise ratio of 0.1, are added to the plant output to simulate output disturbances.

4.3.3 Scenario 1

For the first scenario, the mismatches applied to the system can be seen in (4.10). This scenario will focus on the decoupling of a gain mismatch within the same row (first row) as well as the decoupling of

time constant mismatches in opposite directions within the same row (row 2). The results of the PMR applied to the acquired process data from the simulation study can be seen in Figure 4.27, Figure 4.28 and Figure 4.29.

$$\Delta\frac{K}{\hat{K}} = \begin{bmatrix} -23\% & 0\% \\ -17\% & -17\% \end{bmatrix} \tag{4.10a}$$

$$\Delta\frac{\tau}{\hat{\tau}} = \begin{bmatrix} 0\% & 0\% \\ -9\% & 10\% \end{bmatrix} \tag{4.10b}$$

$$\Delta\frac{D}{\hat{D}} = \begin{bmatrix} 0 \text{ samples} & 0 \text{ samples} \\ 0 \text{ samples} & 0 \text{ samples} \end{bmatrix}. \tag{4.10c}$$

Step 1 - Gain Mismatch

Following the diagnosis procedure in Table 3.4, the first step is to test the zero-frequency component of the PMR. In Figure 4.27, the individual decoupled PMR magnitude spectra of each entry in the PMR matrix can be seen. The following zero-frequency components are observed:

$$|\boldsymbol{G}_{PMR}(0)| = \begin{bmatrix} 0.7700 & 1.0000 \\ 0.8464 & 0.8311 \end{bmatrix}. \tag{4.11}$$

From these values, the diagnosed MPM in the gain term can be calculated as:

$$\text{Gain MPM} = \left(|\boldsymbol{G}_{PMR}(0)| - 1_{(2\times2)} \right) \times 100$$

$$= \left(\begin{bmatrix} 0.7700 & 1.0000 \\ 0.8464 & 0.8311 \end{bmatrix} - 1_{(2\times2)} \right) \times 100$$

$$= \begin{bmatrix} -0.2300 & 0 \\ -0.1536 & -0.1689 \end{bmatrix} \times 100 \tag{4.12}$$

$$= \begin{bmatrix} -23\% & 0\% \\ -15.3641\% & -16.885\% \end{bmatrix}.$$

Step 2 - Time Constant Mismatch

Step 2 in Table 3.4 allows for the estimation of time constant mismatches within the process, by investigating the initial slope of the PMR magnitude spectra. The initial magnitude spectra slope of each entry in the PMR matrix can be seen in Figure 4.28. As in Section 4.2, a linear line is fitted to the magnitude spectra rate of change and the slope of the linear line is used to diagnose the MPM. The

Figure 4.27. PMR magnitude spectra for the simulation study of scenario 1 applied to the Wood-Berry distillation column.

slopes of the linear lines in Figure 4.28 are:

$$\widehat{\alpha}_{\boldsymbol{G}_{PMR}} = \begin{bmatrix} 0 & 0 \\ 0.1803 & -0.2074 \end{bmatrix}. \tag{4.13}$$

Therefore, realizing the following relative mismatch numbers:

$$\text{Time Constant MPM} = \widehat{\alpha}_{\boldsymbol{G}_{PMR}} \times -100$$

$$= \begin{bmatrix} 0 & 0 \\ 0.1803 & -0.2074 \end{bmatrix} \times -100 \tag{4.14}$$

$$= \begin{bmatrix} 0 & 0 \\ -18.0251 & 20.7434 \end{bmatrix}.$$

Figure 4.28. Initial slope of PMR magnitude spectra for the simulation study of scenario 1 applied to the Wood-Berry distillation column.
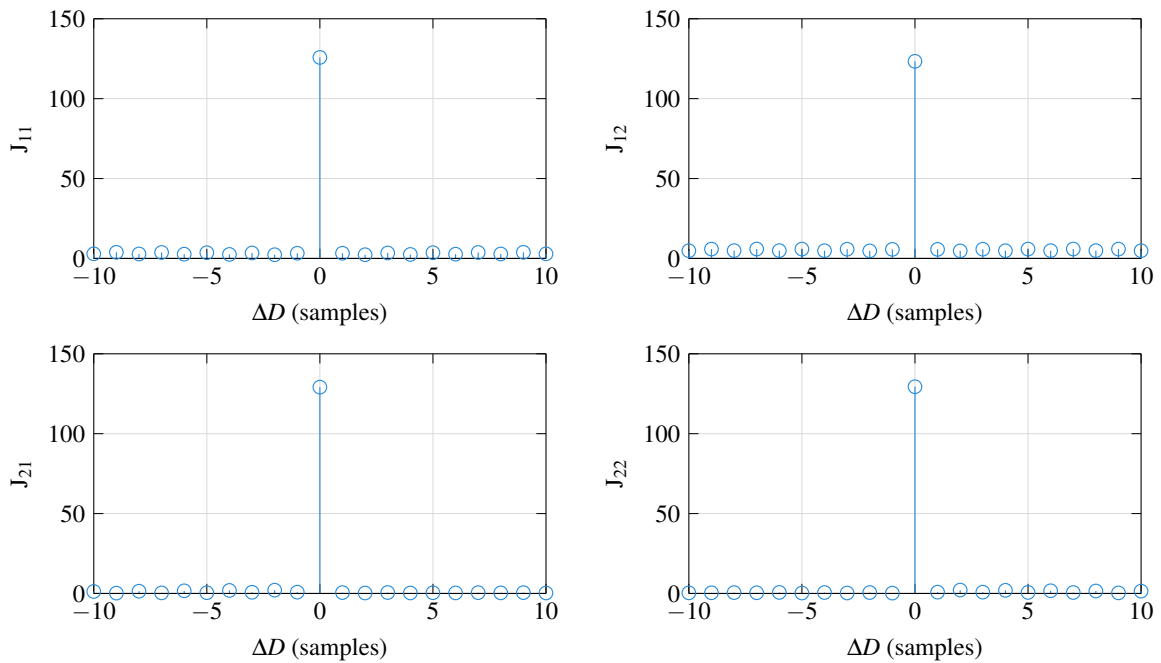
Figure 4.29. Objective function results for the simulation study of scenario 1 applied to the Wood-Berry distillation column.

Step 3 - Delay Mismatch

The last step in Table 3.4 is to use the optimal delay estimation technique to determine the delay mismatches present in the process. The cost function results for each entry in the PMR matrix can be seen in Figure 4.29. From these graphs the MPM for the delay terms are:

$$\text{Delay MPM} = \begin{bmatrix} 0 \text{ samples} & 0 \text{ samples} \\ 0 \text{ samples} & 0 \text{ samples} \end{bmatrix}. \tag{4.15}$$

For the first test scenario the results in (4.12), (4.14) and (4.15) correlates to the applied mismatches in (4.10a), (4.10b) and (4.10c).

4.3.4 Scenario 2

The second scenario applied to the Wood-Berry distillation column will focus on gain mismatch diagnosis for mismatches in opposite directions (second row of (4.16a)) as well as the diagnosis of delay mismatches. As mentioned by Wood and Berry (1973) and Yerramilli and Tangirala (2016) the Wood-Berry distillation column becomes unstable for delays introduced into transfer functions other than G_{21}, a two-sample delay will be added to G_{21} as seen in (4.16c).

$$\Delta\frac{K}{\hat{K}} = \begin{bmatrix} -28\% & 0\% \\ -17\% & 18\% \end{bmatrix} \tag{4.16a}$$

$$\Delta\frac{\tau}{\hat{\tau}} = \begin{bmatrix} 0\% & 0\% \\ -9\% & 10\% \end{bmatrix} \tag{4.16b}$$

$$\Delta\frac{D}{\hat{D}} = \begin{bmatrix} 0 \text{ samples} & 0 \text{ samples} \\ 2 \text{ samples} & 0 \text{ samples} \end{bmatrix}. \tag{4.16c}$$

Step 1 - Gain Mismatch

Once again, the MPM in the gain term of all transfer functions in the transfer function matrix can be determined using the zero-frequency term of the PMR magnitude spectra as seen in Figure 4.30.

$$\begin{aligned} \text{Gain MPM} &= \left(|\boldsymbol{G}_{PMR}(0)| - 1_{(2\times2)} \right) \times 100 \\ &= \left(\begin{bmatrix} 0.7200 & 1.0000 \\ 0.8351 & 1.1774 \end{bmatrix} - 1_{(2\times2)} \right) \times 100 \\ &= \begin{bmatrix} -28.0000\% & 0\% \\ -16.4852\% & 17.7429\% \end{bmatrix}. \end{aligned} \tag{4.17}$$
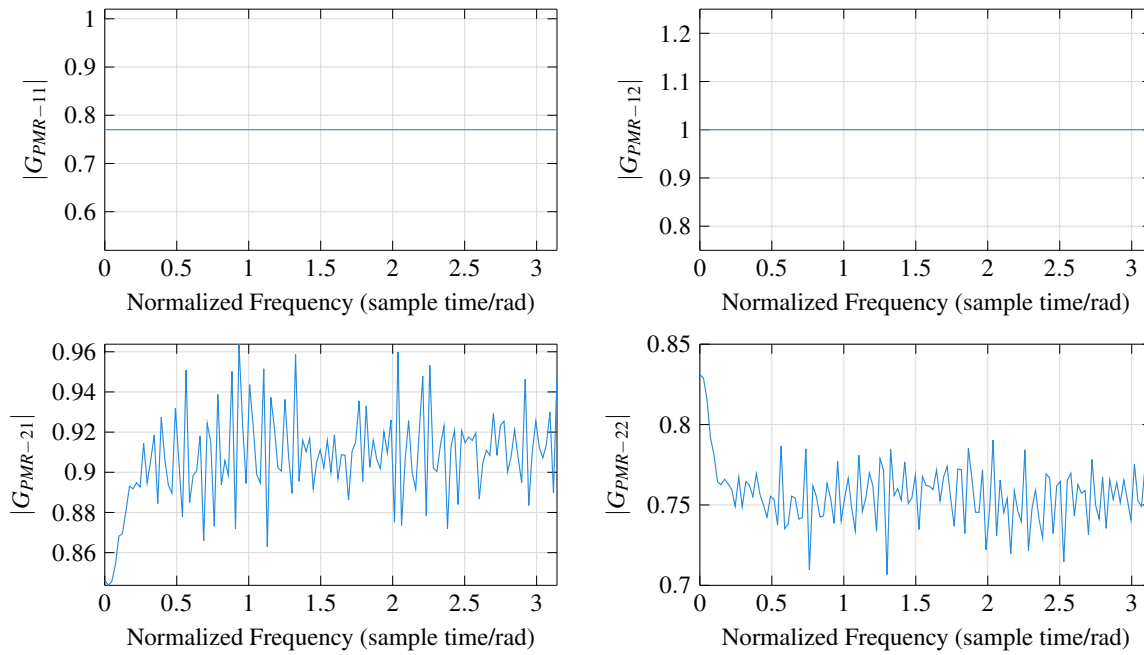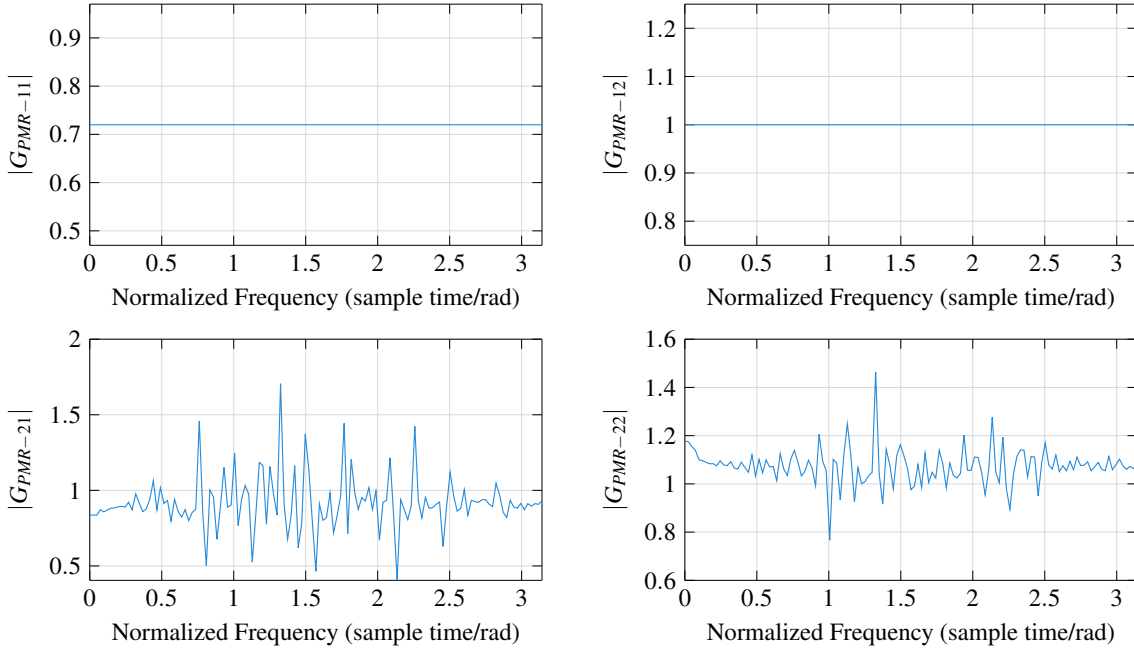
Figure 4.30. PMR magnitude spectra for the simulation study of scenario 2 applied to the Wood-Berry distillation column.

Step 2 - Time Constant Mismatch

The relative time constant mismatches can be deduced from the linear fitted line (orange line) to the initial slope of the PMR magnitude spectrum as seen in Figure 4.31.

$$
\text{Time Constant MPM} = \widehat{\alpha}_{\boldsymbol{G}_{PMR}} \times -100
$$

$$
= \begin{bmatrix} 0 & 0 \\ 0.1923 & -0.2275 \end{bmatrix} \times -100 \tag{4.18}
$$

$$
= \begin{bmatrix} 0 & 0 \\ -19.2261 & 22.7496 \end{bmatrix}.
$$

Step 3 - Delay Mismatch

Finally, the time delay mismatch can be estimated using the optimal delay estimation technique, described in Section 3.3.1.

$$
\text{Delay MPM} = \begin{bmatrix} 0 \text{ samples} & 0 \text{ samples} \\ 2 \text{ samples} & 0 \text{ samples} \end{bmatrix}. \tag{4.19}
$$

Once again, the results in (4.17), (4.18) and (4.19) correlates closely to the applied MPM as described in (4.16a), (4.16b) and (4.16c).
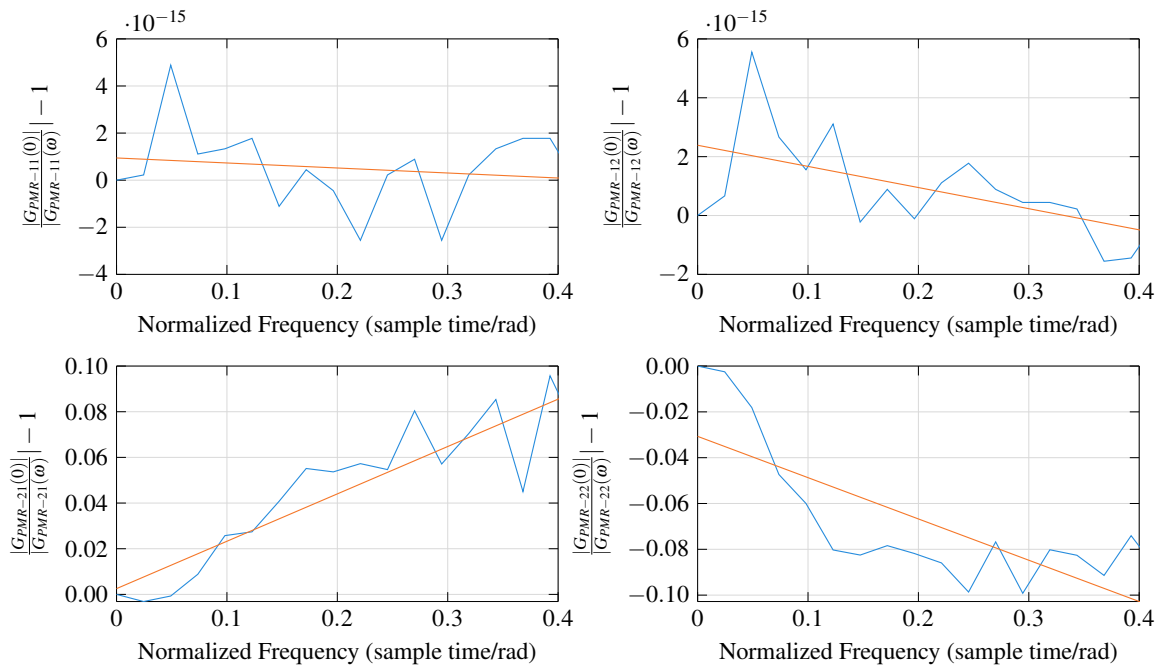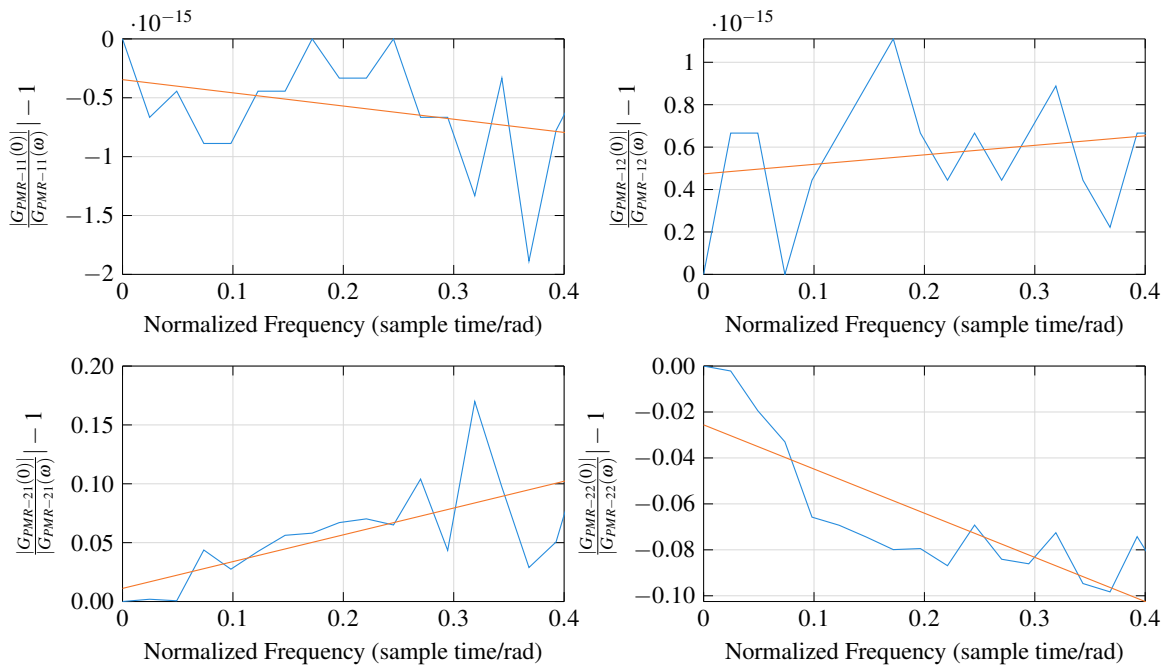
Figure 4.31. Initial slope of PMR magnitude spectra for the simulation study of scenario 2 applied to the Wood-Berry distillation column.

4.3.5   Results Summary

It should be noted that for both scenario 1 and scenario 2, the MPM diagnosis does not match the MPM applied to the system exactly, but rather the diagnosis provides an accurate approximation of the MPM present in the process. This can be attributed to two reasons. First is the fact that the PMR is estimated using data logged from the process outputs containing output disturbances which can slightly affect the accuracy of the PMR estimation. Nonetheless, these effects should largely be removed by correlating all process outputs with the relevant setpoints as described in (3.54) and (3.55). The second attributing factor is the correlation between all outputs and all inputs in a MIMO system. Using (3.55) to decouple all input channels from all output channels does not realize a unique solution. The linear algebra approach to the decoupling of the MIMO system and the construction of the PMR from operational data (containing a contribution of all inputs) will realize a suboptimal PMR estimation. This will lead to slightly inaccurate MPM parameter diagnoses as in (4.12) and (4.17).

The large difference in the relative mismatch number for time constants and the actual MPM applied for the time constants can be attributed to the PMR diagnosis procedure where the time constant mismatches are diagnosed over a range of frequencies, the suboptimal nature of the PMR estimation coupled with the effects of output disturbances will lead to an imprecise diagnosis over the bandwidth B.
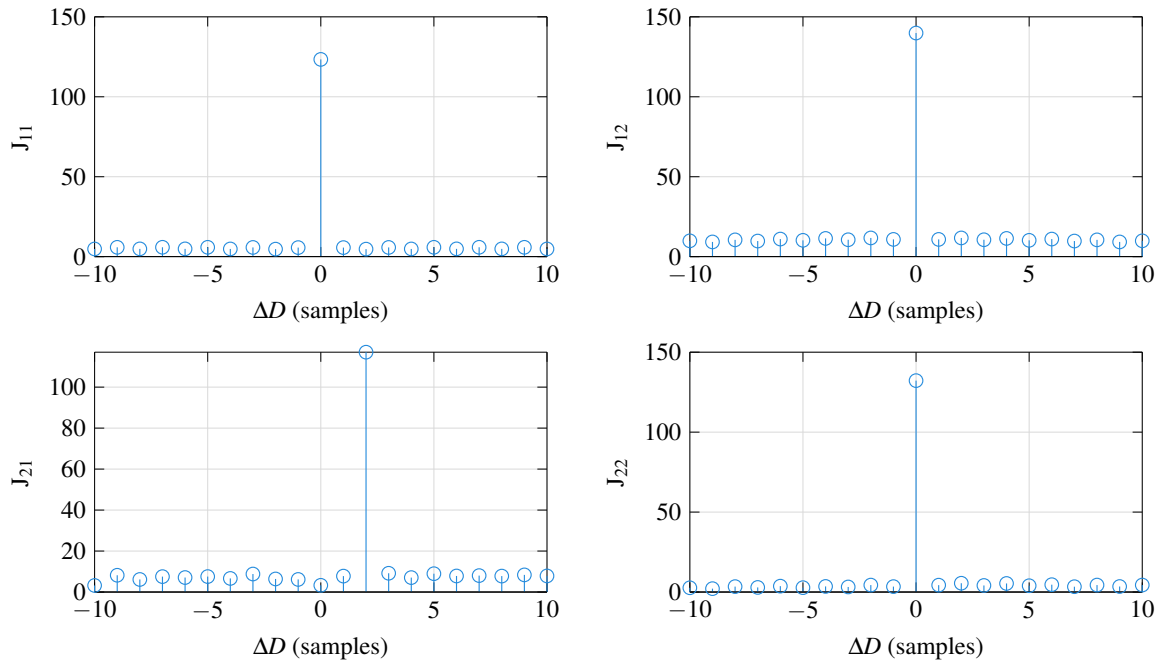
Figure 4.32. Objective function results for the simulation study of scenario 2 applied to the Wood-Berry distillation column.

Nonetheless, the relative mismatch number calculated for time constant parameters will still diagnose the correct direction of the mismatch, as well as provide an estimate of the relative size of mismatches when comparing different relative mismatch numbers to one another.

4.4   CHAPTER SUMMARY

Various scenarios of MPM were applied to two separate plants. A pressure control system was used to test the SISO case of the PMR. Each parameter of the FOPTD transfer function, namely gain, time constant and delay, containing MPM was accurately diagnosed with a relative size estimate of the mismatch as well as the direction of the mismatch.

Following the pressure control system, the Wood-Berry distillation column, a widely used benchmark MIMO system, was used to evaluate the MIMO PMR. The MIMO PMR was able to decouple all the process outputs and estimate the PMR matrix allowing for an accurate diagnosis of all FOPTD parameters for all entries in the transfer function matrix. The diagnosis once again allowed insight into the relative size and direction of each MPM.

CHAPTER 5 PLANT MODEL RATIO APPLIED TO A GRINDING MILL CIRCUIT

5.1 CHAPTER OVERVIEW

The following chapter focuses on the application of the PMR to a grinding mill circuit. A complete non-linear model of the grinding mill circuit is presented in Section 5.2. This non-linear model will form the basis of the application of the PMR. Since the PMR is based on FOPTD transfer functions and the plant will be controlled using a linear MPC, SID is applied to the non-linear model as described in Section 5.3. An initial test on the grinding mill is done by repeating the MIMO PMR simulations of Section 4.3. These results are recorded in Section 5.4. After the linear simulations have been conducted, some shortcoming of the PMR as applied to the grinding mill circuit is presented in Section 5.5.

5.2 PROCESS MODEL

The semi-autogenous grinding mill in Figure 5.1 receives the mined ore to be milled (u_{MFO}), along with water, steel balls, and the underflow of the hydrocyclone to form the mill load (y_{J_T}). The mill turns causing the falling balls to crush the ore and mix the broken ore with the water in the mill to form a slurry. An end-discharge grate is placed at the outflow of the mill to ensure only the slurry is fed into the sump which acts as a buffer. The sump level (y_{SLEV}) is controlled by adding water (u_{SFW}) to the sump. The slurry is then pumped from the sump to the hydrocyclone classifier with a controlled feed flow rate (u_{CFF}). The in-specification particles will then exit as the cyclone overflows (y_{PSE}) and the out-of-specification particles are fed back into the mill.

The mill is modelled as in Ziolkowski (2022), using an adapted version of the continuous-time phenomenological non-linear population balance model of Le Roux et al. (2020) and Le Roux and Steyn (2022). The developed model provides a wide variety of suitable operating conditions, viable

to test the model-plant mismatch diagnosis. The following nomenclature is used throughout the development of the model:

- *Rocks* refer to all the ore that requires further grinding before being able to fit through the end-discharge grate.

- *Solids* refer to all of the ore that is small enough to discharge through the end-discharge grate.

- *Fines* refer to the portion of ore smaller than the specification size.

- *Coarse* is the portion of ore larger than the specification size. Therefore solids can be regarded as a combination of fine ore and coarse ore.

Table 5.1 provides the convention of lower-case subscripts for model flow-rates ($Q(\mathrm{m}^3/\mathrm{h})$) and model states ($x(\mathrm{m}^3)$). The first subscript differentiates between the circuit units namely the mill, the sump and the cyclone. The second subscript differentiates between the model states namely rocks, solids coarse, fines, balls or water. The third subscript (used for flow-rates) differentiates between the inflow, underflow and outflow. All model parameters used in the development of the full state space model are described in Table 5.2.
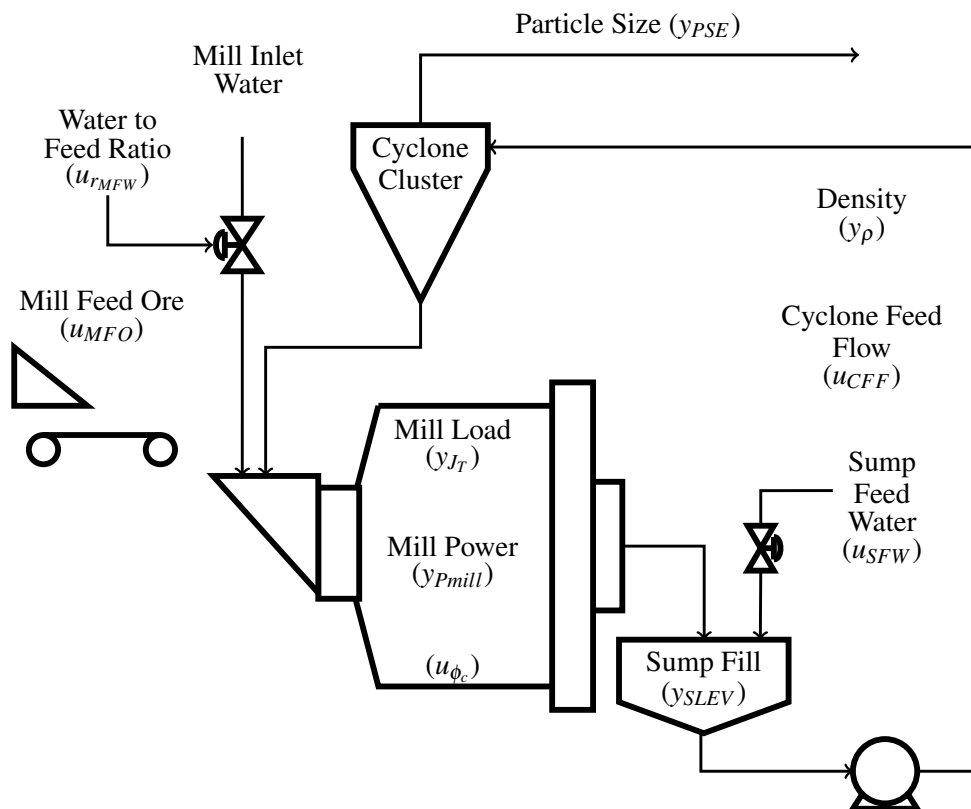
Figure 5.1. Single-stage closed-loop semi-autogenous grinding mill circuit.

Table 5.1. Description of state and flow-rate lower case subscripts (Le Roux and Steyn, 2022).

Subscript	Description
$x_{\square-}$	m-mill; s-sump; c-cyclone
$x_{-\square}$	w-water; s-solids; c-coarse; f-fines; r-rocks; b-balls
$Q_{--\square}$	i-inflow; o-outflow; u-underflow

5.2.1   Mill Model

The total volume of the mill is comprised of four states: water (x_{mw}), solids (x_{ms}), rocks (x_{mr}), and fines (x_{mf}) all with the same unit of cubic meters (m^3). Therefore, the dynamics of the semi-autogenous grinding mill can be modelled as a population volume balance. The difference in feed-rate of particles into the mill, coupled with the discharge rate of particles from the mill, constitutes the accumulation of components within the mill:

$$\frac{d}{dt}x_{mw} = -Q_{mwo} + Q_{mwi} = -\left(\varphi d_q x_{mw}\left(\frac{x_{mw}}{x_{ms}+x_{mw}}\right)\right) + u_{MFW} \tag{5.1a}$$

$$\frac{d}{dt}x_{ms} = -Q_{mso} + Q_{msi} + Q_{RC} = -\left(\varphi d_q x_{mw}\left(\frac{x_{ms}}{x_{ms}+x_{mw}}\right)\right) + \frac{u_{MFO}}{\rho_o}(1-\alpha_r) + Q_{RC} \tag{5.1b}$$

$$\frac{d}{dt}x_{mr} = -Q_{RC} + Q_{mri} = -Q_{RC} + \frac{u_{MFO}}{\rho_o}(\alpha_f) \tag{5.1c}$$

$$\frac{d}{dt}x_{mfo} = -Q_{mf} + Q_{mfi} + Q_{FP} = -\left(\varphi d_q x_{mw}\left(\frac{x_{mf}}{x_{ms}+x_{mw}}\right)\right) + \frac{u_{MFO}}{\rho_o}(\alpha_r) + Q_{FP}, \tag{5.1d}$$

where the mill feed flow-rates of water, solids, rocks and fines are respectively represented by Q_{mwi}, Q_{msi}, Q_{mri}, and Q_{mfi} (m^3/h) while the mill discharge of water, solids and fines respectively are represented as Q_{mwo}, Q_{mso}, Q_{mfo} (m^3/h). The volumetric rate of rocks broken into solids, i.e., the rock consumption rate, is Q_{RC} (m^3/h). The volumetric rate of ore broken into fines is represented by Q_{FP} (m^3/h). Using the assumption of a constant feed-rate for balls, they are not included in the model dynamics. α_f and α_r denotes the ratio of fines and rocks within u_{MFO} respectively and ρ_o (m^3/h) is the ore density. The parameter d_q (1/h) represents the pressure or driving force applied to the slurry to discharge from the mill while the rheology factor, φ, is an empirically defined function. A large aperture discharge grate, fitted to the end of the mill, is used as a discharge prevention mechanism for large ore, rocks and steel balls. The fine production and rock consumption terms of (5.1) are:

$$Q_{FP} = \frac{P_m}{\rho_o K_{FP}(y_{J_T}, \phi_m)} \tag{5.2a}$$

$$Q_{RC} = \frac{P_m}{\rho_o K_{RC}(y_{J_T}, \phi_m)}, \tag{5.2b}$$

Table 5.2. Model parameters (Le Roux and Steyn, 2022).

Parameter	Parameter values	Unit	Description
Densities			
ρ_o	2.7	t/m^3	Density of ore
ρ_w	1	t/m^3	Density of water
Mill parameters			
α_f	0.0802	-	Mass fraction of fines in the feed ore
α_r	0.5	-	Mass fraction of rocks in the feed ore
δ_s	0.928	-	Power parameter for fraction solids in the mill
δ_v	0.928	-	Power parameter for volume of mill filled
d_q	36.4	h^{-1}	Discharge rate
ε_o	0.6	-	Maximum fraction of solids by volume slurry at zero slurry flow
φ_N	0.5092	-	Rheology normalisation factor
$J_{TP_{max}}$	0.48	-	Fraction of mill filled at maximum power draw
K_{FP}	18.8943	MWh/t	Fines production factor
K_{RC}	21.5333	MWh/t	Rock consumption factor
P_{max}	4.0369×10^3	MW	Maximum mill power draw
v_{mill}	208	m^3	Mill volume
Sump parameters			
v_{sump}	5	m^3	Sump volume
Cyclone parameters			
α_{su}	0.2343	-	Parameter related to fraction solids in cyclone underflow
C_1	0.6	-	Cyclone model constants
C_2	0.7	-	Cyclone model constants
C_3	2	-	Cyclone model constants
ε_c	427.6986	m^3/h	Parameter related to coarse split at cyclone

where $K_{FP}(y_{J_T}, \phi_m)$ and $K_{RC}(y_{J_T}, \phi_m)$ are functions describing the energy required (per tonne) to produce the fines and consume the rocks respectively:

$$
\begin{aligned}
K_{FP}(y_{J_T}, \phi_m) = [&(-3.73\phi_m^3 + 0.602\phi_m^2 + 0.301\phi_m - 0.0487)y_{J_T}^3 \\
&+ (8.76\phi_m^3 - 1.97\phi_m^2 - 0.453\phi_m + 0.0877)y_{J_T}^2 \\
&+ (-6.82\phi_m^3 + 1.91\phi_m^2 + 0.180\phi_m - 0.0501)y_{J_T} \\
&+ (1.77\phi_m^3 - 0.581\phi_m^2 - 0.00728\phi_m + 0.00882)] \times 10^6
\end{aligned}
\tag{5.3a}
$$

$$
\begin{aligned}
K_{RC}(y_{J_T}, \phi_m) = [&(-0.4078\phi_m^3 - 3.06\phi_m^2 + 1.55\phi_m - 0.183)y_{J_T}^3 \\
&+ (2.68\phi_m^3 + 5.13\phi_m^2 - 2.92\phi_m + 0.355)y_{J_T}^2 \\
&+ (-3.15\phi_m^3 - 2.61\phi_m^2 + 1.78\phi_m - 0.226)y_{J_T} \\
&+ (1.05\phi_m^3 + 0.361\phi_m^2 - 0.352\phi_m + 0.0472)] \times 10^6.
\end{aligned}
\tag{5.3b}
$$

The fraction of the mill filled with charge, y_{J_T}, is defined as:

$$
y_{J_T} = \frac{x_{mw} + x_{ms} + x_{mr} + x_{mb}}{v_{mill}},
\tag{5.4}
$$

where the internal volume of the mill is represented by v_{mill} (m^3) and x_{mb} (t/h) is the balls within the mill. The mill power draw, from (5.2), is modelled as a function of ϕ_m and y_{J_T}:

$$
P_m(y_{J_T}, \phi_m) = P_{max}(\phi_m)\left(1 - \delta_v\left(\frac{y_{J_T}}{J_{T,P_{max}}} - 1\right)^2 - \delta_s\left(\frac{\varphi}{\varphi_N} - 1\right)^2\right),
\tag{5.5}
$$

where δ_s and δ_v are the power change parameters for the fraction of slurry volume filled with solids and the volume of the mill respectively. φ_N is a normalization factor while the maximum power draw is given by:

$$
P_{max}(\phi_m) = \left(-2.7\phi_{,}^2 + 3.92\phi_m - 1.02\right) \times 10^4,
\tag{5.6}
$$

incorporating the effects of the fluidity and density of the slurry on the performance of the mill, the empirical rheology factor is:

$$
\varphi = \begin{cases}
\sqrt{1 - \left(\varepsilon_0^{-1} - 1\right)\frac{x_{ms}}{x_{mw}}}; & \frac{x_{ms}}{x_{mw}} \leq \left(\varepsilon_0^{-1} - 1\right)^{-1} \\
0; & \frac{x_{ms}}{x_{mw}} > \left(\varepsilon_0^{-1} - 1\right)^{-1}.
\end{cases}
\tag{5.7}
$$

The slurry will be only water when $\alpha = 1$ and $\frac{x_{ms}}{x_{mw}} = 0$ while the slurry will be a non-flowing mud when $\alpha = 0$ and $\frac{x_{ms}}{x_{mw}} = 1.5$. $\varepsilon_o = 0.6$ is the approximate maximum fraction of solids by volume of slurry at zero slurry flow (Song et al., 2008).

5.2.2 Sump Model

As depicted in Figure 5.1, the sump receives the discharged slurry from the mill. The sump then acts as a buffer before the slurry is pumped to the classifier. To prevent any spillage, the sump volume (y_{SVOL}) should not exceed the total sump volume, simultaneously the sump should not run dry. Even though the addition of water (u_{SFW}) to the sump dilutes the slurry pumped to the classifier, u_{SFW} along with the manipulation of the feed-rate to the classifier is used to control y_{SVOL}. Under the assumption that all water, solids and fines within the sump are perfectly mixed, along with the discharge grate ensuring that no steel balls (x_{mb}) or rocks (x_{ms}) are present, the population volume of the sump, which is a mixture of water (x_{sw}), solids (x_{ss}) and fines (x_{sf}), can be described in state space as:

$$\frac{d}{dt}x_{sw} = Q_{swi} - Q_{swo} = Q_{mwo} + u_{SFW} - \left(u_{CFF}\left(\frac{x_{sw}}{x_{sw} + x_{ss}} \right) \right) \tag{5.8a}$$

$$\frac{d}{dt}x_{ss} = Q_{ssi} - Q_{sso} = Q_{mso} - \left(u_{CFF}\left(\frac{x_{ss}}{x_{sw} + x_{ss}} \right) \right) \tag{5.8b}$$

$$\frac{d}{dt}x_{sf} = Q_{sfi} - Q_{sfo} = Q_{mfo} - \left(u_{CFF}\left(\frac{x_{sf}}{x_{sw} + x_{ss}} \right) \right), \tag{5.8c}$$

where the sump feed flow-rates of water, solids and fines are described by Q_{swi}, Q_{ssi}, Q_{sfi} (m^3/h) respectively while the sump discharge flow-rates of water, solids and fines are described by Q_{swo}, Q_{sso}, Q_{sfo} (m^3/h) respectively. A variable speed pump is used to pump the sump discharge to the cyclone. The percentage of the sump filled with slurry is defined as:

$$y_{SLEV} = 100\left(\frac{x_{ss} + x_{sw}}{v_{sump}} \right), \tag{5.9}$$

while the sump outflow density is:

$$y_\rho = \frac{\rho_w x_{sw} + \rho_o x_{ss}}{x_{ss} + x_{sw}}, \tag{5.10}$$

where the physical volume of the sump is v_{sump} (m^3) and ρ_w (t/m^3) is the density of water.

5.2.3 Hydrocyclone Classification Model

A model for the classifier of the grinding mill is required to calculate the total water, solids, and fines that split at the classifier. As described by Botha et al. (2018), the classifier of the system can be modelled as either a single hydrocyclone, or a cluster of cyclones. For this study, the classifier will be modelled as a single cyclone (Le Roux et al., 2013). Using the effect of the angular velocity of the particles inside the cyclone, taking into account the slurry density and viscosity, the non-linear static cyclone models, the product size and density, the underflow of coarse material is modelled as:

$$Q_{ccu} = (Q_{sso} - Q_{sfo})\left(1 - C_1 exp\left(\frac{-u_{CFF}}{\varepsilon_c} \right) \right)\left(1 - \left(\frac{F_i}{C_2} \right)^{C_3} \right)\left(1 - P_i^{C_3} \right), \tag{5.11}$$

where the fraction of solids in the cyclone feed is $F_i = \frac{Q_{sso}}{u_{CFF}}$. The fraction of fines in the feed solids is $P_i = \frac{Q_{sfo}}{Q_{sso}}$. The coarse split is related by ε_c (m^3/h).

The relation of solids within the underflow can be expressed as:

$$F_u = \frac{Q_{csu}}{Q_{csu} + Q_{cwu}}. \tag{5.12}$$

To determine the amount of fines, water, and coarse underflow, the model can be adjusted to:

$$F_u = C_2 - (C_2 - F_i) \exp\left(-\frac{Q_{ccu}}{\alpha_{su}\varepsilon_c}\right). \tag{5.13}$$

Under the assumption that fines are not influenced by centrifugal forces, the ratio of fines to water in the feed and underflow respectively can be regarded as approximately equal ($\frac{Q_{sfo}}{Q_{swo}} \approx \frac{Q_{cfu}}{Q_{cwu}}$). Therefore, from (5.12) the cyclone underflow flow-rates in (5.1) can be expressed as:

$$Q_{cwu} = \frac{Q_{swo}(Q_{ccu} - F_u Q_{ccu})}{F_u Q_{swo} + F_u Q_{sfo} - Q_{sfo}} \tag{5.14a}$$

$$Q_{cfu} = \frac{Q_{sfo}(Q_{ccu} - F_u Q_{ccu})}{F_u Q_{swo} + F_u Q_{sfo} - Q_{sfo}} \tag{5.14b}$$

$$Q_{csu} = Q_{ccu} + Q_{cfu}. \tag{5.14c}$$

Using a flow balance around the cyclone, the water overflow (Q_{cwo}), solids overflow (Q_{cso}) and fines overflow (Q_{cfo}) can be determined. The product particle size passing the specification size (y_{PSE}) is defined as:

$$y_{PSE} = 100\left(\frac{Q_{cfo}}{Q_{cso}}\right). \tag{5.15}$$

5.2.4 State Space Representation

The standard state-space model representation is:

$$\frac{d}{dt}\mathbf{x} = \mathbf{f}(t, \mathbf{x}, \mathbf{u}, \mathbf{p})$$
$$\mathbf{y} = \mathbf{h}(t, \mathbf{x}, \mathbf{u}, \mathbf{p}). \tag{5.16}$$

For the grinding mill circuit, the states are $\mathbf{x} = [x_{mw}, x_{ms}, x_{mr}, x_{mf}, x_{sw}, x_{ss}, x_{sf}]^T$, while the inputs are $\mathbf{u} = [u_{MFO}, u_{SFW}, u_{CFF}]^T$ and the outputs are $\mathbf{y} = [y_{J_T}, y_{SLEV}, y_{PSE}]^T$. $\mathbf{p}$ contains the model parameters as listed in Table 5.2, the function $\mathbf{f}(\cdot)$ is given by (5.1) and (5.8) while the function $\mathbf{h}(\cdot)$ is given by (5.4), (5.5), (5.9), (5.10), and (5.15).

5.3 SYSTEM IDENTIFICATION

5.3.1 Linear Model Fitting

The non-linear grinding mill circuit described in Section 5.2 is used as the plant. A linear model of the plant is obtained using standard SID procedures as described by Ljung (1999). It is well known that FOPTD models can be used to successfully describe and control many industrial processes (Larsen et al., 2007; Li et al., 2008; Rasmussen and Larsen, 2009) and therefore the models fitted to the process will be FOPTD transfer functions as shown in (1.1).

The three MVs that will be excited in the SID procedure are:

- Cyclone Feed Flow (u_{CFF})
- Mill Feed Ore (u_{MFO})
- Sump Feed Water (u_{SFW})

The three CVs that will be measured in the SID procedure are:

- Particle Size (y_{PSE})
- Mill Load (y_{Load})
- Sump Fill (y_{SLEV})

For each of the MVs, the same input sequence is used to capture as much of the process dynamics as possible while keeping the other MVs constant. All three SID procedures can be seen in Figure 5.2, Figure 5.3 and Figure 5.4 where the blue line signifies the non-linear plant response and the orange line the FOPTD model fitted to the response. For the SID as well as all other simulations, the mill feed water ($u_{r_{MFW}}$) is controlled as a ratio of the mill feed ore (u_{MFO}). From Figure 5.2, Figure 5.3 and Figure 5.4 the transfer function matrix of FOPTD transfer functions is:

$$
\begin{bmatrix} y_{PSE} \\ y_{J_T} \\ y_{SLEV} \end{bmatrix} = \begin{bmatrix} \frac{-9.892\times10^{-5}}{0.4924s+1}e^{-0.0444s} & \frac{-5.208\times10^{-4}}{0.187s+1} & \frac{1.927\times10^{-4}}{0.04758s+1} \\ \frac{4.302\times10^{-4}}{0.3173s+1} & \frac{2.774\times10^{-4}}{s}e^{-0.0472s} & \frac{-3.131\times10^{-4}}{0.2355s+1}e^{-0.0528s} \\ \frac{-45.35}{53.07s+1} & \frac{13.07}{8.277s+1}e^{-0.025s} & \frac{91.99}{93.68s+1} \end{bmatrix} \begin{bmatrix} u_{CFF} \\ u_{MFO} \\ u_{SFW} \end{bmatrix}. \quad (5.17)
$$

50% of the data was used to fit the models while the remaining 50% of the data was used to validate the models. The accuracy of each transfer function in (5.17) is calculated using a root mean squared error between the non-linear plant response and the FOPTD response:

$$
\text{FOPTD accuracy} = \begin{bmatrix} 27.91\% & 32.89\% & 87.54\% \\ 88.95\% & 1.50\% & 89.02\% \\ 85.16\% & 86.79\% & 91.13\% \end{bmatrix}. \quad (5.18)
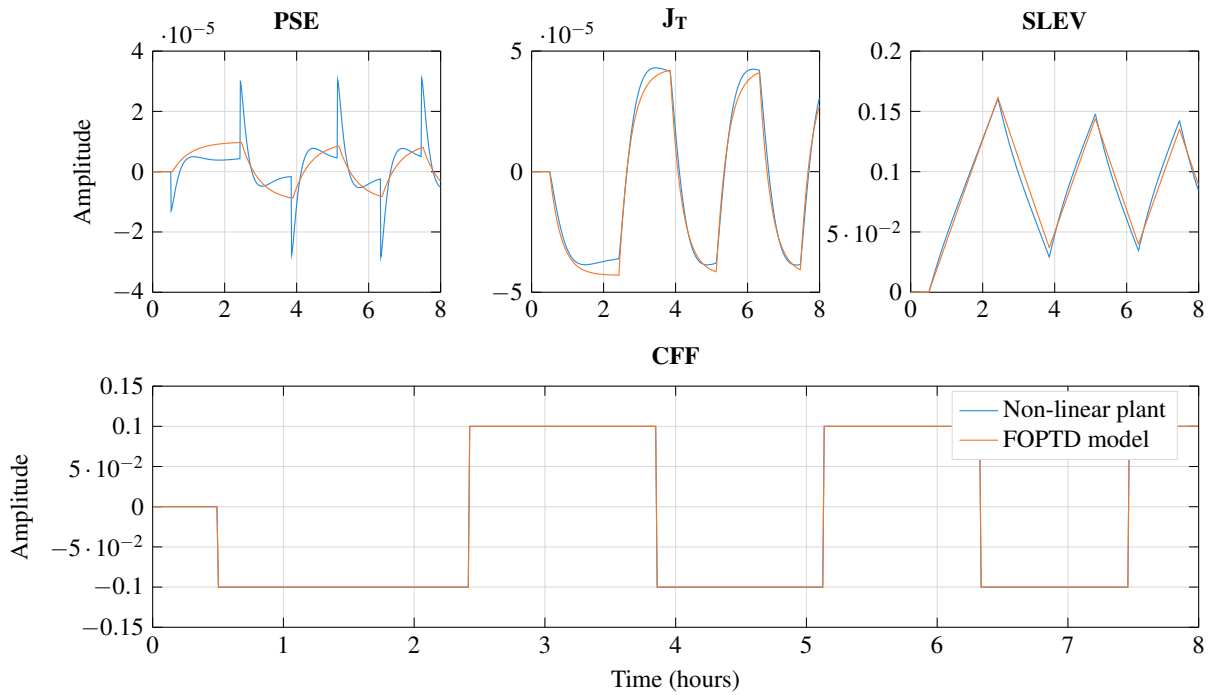$$

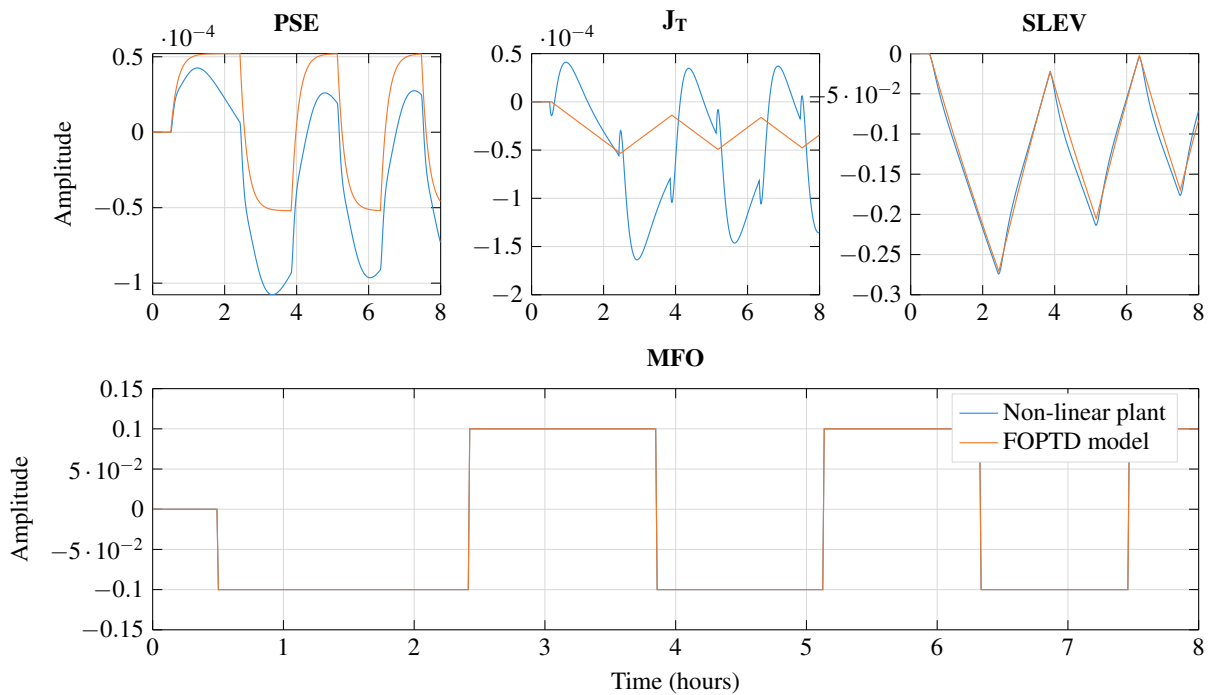**Figure 5.2.** SID applied to the grinding mill for excitation in u_{CFF}.

Figure 5.3. SID applied to the grinding mill for excitation in u_{MFO}.
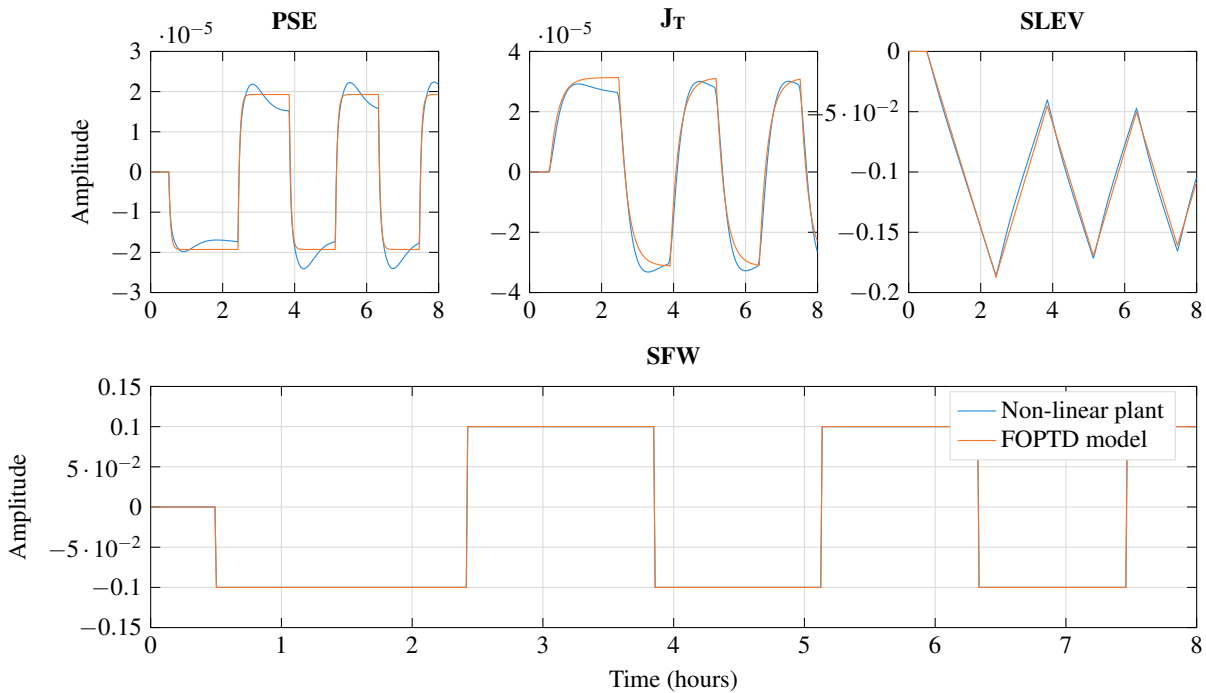
Figure 5.4. SID applied to the grinding mill for excitation in u_{SFW}.

5.3.2 Linear Model Scaling

As shown in (3.55), each individual model output is used to decouple the process outputs from the PMR matrix. Therefore, attention should be given to the relative size difference in gain terms of each transfer function within the transfer function matrix. These size differences in gain terms can cause an overpowering of information within the frequency analysis, most prominently in the cross-spectral density calculation as discussed by Lathi and Ding (2010) and Proakis and Salehi (2014). The gain terms of the transfer functions of the Wood-Berry distillation column, seen in (4.7), are within the same range, therefore, no scaling was required.

Since the transfer function matrix in (5.17) consists purely of LTI systems, the homogeneity property of an LTI system, can be used to scale the plant model in (5.17). To scale the transfer functions of (5.17) so that all gains are within the same order, the following scaling matrices were derived from the constraints and operating points as described by Coetzee et al. (2010). Furthermore, the scaling matrices were adjusted to ensure full observability, and therefore establish the success of the Kalman-filter. The MV scaling matrix ($u_{scaling}$) and the CV scaling matrix ($y_{scaling}$) is:

$$u_{scaling} = \begin{bmatrix} 150 & 0 & 0 \\ 0 & 326 & 0 \\ 0 & 0 & 372.8 \end{bmatrix} \tag{5.19a}$$

$$y_{scaling} = \begin{bmatrix} 0.015 & 0 & 0 \\ 0 & 0.02 & 0 \\ 0 & 0 & 25 \end{bmatrix}. \tag{5.19b}$$

As described by Skogestad and Postlethwaite (2010), the multivariable plant in (5.17) can then be scaled as follows:

$$G_{\text{scaled}} = y_{scaling}^{-1} G u_{scaling}$$

$$= \begin{bmatrix} 0.015 & 0 & 0 \\ 0 & 0.02 & 0 \\ 0 & 0 & 25 \end{bmatrix}^{-1} G \begin{bmatrix} 150 & 0 & 0 \\ 0 & 326 & 0 \\ 0 & 0 & 372.8 \end{bmatrix}$$

$$= \begin{bmatrix} \frac{200}{3} & 0 & 0 \\ 0 & 50 & 0 \\ 0 & 0 & 0.04 \end{bmatrix} G \begin{bmatrix} 150 & 0 & 0 \\ 0 & 326 & 0 \\ 0 & 0 & 372.8 \end{bmatrix} \tag{5.20}$$

$$= \begin{bmatrix} 10000 & 21733 & 24853 \\ 7500 & 16300 & 18640 \\ 6 & 13.0400 & 14.9120 \end{bmatrix} \cdot \begin{bmatrix} \frac{-9.892\times10^{-5}}{0.4924s+1}e^{-0.0444s} & \frac{-5.208\times10^{-4}}{0.187s+1} & \frac{1.927\times10^{-4}}{0.04758s+1} \\ \frac{4.302\times10^{-4}}{0.3173s+1} & \frac{2.774\times10^{-4}}{s}e^{-0.0472s} & \frac{-3.131\times10^{-4}}{0.2355s+1}e^{-0.0528s} \\ \frac{-45.35}{53.07s+1} & \frac{13.07}{8.277s+1}e^{-0.025s} & \frac{91.99}{93.68s+1} \end{bmatrix}$$

$$= \begin{bmatrix} \frac{-0.9892}{0.4924s+1}e^{-0.0444s} & \frac{-11.32}{0.187s+1} & \frac{4.79}{0.04758s+1} \\ \frac{3.226}{0.3173s+1} & \frac{4.522}{s}e^{-0.0472s} & \frac{-5.836}{0.2355s+1}e^{-0.0528s} \\ \frac{-272.1}{53.07s+1} & \frac{170.4}{8.277s+1}e^{-0.025s} & \frac{1372}{93.68s+1} \end{bmatrix}.$$

5.4 SIMULATION OF THE GRINDING MILL CIRCUIT

Before the PMR method can be tested on the non-linear plant, the methodology should be tested on the linear process as described in (5.17). Therefore, using a similar simulation structure as described in Section 4.3.2, the scaled linear model will be used as the basis of the MPC while MPM will be applied to (5.17) and therefore realize a plant that differs from the model being used in the model-based controller.

5.4.1 Model-Plant Mismatch Applied

5.4.1.1 Uncertainty Description

The following uncertainty descriptions in (5.21) for model parameters in a grinding mill circuit were developed by Craig and MacLeod (1995) and will form the basis of the MPM applied to (5.20) as this represents a realistic expectation of process changes at different operating conditions.

$$K_{ij} = \begin{bmatrix} 31\% & 14\% & 31\% \\ 65\% & 11\% & 16\% \\ - & - & - \end{bmatrix} \tag{5.21a}$$

$$\tau_{ij} = \begin{bmatrix} 18\% & - & 19\% \\ 40\% & - & 60\% \\ - & - & - \end{bmatrix} \tag{5.21b}$$

$$D_{ij} = \begin{bmatrix} 27\% & - & - \\ - & - & 43\% \\ - & - & - \end{bmatrix}. \tag{5.21c}$$

5.4.1.2   Model-Plant Mismatch Applied for Initial Testing

To evaluate the PMR for a grinding mill, an initial set of parameter mismatches are applied to (5.20). These mismatches, as seen in (5.22), are based on the uncertainty location in (5.21) but with a lower absolute value to ensure reproducibility of all results as well as unique direction changes to simulate how a real plant can vary.

$$K_{ij} = \begin{bmatrix} +5\% & +5\% & +5\% \\ -5\% & -5\% & -5\% \\ - & - & - \end{bmatrix} \tag{5.22a}$$

$$\tau_{ij} = \begin{bmatrix} +5\% & - & +5\% \\ -5\% & - & -5\% \\ - & - & - \end{bmatrix} \tag{5.22b}$$

$$D_{ij} = \begin{bmatrix} +5 \text{ samples} & - & - \\ - & - & -5 \text{ samples} \\ - & - & - \end{bmatrix}. \tag{5.22c}$$

5.4.2   Controller Design and Simulation Description

5.4.2.1   Controller Design

The plant of (5.17) will be controlled using an MPC controller. The controller is a linear constrained MPC controller (as in (4.4)), based on the scaled version of the transfer function, seen in (5.20), obtained using SID (Qin and Badgwell, 2003). A Kalman-filter is used to estimate the states of the

system from the plant outputs based on the model of the plant before MPM is introduced (Grewal and Andrews, 2001).

The plant is discretized using a sampling time of 10 seconds, and a third-order Padé approximation is used to absorb the delay into the state space representation (Trefethen, 2019). The prediction horizon (N_p) is chosen as 50 and the control horizon (N_c) is chosen as 10 while $Q = \text{diag}[100, 100, 50]$ and $R = \text{diag}[10, 10, 10]$ for the cost function in (4.4b). The plant is controlled to the extent that no constraints are reached.

5.4.2.2 Simulation Description

The simulation of the plant was done using the system seen in Figure 5.5. Both the plant and model outputs are logged for use with the PMR algorithm along with the setpoints. As with a realistic system, the controlled variables of the plant are used in conjunction with a Kalman-filter to estimate the process states. The estimated states along with the required setpoints are fed back into the MPC to determine the required MVs applied to both the model and the plant.

To ensure that the required adequate excitation is applied to the process, pseudo-random binary sequences, with a maximum switching time of 10 times the sampling time, are used as reference signals. AWGN signals, with a power-to-noise ratio of 0.1, are added to the plant outputs to simulate output disturbances. All setpoints were perturbed at the same time, with different pseudo-random binary sequences. If perturbations were applied to individual setpoints at a time, the low-frequency interference to the CSD as described in Section 3.5 is observed.
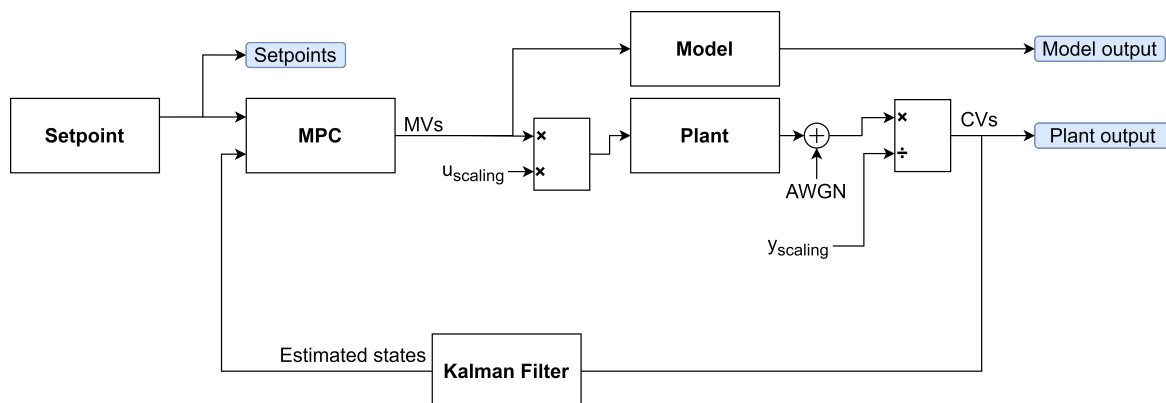

Figure 5.5. Grinding mill feedback loop.

5.4.3   Initial Simulation Results

The first simulation of the grinding mill circuit made use of the MPM as described by (5.22). This will allow for an adequate evaluation of the PMR applied to the mill.

5.4.3.1   Plant

The plant after application of the MPM in (5.22) is:

$$
\begin{bmatrix} y_{PSE} \\ y_{J_T} \\ y_{SLEV} \end{bmatrix} = \begin{bmatrix} \frac{-1.039 \times 10^{-4}}{0.5171+1} e^{-0.0583} & \frac{-5.468 \times 10^{-4}}{0.187s+1} & \frac{2.024 \times 10^{-4}}{0.04996s+1} \\ \frac{4.087 \times 10^{-4}}{0.3014+1} & \frac{2.635 \times 10^{-4}}{s} e^{-0.0472s} & \frac{-2.975 \times 10^{-4}}{0.2238s+1} e^{-0.0389s} \\ \frac{-45.35}{53.07s+1} & \frac{13.07}{8.277s+1} e^{-0.025s} & \frac{91.99}{93.68s+1} \end{bmatrix} \begin{bmatrix} u_{CFF} \\ u_{MFO} \\ u_{SFW} \end{bmatrix}. \quad (5.23)
$$

5.4.3.2   Results

Step 1 - Gain Mismatch

The MPM in the gain term of all transfer functions in the transfer function matrix can be determined using the zero-frequency term of the PMR magnitude spectra as seen in Figure 5.6.

$$
\text{Gain MPM} = (|\mathbf{G_{PMR}}(0)| - 1) \times 100
$$

$$
= \left(\begin{bmatrix} 1.0269 & 1.0266 & 1.0259 \\ 0.9782 & 1.0541 & 1.0020 \\ 1.0000 & 1.0000 & 1.0000 \end{bmatrix} - 1 \right) \times 100
$$

$$
= \begin{bmatrix} 2.6948\% & 2.6604\% & 2.5864\% \\ -2.1751\% & 5.4115\% & 0.2009\% \\ -0\% & 0\% & -0\% \end{bmatrix}. \quad (5.24)
$$

Step 2 - Time Constant Mismatch

The relative time constant mismatches can be deduced from the linear fitted line (orange line) to the

initial slope of the PMR magnitude spectrum as seen in Figure 5.7.

$$\text{Time Constant MPM} = \widehat{\alpha}_{\mathbf{G_{PMR}}} \times -100$$

$$= \begin{bmatrix} 2.0230 & 0.3350 & 0.1350 \\ -0.5810 & 18.1410 & 1.2250 \\ 0 & 0 & 0 \end{bmatrix} \times -100 \tag{5.25}$$

$$= \begin{bmatrix} -202.30 & -33.50 & -13.50 \\ 58.10 & -1814.10 & -122.50 \\ 0 & 0 & 0 \end{bmatrix}.$$
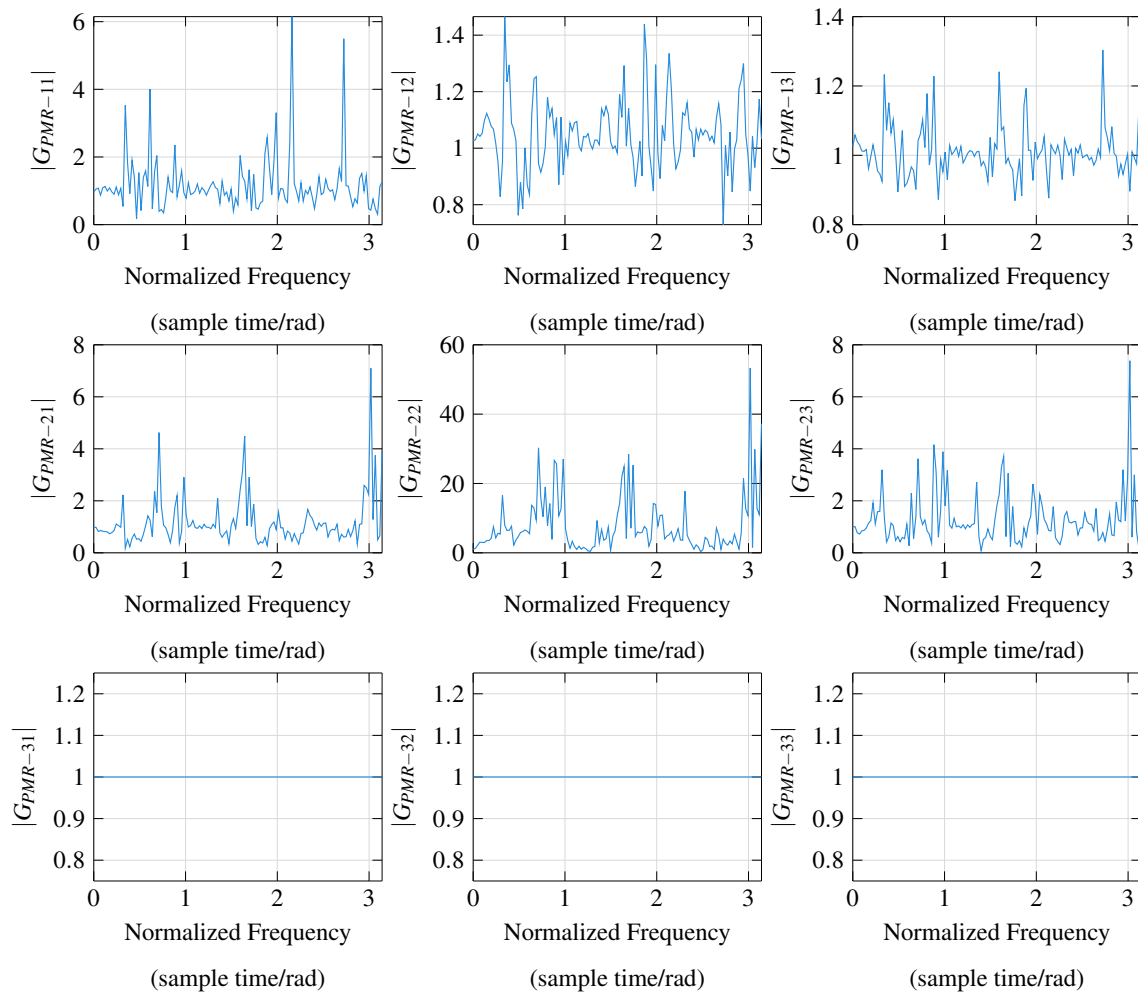
Figure 5.6. PMR magnitude spectra for the simulation study of scenario 1 applied to the linear model of the grinding mill.
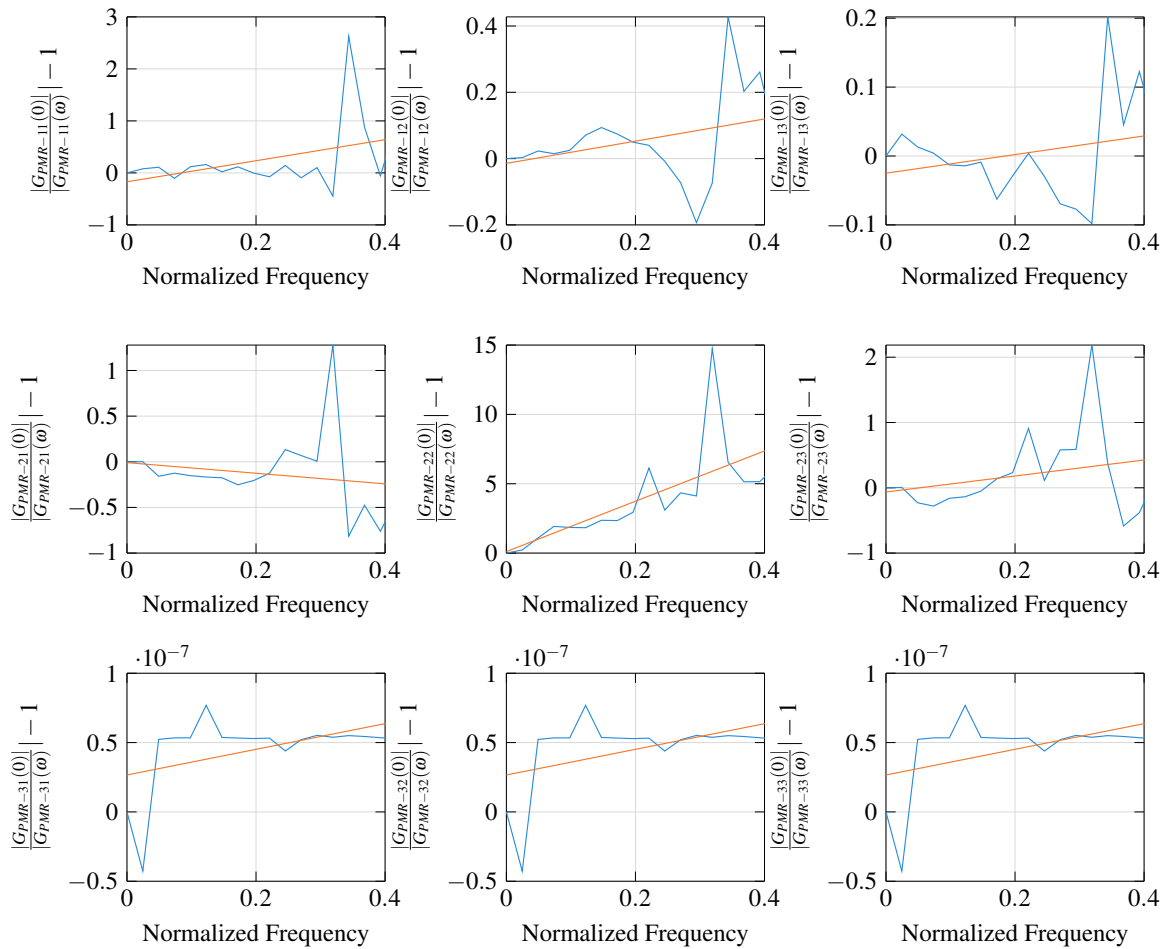
Figure 5.7. Initial slope of PMR magnitude spectra for the simulation study of scenario 1 applied to the linear model of the grinding mill.

Step 3 - Delay Mismatch

Finally, the time delay mismatch can be estimated using the optimal delay estimation technique, described in Section 3.3.1, with the results of the cost function visible in Figure 5.8.

$$\text{Delay MPM} = \begin{bmatrix} -5 \text{ samples} & 0 \text{ samples} & 0 \text{ samples} \\ 0 \text{ samples} & -16 \text{ samples} & -10 \text{ samples} \\ 0 \text{ samples} & 0 \text{ samples} & 0 \text{ samples} \end{bmatrix}. \tag{5.26}$$

5.4.3.3   Discussion of Results

From (5.24), (5.25) and (5.26) it is evident that there does not exist a strong correlation between the diagnosed MPM and the MPM applied to the grinding mill as described by (5.22). The differences

between the MPM applied and the diagnosed MPM can be quantified as:

$$K \text{ MPM error} = \frac{K \text{ MPM diagnosed} - K \text{ MPM applied}}{K \text{ MPM applied}}$$

$$= \begin{bmatrix} -0.4610 & -0.4679 & -0.4827 \\ -0.5650 & -2.0823 & -1.0402 \\ \emptyset & \emptyset & \emptyset \end{bmatrix} \tag{5.27a}$$

Figure 5.8. Objective function results for the simulation study of scenario 1 applied to the linear model of the grinding mill.
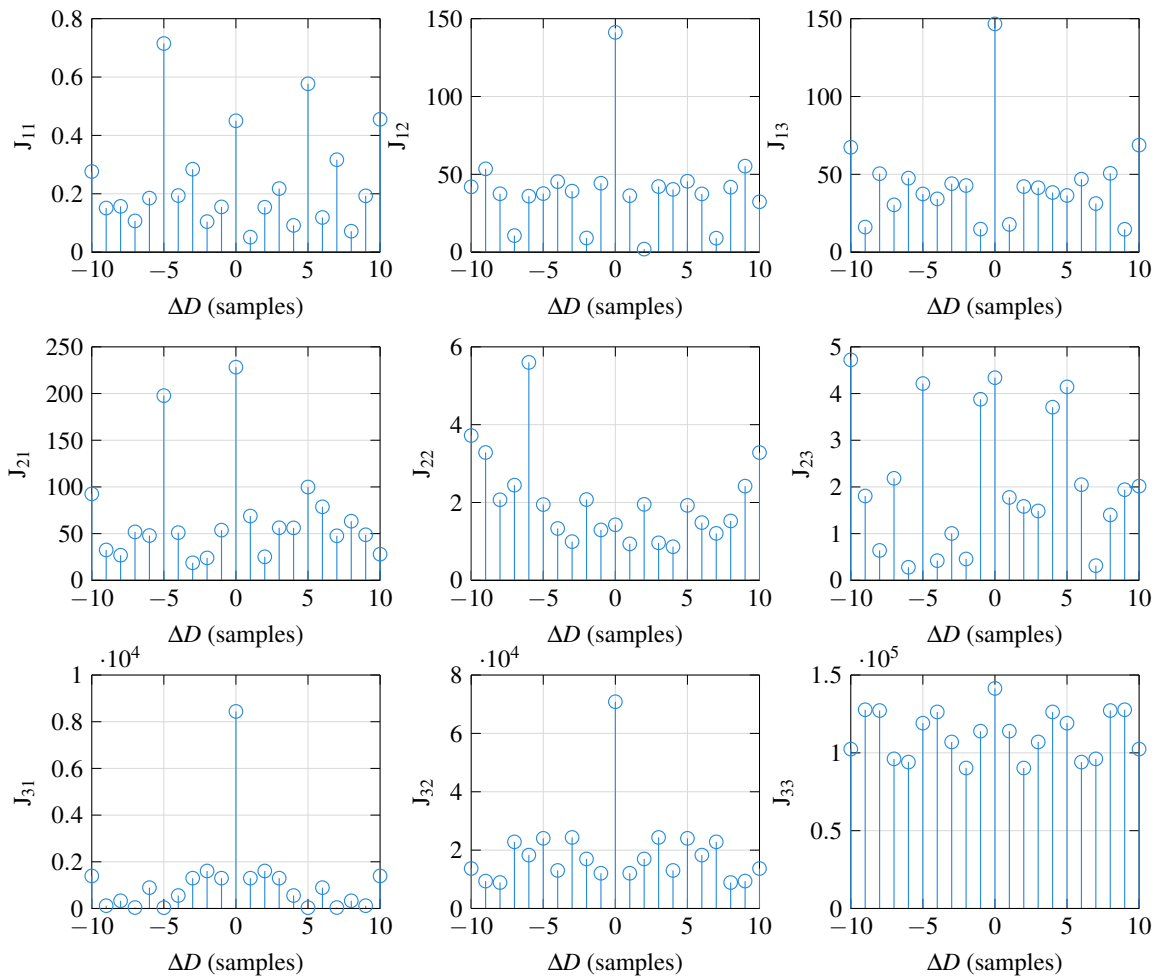
$$\tau \text{ MPM error} = \frac{\tau \text{ MPM diagnosed} - \tau \text{ MPM applied}}{\tau \text{ MPM applied}}$$

$$= \begin{bmatrix} -41.4600 & -\infty & -3.7000 \\ -12.6200 & -\infty & 23.5000 \\ \emptyset & \emptyset & \emptyset \end{bmatrix} \quad (5.27b)$$

$$D \text{ MPM error} = \frac{D \text{ MPM diagnosed} - D \text{ MPM applied}}{D \text{ MPM applied}}$$

$$= \begin{bmatrix} 0 & \emptyset & \emptyset \\ \emptyset & -\infty & 1 \\ \emptyset & \emptyset & \emptyset \end{bmatrix}. \quad (5.27c)$$

The undefined ($\emptyset$) values of (5.27) indicates locations where no MPM was applied and no MPM was diagnosed. The infinity values of (5.27) indicates where no MPM was applied but some MPM was diagnosed. The negative symbols indicate diagnosis in the opposite direction than applied while the size of the values in (5.27) quantifies the amount by which the MPM was misdiagnosed.

By considering these results it is evident that some MPM is correctly diagnosed while others are misdiagnosed with more detail on the misdiagnosis provided in Section 5.4.4.3.

5.4.4 Full Uncertainty Simulation Results

The second simulation of the grinding mill circuit made use of the uncertainty MPM as described by (5.21).

5.4.4.1 Plant

The plant after application of the MPM in (5.21) is:

$$\begin{bmatrix} y_{PSE} \\ y_{J_T} \\ y_{SLEV} \end{bmatrix} = \begin{bmatrix} \frac{-1.296 \times 10^{-4}}{0.5811s+1} e^{-0.119} & \frac{-5.937 \times 10^{-4}}{0.187s+1} & \frac{2.525 \times 10^{-4}}{0.05662s+1} \\ \frac{7.098 \times 10^{-4}}{0.4442s+1} & \frac{3.079 \times 10^{-4}}{s} e^{-0.0472s} & \frac{-3.632 \times 10^{-4}}{0.3769s+1} e^{-0.172} \\ \frac{-45.35}{53.07s+1} & \frac{13.07}{8.277s+1} e^{-0.025s} & \frac{91.99}{93.68s+1} \end{bmatrix} \begin{bmatrix} u_{CFF} \\ u_{MFO} \\ u_{SFW} \end{bmatrix}. \quad (5.28)$$

5.4.4.2 Results

Step 1 - Gain Mismatch

The MPM in the gain term of all transfer functions in the transfer function matrix can be determined using the zero-frequency term of the PMR magnitude spectra as seen in Figure 5.9.

$$\text{Gain MPM} = (|\mathbf{G_{PMR}}(0)| - 1) \times 100$$

$$= \left(\begin{bmatrix} 1.5682 & 1.2131 & 1.4884 \\ 1.7347 & 5.9025 & 1.2706 \\ 1.0000 & 1.0000 & 1.0000 \end{bmatrix} - 1 \right) \times 100 \tag{5.29}$$

$$= \begin{bmatrix} 56.8222\% & 21.3124\% & 48.8449\% \\ 73.4657\% & 490.2528\% & 27.0557\% \\ 0.0003\% & 0.0003\% & 0.0003\% \end{bmatrix}.$$
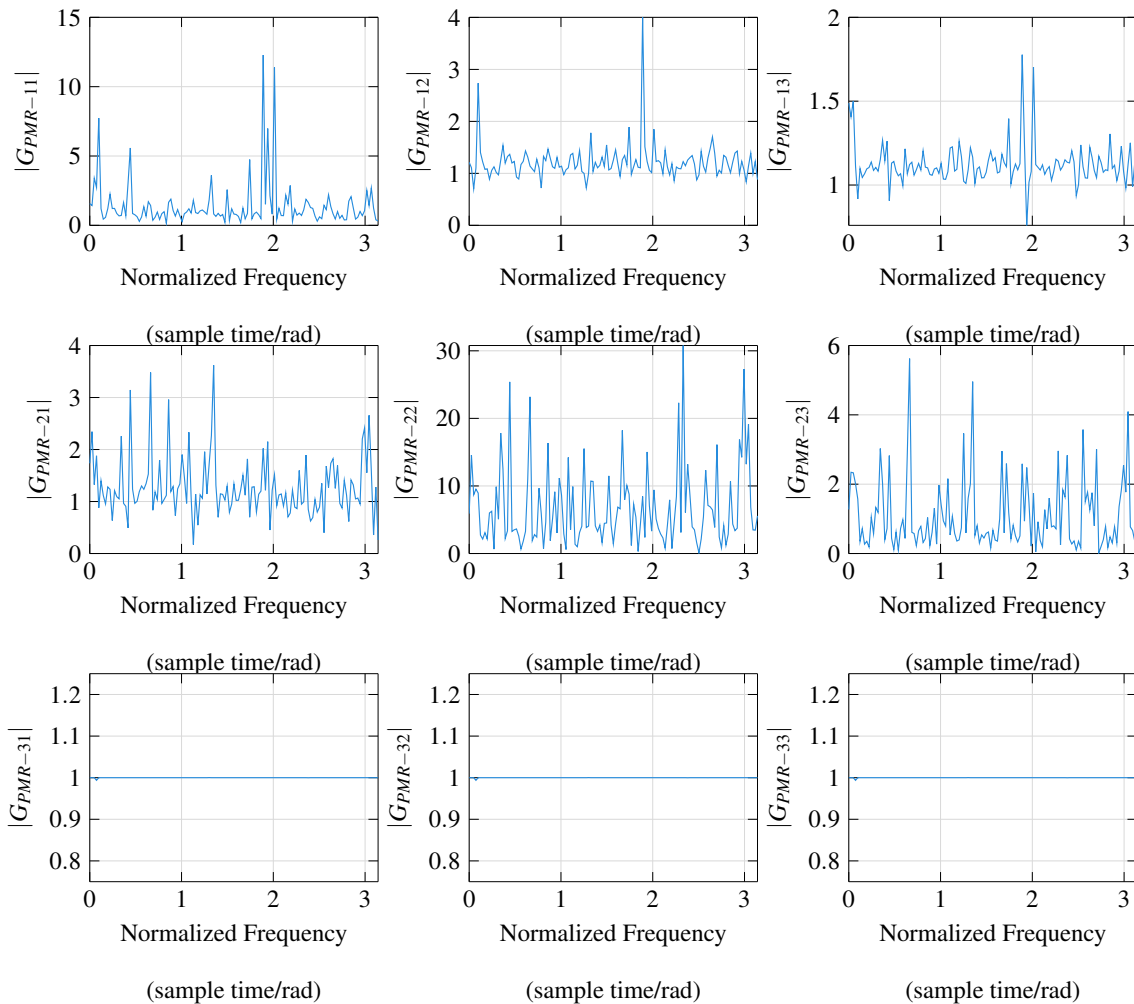

Figure 5.9. PMR magnitude spectra for the simulation study of scenario 2 applied to the linear model of the grinding mill.

Step 2 - Time Constant Mismatch

The relative time constant mismatches can be deduced from the linear fitted line (orange line) to the initial slope of the PMR magnitude spectrum as seen in Figure 5.10.

$$\text{Time Constant MPM} = \widehat{\alpha}_{\mathbf{G_{PMR}}} \times -100$$

$$= \begin{bmatrix} 2.0230 & 0.3350 & 0.1350 \\ -0.5810 & 18.1410 & 1.2250 \\ 0 & 0 & 0 \end{bmatrix} \times -100 \tag{5.30}$$

$$= \begin{bmatrix} -202.3000 & -33.5000 & -13.5000 \\ 58.1000 & -1814.1000 & -122.5000 \\ 0 & 0 & 0 \end{bmatrix}.$$

Step 3 - Delay Mismatch

Finally, the time delay mismatch can be estimated using the optimal delay estimation technique, described in Section 3.3.1, with the results of the cost function visible in Figure 5.11.

$$\text{Delay MPM} = \begin{bmatrix} 2 \text{ samples} & 0 \text{ samples} & 0 \text{ samples} \\ 0 \text{ samples} & 9 \text{ samples} & -2 \text{ samples} \\ 0 \text{ samples} & 0 \text{ samples} & 0 \text{ samples} \end{bmatrix}. \tag{5.31}$$

5.4.4.3 Discussion of Results

Once again, the applied MPM from (5.21) does not correspond to the MPM diagnosis in (5.29), (5.30) and (5.31). The differences between the MPM applied and the diagnosed MPM can be quantified as:

$$K \text{ MPM error} = \frac{K \text{ MPM diagnosed} - K \text{ MPM applied}}{K \text{ MPM applied}}$$

$$= \begin{bmatrix} -0.9677 & -0.9231 & -0.9677 \\ -0.9846 & -0.9091 & -0.9375 \\ \infty & \infty & \infty \end{bmatrix} \tag{5.32a}$$

$$\tau \text{ MPM error} = \frac{\tau \text{ MPM diagnosed} - \tau \text{ MPM applied}}{\tau \text{ MPM applied}}$$

$$= \begin{bmatrix} -12.2389 & -\infty & -1.7105 \\ 0.4525 & -\infty & -3.0417 \\ \varnothing & \varnothing & \varnothing \end{bmatrix} \tag{5.32b}$$

$$D \text{ MPM error} = \frac{D \text{ MPM diagnosed} - D \text{ MPM applied}}{D \text{ MPM applied}}$$

$$= \begin{bmatrix} -1.0985 & \varnothing & \varnothing \\ \varnothing & \infty & -0.9264 \\ \varnothing & \varnothing & \varnothing \end{bmatrix}. \tag{5.32c}$$

5.5   INCOMPATIBILITIES OF THE PMR AND A GRINDING MILL

Even though the results for the feasibility of using the PMR to detect MPM for MIMO FOPTD process under MPC, from (5.27) and (5.32) looks promising, it is evident that the PMR as a method of detecting
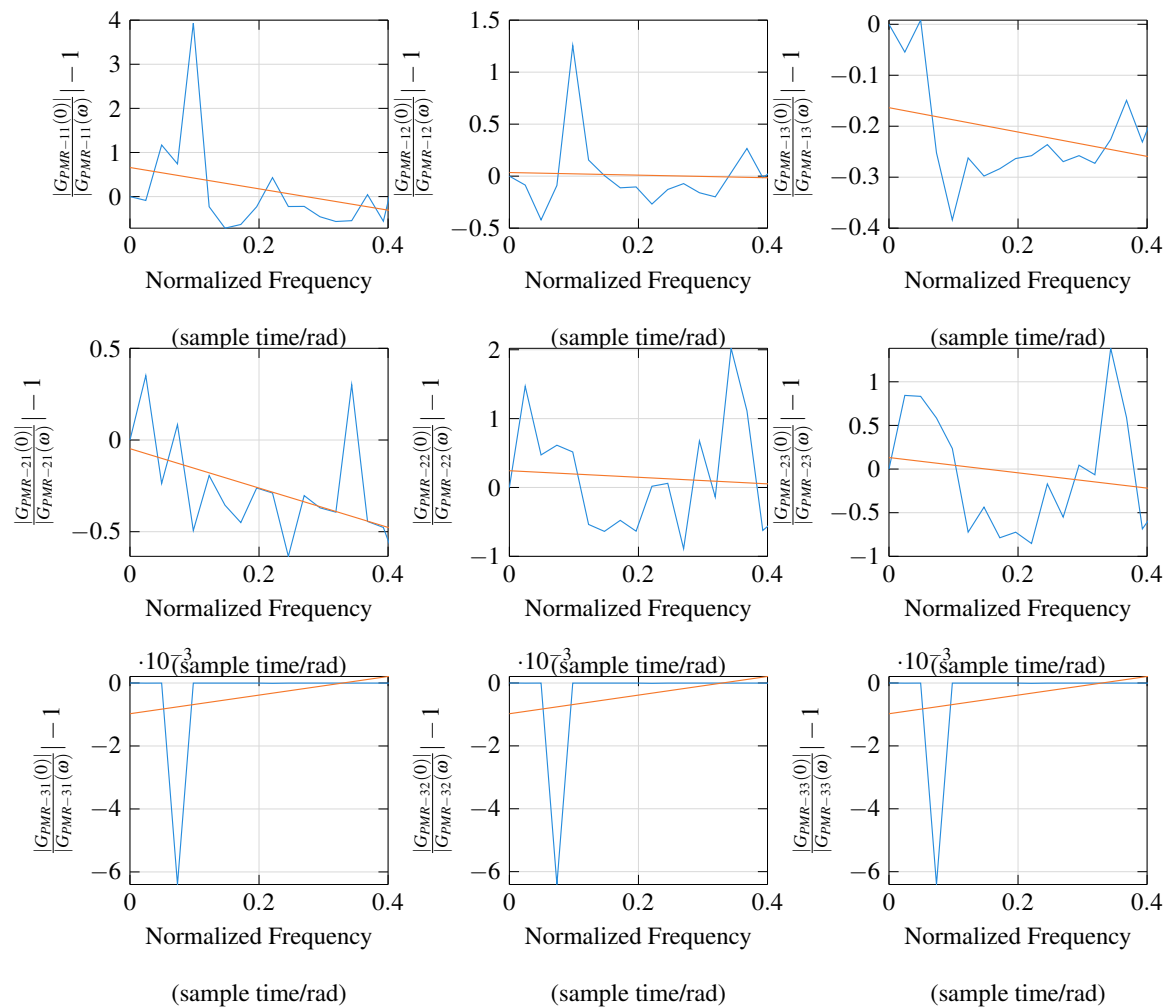
Figure 5.10. Initial slope of PMR magnitude spectra for the simulation study of scenario 2 applied to the linear model of the grinding mill.

MPM for a grinding mill under MPC is not a viable option. The inability of the PMR to diagnose the MPM for grinding mills boils down to one of two sources, described in Section 5.5.1 and Section 5.5.2, with both causes stemming for the fact that the PMR is a frequency-based analysis.

5.5.1   Overpowering of a Cross-Spectral Density

As briefly mentioned in Section 5.3.2, it is possible that the relative size between two CSDs can overpower the spectral analysis. Recall, from (3.31), that the PMR is estimated as a ratio of two CSDs $(\widehat{G}_{PMR} = \frac{\widehat{\gamma}_{y,r}(\omega)}{\widehat{\gamma}_{\hat{y},r}(\omega)})$ and that the estimation of the MIMO PMR includes a ratio of CSDs between all process outputs and model outputs seen in (3.55).

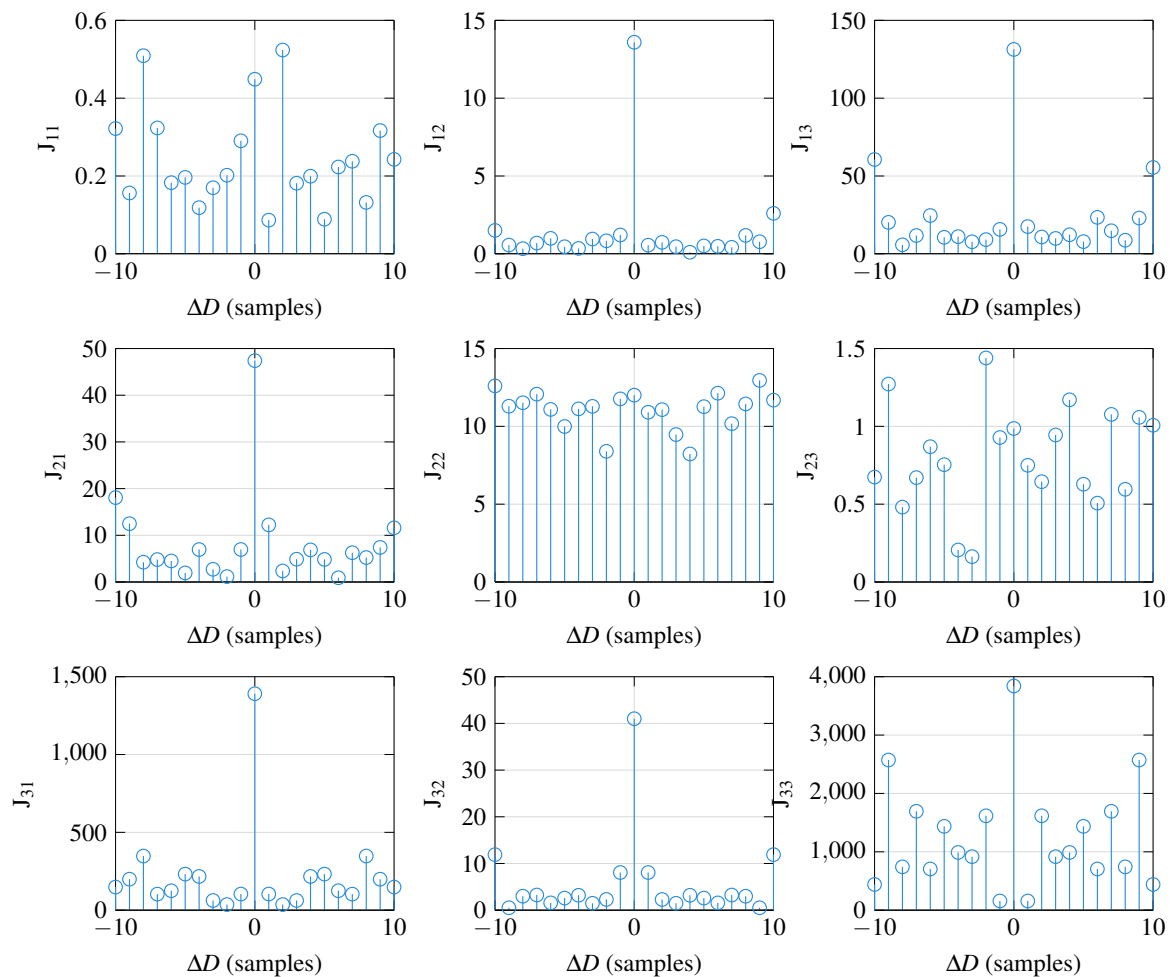**Figure 5.11.** Objective function results for the simulation study of scenario 2 applied to the linear model of the grinding mill.

Considering the mathematical formulation of the CSD as described by Oppenheim (1999):

$$P_{xy}(\omega) = \sum_{m=-\infty}^{\infty} R_{xy}(m)e^{-j\omega m}, \tag{5.33a}$$

where R_{xy} is the cross-correlation sequence between signals x and y, defined as:

$$R_{xy}(m) = E\left\{x_{n+m}y_n^*\right\} = E\left\{x_n y_{n-m}^*\right\}, \tag{5.33b}$$

the trivial connection between the absolute size of the signals (x and y) and the absolute size of the CSD can be made. Applying this deduction to the CSD of the MIMO PMR estimation, it is evident that if the process being diagnosed does not have gains within the same order, the ratio of the PMR ($\widehat{G}_{PMR} = \frac{\widehat{\gamma}_{y,r}(\omega)}{\widehat{\gamma}_{\hat{y},r}(\omega)}$) might be overpowered by model outputs having a different output size (larger or smaller) when compared to the process output size.

Seeing that this limitation of the PMR is accounted for by normalizing the gain values of all transfer functions within the MIMO transfer function of (5.20), the PMR incompatibility with the grinding mill circuit should be accredited to the dynamic imbalance within the system.

5.5.2 Dynamic Imbalance of the Plant

To formulate the dynamic imbalance limitation of the PMR, recall that the PMR can be represented by a polar representation (3.2):

$$G_{PMR}(e^{j\omega}) = \frac{|G(e^{j\omega})|e^{j\angle \underline{G}(e^{j\omega})}e^{-jD\omega}}{|\hat{G}(e^{j\omega})|e^{j\angle \hat{G}(e^{j\omega})}e^{-j\hat{D}\omega}}. \tag{5.34}$$

This polar representation of the PMR reveals that both the magnitude spectrum as well as the phase spectrum are influenced by a time constant mismatch. Furthermore, as discussed in Section 3.2, the time constant mismatch diagnosis consists of a linearity check on the rate of change of the PMR magnitude spectrum. Therefore, if certain models within the MIMO transfer function have faster dynamics when compared to other transfer functions, some frequency-based information might be filtered out, rendering the PMR less effective.

It should be noted that, as stated in section 3.2, the PMR is developed for FOPTD systems. Nonetheless, (5.17) contains a pure integrator, instead of fully consisting of FOPTD transfer functions. This does not pose a problem seeing that the PMR was developed to identify the MPM, without any knowledge of the system, under the assumption that all models of the system are FOPTD. Since the PMR is an offline method and has no effect on the closed-loop performance of the system, the PMR can accommodate pure integrators, interpreted as FOPTD models with the dynamics of the transfer function being magnitudes slower compared to the other models in the system.
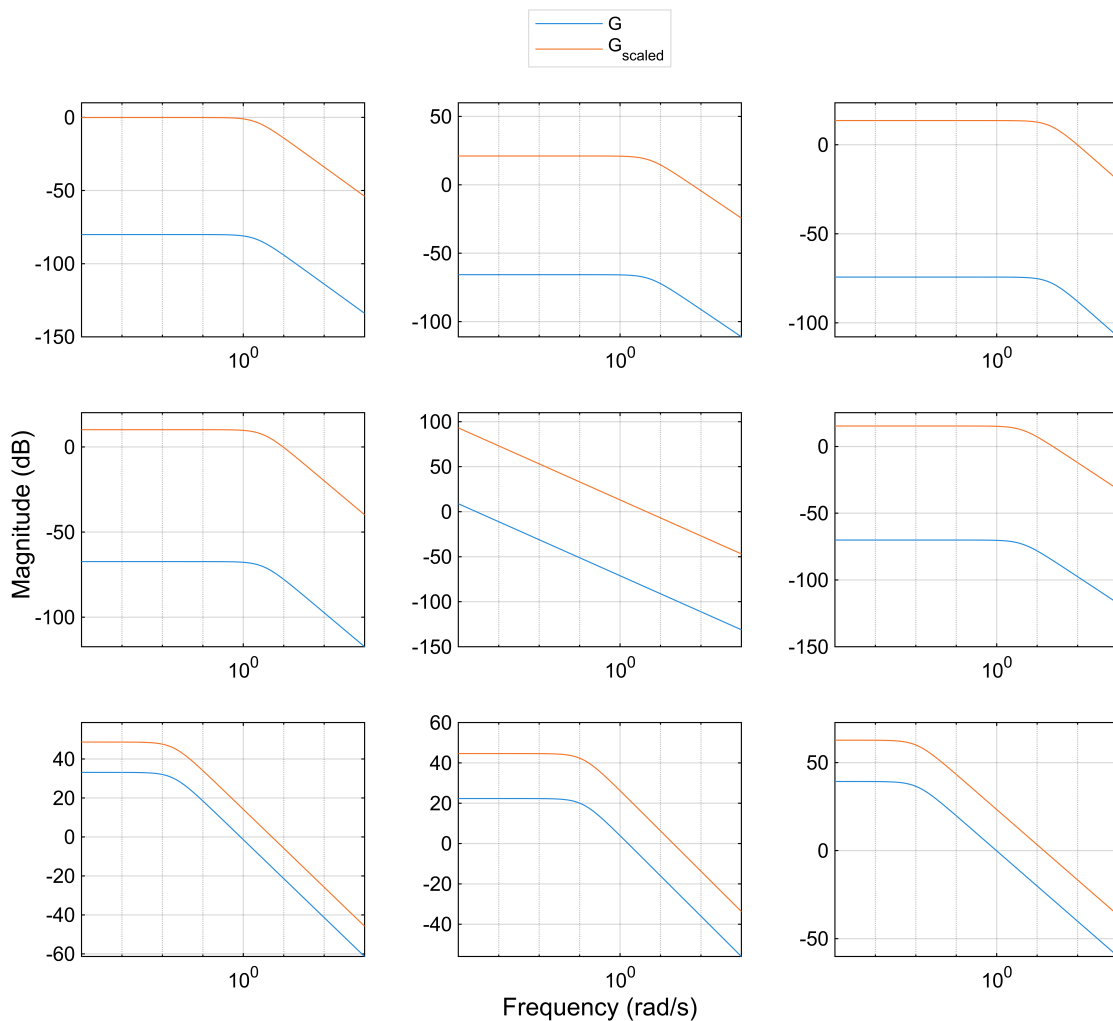
Figure 5.12. Bode magnitude of G and G_{scaled}.

5.5.3 PMR Limitations

For the instance of the grinding mill circuit, obtaining a Bode magnitude plot of both (5.17) and (5.20) allows the verification and qualitative analysis of both limitations of the PMR, with Figure 5.12 providing a further quantitative representation of the limitations.

The first limitation of overpowering the cross-spectral density can be visualized by observing the large size differences of the blue lines in Figure 5.12, noting that the figures use logarithmic scales. The second limitation, the dynamic imbalances within the plant, can be observed by inspecting the roll off rates and the critical frequencies of the orange lines in Figure 5.12, where the gain terms of the transfer matrix have been normalized. The dynamic imbalances within the plant can clearly be seen between example $G_{scaled-22}$ and $G_{scaled-12}$ or $G_{scaled-11}$ and $G_{scaled-31}$. These dynamic imbalances will cause certain parts of the plant to react faster to the setpoint changes while the rest of the plant lags behind,

causing a filtering effect on some frequency-based information.

5.6 CHAPTER SUMMARY

Focus was placed, in this chapter, on the application of the PMR to a grinding mill circuit. To obtain a model that represents a real-world grinding mill, a non-linear model was presented using a population volume balance with the aim of using this non-linear model as a real-world plant where setpoint changes lead to MPM for a linear system fitted to a specific operating point of the mill. To achieve this, SID was applied to the grinding mill to realize a FOPTD representation of the plant. An initial set of tests were conducted using an uncertainty description of a grinding mill to quantify realistic mismatches applied to the system. The results obtained from the grinding mill simulation were contrary to those obtained in Chapter 4, and therefore no further simulations were conducted. In addition to the results, a brief exploration of the cause of the unfavourable results was investigated to pinpoint the exact reason for the incompatibility between the PMR and a grinding mill circuit.

CHAPTER 6   CONCLUSION

This study focussed on the development of a method to detect, isolate and diagnose MPM within process control, and more specifically the minerals processing environment. By using the literature study to identify the state-of-the-art methods of MPM detection, the approach of the PMR was chosen to be investigated.

With the derivation of the PMR diagnosis procedure, two trivial limitations of the PMR could be identified. These limitations are that the PMR can only be used with processes that conform to a deviation variable model as well as the PMR will require setpoint excitation over a range or band of frequencies.

Collectively the PMR could be classified as an accurate and dependable MPM diagnosis tool, under specific conditions. The PMR developed for SISO systems showed remarkable capabilities of diagnosing the MPM to a specific parameter in the FOPTD transfer function. The size and direction of the mismatch could also be diagnosed relative to the applied mismatch, indicating an accurate method of diagnosing the MPM and providing insight into the online plant changes while being controlled. Furthermore, the MIMO PMR was evaluated on the Wood-Berry distillation column with positive results. The MIMO PMR estimation was able to decouple all the process outputs, allowing for the isolation of mismatch within the transfer function matrix, which could once again be used by the SISO PMR diagnosis procedure to identify the mismatched FOPTD parameter and diagnose the size and direction of the mismatch.

Even though the PMR did not realize favourable results when applied to a grinding mill circuit, the application of the PMR to the grinding mill allowed the exploration of limitations within the method and two limitations, not mentioned in the literature, could be established. The limitation of overpowering

the CSD could easily be mitigated by scaling the model of the plant as discussed previously. Future work could stem from the limitation of dynamic imbalance within the plant. This includes:

- The development of a PMR methodology that separates the fast process dynamics from the slow process dynamics of a grinding mill and therefore alleviates the dynamic imbalance limitation.
- The development of a transfer function reduction technique that will allow the PMR to include certain transfer functions, where MPM is expected, into the PMR while excluding transfer functions where MPM is unlikely to be present

Future work also includes the quantification of dynamic differences for which the PMR would result in an accurate MPM diagnosis.

From this investigation into the proposed methodology, the PMR in the current form, is a viable approach to detecting, isolating and diagnosing MPM for systems in the process industry given that the system dynamics are within the same order.

REFERENCES

Al-Muthairi, N. F. and Bingulac, S. (1995). An algorithm for calculating Markov parameters from transfer function matrices, *Computers & Electrical engineering* **21**(2): 77–87.

Azhin, M., Silva-Aires, P., Popli, K., Afacan, A., Liu, Q. and Prasad, V. (2022). State Estimation of a Flotation Column using Fundamental Dynamic Models, *IFAC-PapersOnLine* **55**(21): 108–113.

Badwe, A. S., Gudi, R. D., Patwardhan, R. S., Shah, S. L. and Patwardhan, S. C. (2009). Detection of model-plant mismatch in MPC applications, *Journal of Process Control* **19**(8): 1305–1313.

Bagyaveereswaran, V., Mathur, T. D., Gupta, S. and Arulmozhivarman, P. (2016). Performance comparison of next generation controller and MPC in real time for a SISO process with low cost DAQ unit, *Alexandria Engineering Journal* **55**(3): 2515–2524.

Basseville, M. and Benveniste, A. (1983). Sequential segmentation of nonstationary digital signals using spectral analysis, *Information Sciences* **29**(1): 57–73.

Basseville, M. and Nikiforov, I. V. (1993). *Detection of Abrupt Changes: Theory and Application*, Prentice Hall, Englewood Cliffs.

Botha, S., le Roux, J. and Craig, I. (2018). Hybrid non-linear model predictive control of a run-of-mine ore grinding mill circuit, *Minerals Engineering* **123**: 49–62.

Camacho, E. F. and Bordons, C. (1999). *Model Predictive Control*, Advanced Textbooks in Control and Signal Processing, Springer, Berlin; New York.

REFERENCES

Chen, G., Xie, L., Zeng, J., Chu, J. and Gu, Y. (2013). Detecting model–plant mismatch of nonlinear multivariate systems using mutual information, *Industrial & Engineering Chemistry Research* **52**(5): 1927–1938.

Coetzee, L. C., Craig, I. K. and Kerrigan, E. C. (2010). Robust nonlinear model predictive control of a run-of-mine ore milling circuit, *IEEE Transactions on Control Systems Technology* **18**(1): 222–229.

Craig, I. K. and MacLeod, I. M. (1995). Specification framework for robust control of a run-of-mine ore milling circuit, *Control Engineering Practice* **3**(5): 621–630.

Darby, M. L. and Nikolaou, M. (2012). MPC: Current practice and challenges, *Control Engineering Practice* **20**(4): 328–342.

Gao, X., Yang, F., Shang, C. and Huang, D. (2016). A review of control loop monitoring and diagnosis: Prospects of controller maintenance in big data era, *Chinese Journal of Chemical Engineering* **24**(8): 952–962.

Grewal, MS. and Andrews, AP. (2001). *Kalman Filtering: Theory and Practice Using MATLAB*, 2nd edn, Wiley, New York.

Groenewald, J. and Aldrich, C. (2015). Root cause analysis of process fault conditions on an industrial concentrator circuit by use of causality maps and extreme learning machines, *Minerals Engineering* **74**: 30–40.

Hamon, BV. and Hannan, EJ. (1974). Spectral estimation of time delay for dispersive and non-dispersive systems, *Journal of the Royal Statistical Society Series C: Applied Statistics* **23**(2): 134–142.

Han, R., Salehi, Y., Huang, B. and Prasad, V. (2021). State estimation for multirate measurements in the presence of integral term and variable delay, *IEEE Transactions on Control Systems Technology* **29**(6): 2416–2426.

REFERENCES

Hodouin, D. (2011). Methods for automatic control, observation, and optimization in mineral processing plants, *Journal of Process Control* **21**(2): 211–225.

Holten, L., Gjelsvik, A., Aam, S., Wu, F. F. and Liu, W.-H. (1988). Comparison of different methods for state estimation, *IEEE Transactions on Power Systems* **3**(4): 1798–1806.

Ji, G., Zhang, K. and Zhu, Y. (2012). A method of MPC model error detection, *Journal of Process Control* **22**(3): 635–642.

Jiang, H., Huang, B. and Shah, S. L. (2009). Closed-loop model validation based on the two-model divergence method, *Journal of Process Control* **19**(4): 644–655.

Kaw, S., Tangirala, A. K. and Karimi, A. (2014). Improved methodology and set-point design for diagnosis of model-plant mismatch in control loops using plant-model ratio, *Journal of Process Control* **24**(11): 1720–1732.

Larsen, L. F., Izadi-Zamanabadi, R. and Wisniewski, R. (2007). Supermarket refrigeration system-benchmark for hybrid system control, *2007 European Control Conference (ECC)*, IEEE, pp. 113–120.

Lathi, B. P. and Ding, Z. (2010). *Modern Digital and Analog Communication Systems*, The Oxford Series in Electrical and Computer Engineering, 4th edn, Oxford University Press.

Le Roux, J. D., Craig, I. K., Hulbert, DG. and Hinde, AL. (2013). Analysis and validation of a run-of-mine ore grinding mill circuit model for process control, *Minerals Engineering* **43**: 121–134.

Le Roux, J. D., Steinboeck, A., Kugi, A. and Craig, I. K. (2020). Steady-state and dynamic simulation of a grinding mill using grind curves, *Minerals Engineering* **152**: 106208.

Le Roux, J. D. and Steyn, C. W. (2022). Validation of a dynamic non-linear grinding circuit model for process control, *Minerals Engineering* **187**: 107780.

Li, H., Jeong, S.-K., Yoon, J.-I. and You, S.-S. (2008). An empirical model for independent control of variable speed refrigeration system, *Applied Thermal Engineering* **28**(14-15): 1918–1924.

Li, L., Lu, L., Huang, Z., Chen, X. and Yang, S. (2020). A model mismatch assessment method of MPC by decussation, *ISA Transactions* **106**: 51–60.

Lindemann, M., Raethjen, J., Timmer, J., Deuschl, G. and Pfister, G. (2001). Delay estimation for cortico-peripheral relations, *Journal of Neuroscience Methods* **111**(2): 127–139.

Lindner, B., Chioua, M., Groenewald, J., Auret, L. and Bauer, M. (2018). Diagnosis of oscillations in an industrial mineral process using transfer entropy and nonlinearity index, *IFAC-PapersOnLine* **51**(24): 1409–1416.

Ling, D., Zheng, Y., Zhang, H., Yang, W. and Tao, B. (2017). Detection of model-plant mismatch in closed-loop control system, *Journal of Process Control* **57**: 66–79.

Ljung, L. (1999). *System Identification: Theory for the User*, Prentice Hall Information and System Sciences Series, 2nd edn, Prentice Hall PTR, Upper Saddle River, NJ.

Mayne, D. Q. (2014). Model predictive control: Recent developments and future promise, *Automatica* **50**(12): 2967–2986.

Mittermaier, H. K., Le Roux, J. D., Olivier, L. E. and Craig, I. K. (2023). Model-plant mismatch detection for a plant under Model Predictive Control: A grinding mill circuit case study, *IFAC-PapersOnLine* **56**(2): 11778–11783.

Niu, D., Chen, X.-s., Yang, J. and Zhou, X.-p. (2017). Disturbance rejection control for Raymond mill grinding system based on disturbance observer, *Journal of Central South University* **24**(9): 2019–2027.

Olivier, L. E. and Craig, I. K. (2011). Parameter mismatch detection in a run-of-mine ore milling circuit under Model Predictive Control, *IFAC PapersOnLine* **44**(1): 9929–9934.

REFERENCES

Olivier, L. E. and Craig, I. K. (2017). A survey on the degree of automation in the mineral processing industry, *2017 IEEE AFRICON*, pp. 404–409.

Oppenheim, A. V. (1999). *Discrete-Time Signal Processing*, Pearson Education, India.

Phan, M., Juang, J.-N. and Longman, R. W. (1991). On Markov parameters in system identification, *Technical report*, (No. NASA-TM-104156).

Priestley, M. B. (1981). *Spectral Analysis and Time Series*, Academic Press, London; New York.

Proakis, J. G. and Salehi, M. (2014). *Fundamentals of Communication Systems*, 2nd edn, Pearson, Boston.

Qin, S. and Badgwell, T. A. (2003). A survey of industrial model predictive control technology, *Control Engineering Practice* **11**(7): 733–764.

Rasmussen, H. and Larsen, L. F. (2009). Nonlinear superheat and capacity control of a refrigeration plant, *2009 17th Mediterranean Conference on Control and Automation*, IEEE, pp. 1072–1077.

Schwarz, M. P., Song, T., Yang, T., Zhou, J. and Wang, Q. (2019). Reconciliation of empirical correlations and CFD results for hydrocyclone performance for application in process modelling, *Minerals Engineering* **144**: 106028.

Schwenzer, M., Ay, M., Bergs, T. and Abel, D. (2021). Review on model predictive control: An engineering perspective, *International Journal of Advanced Manufacturing Technology* **117**(5): 1327–1349.

Seborg, D. E., Edgar, T. F., Mellichamp, D. A. and Doyle III, F. J. (2016). *Process Dynamics and Control*, John Wiley & Sons.

Selvanathan, S. and Tangirala, A. K. (2010a). Diagnosis of poor control loop performance due to model-plant mismatch, *Industrial & Engineering Chemistry Research* **49**(9): 4210–4229.

REFERENCES

Selvanathan, S. and Tangirala, AK. (2010b). Time-delay estimation in multivariate systems using Hilbert transform relation and partial coherence functions, *Chemical Engineering Science* **65**(2): 660–674.

Skogestad, S. and Postlethwaite, I. (2010). *Multivariable Feedback Control: Analysis and Design*, 2nd edn, Wiley, Chichester.

Song, C., Wang, P. and Makse, H. A. (2008). A phase diagram for jammed matter, *Nature* **453**(7195): 629–632.

Sun, Z., Qin, S. J., Singhal, A. and Megan, L. (2013). Performance monitoring of model-predictive controllers via model residual assessment, *Journal of Process Control* **23**(4): 473–482.

Taguchi, G. (2014). *Fault Tree Analysis of Slurry and Dewatered Taiings Management – a Framework*, PhD thesis, University of British Columbia.

Trefethen, L. N. (2019). *Approximation Theory and Approximation Practice, Extended Edition*, Society for Industrial and Applied Mathematics.

Tsai, Y., Gopaluni, R. B., Marshman, D. and Chmelyk, T. (2015). A novel algorithm for model-plant mismatch detection for model predictive controllers, *IFAC PapersOnLine* **48**(8): 746–752.

Varas, P., Carvajal, R. and Aguero, J. C. (2019). State Estimation for SAG Mills utilizing a simplified model with an alternative measurement, *2019 IEEE CHILEAN Conference on Electrical, Electronics Engineering, Information and Communication Technologies (CHILECON)*, IEEE, pp. 1–7.

Venkatasubramanian, V., Rengaswamy, R. and Kavuri, S. N. (2003). A review of process fault detection and diagnosis, *Computers & Chemical Engineering* **27**(3): 313–326.

Wakefield, B., Lindner, B., McCoy, J. and Auret, L. (2018). Monitoring of a simulated milling circuit: Fault diagnosis and economic impact, *Minerals Engineering* **120**: 132–151.

REFERENCES

Wang, L. (2009). *Model Predictive Control System Design and Implementation Using MATLAB*, Advances in Industrial Control, Springer, London.

Wang, S., Simkoff, J. M., Baldea, M., Chiang, L. H., Castillo, I., Bindlish, R. and Stanley, D. B. (2017). Autocovariance-based plant-model mismatch estimation for linear model predictive control, *Systems & Control Letters* **104**: 5–14.

Wang, Y., Yao, Y., Zheng, Y. and Wong, D. S. H. (2015). Multi-objective monitoring of closed-loop controlled systems using adaptive LASSO, *Journal of the Taiwan Institute of Chemical Engineers* **56**: 84–95.

Webber, J. R. and Gupta, Y. P. (2008). A closed-loop cross-correlation method for detecting model mismatch in MIMO model-based controllers, *ISA Transactions* **47**(4): 395–400.

Wei, D. and Craig, I. K. (2009). Grinding mill circuits — A survey of control and economic concerns, *International Journal of Mineral Processing* **90**(1-4): 56–66.

Wood, R. K. and Berry, M. W. (1973). Terminal composition control of a binary distillation column, *Chemical Engineering Science* **28**(9): 1707–1717.

Wu, Q. and Du, W. (2022). Online detection of model-plant mismatch in closed-loop systems with Gaussian processes, *IEEE Transactions On Industrial Informatics* **18**(4): 2213–2222.

Xu, L., Ge, S.-Q. and Guo, J.-Y. (2018). Application of self-adaptive TDF-IMC in grinding classification process, *2018 Chinese Control and Decision Conference (CCDC)*, IEEE, pp. 2982–2984.

Xu, X., Simkoff, J. M., Baldea, M., Chiang, L. H., Castillo, I., Bindlish, R. and Ashcraft, B. (2020). Data-driven plant-model mismatch estimation for dynamic matrix control systems, *International Journal of Robust and Nonlinear Control* **30**(17): 7103–7129.

Yerramilli, S. and Tangirala, A. K. (2016). Detection and diagnosis of model-plant mismatch in MIMO systems using plant-model ratio, *IFAC PapersOnLine* **49**(1): 266–271.

Yerramilli, S. and Tangirala, A. K. (2018). Detection and diagnosis of model-plant mismatch in multivariable model-based control schemes, *Journal of Process Control* **66**: 84–97.

Yin, F., Wang, H., Xie, L., Wu, P. and Song, Z. (2014). Data driven model mismatch detection based on statistical band of Markov parameters, *Computers & Electrical Engineering* **40**(7): 2178–2192.

Zheng, Q., Chen, Z. and Gao, Z. (2009). A practical approach to disturbance decoupling control, *Control Engineering Practice* **17**(9): 1016–1025.

Ziolkowski, L. (2022). *Extremum Seeking Control of Grinding Mill Circuits Based on Grinding Curves*, MEng Dissertation, University of Pretoria.

Zou, H. (2006). The adaptive Lasso and its oracle properties, *Journal of the American Statistical Association* **101**(476): 1418–1429.